



TECHNISCHE  
UNIVERSITÄT  
WIEN

## DISSERTATION

# Mathematical Modeling, Estimation, and Control of the Contour Evolution in Heavy-Plate Rolling

Ausgeführt zum Zwecke der Erlangung des akademischen Grades eines  
Doktors der technischen Wissenschaften (Dr.techn.)

unter der Leitung von  
Univ.-Prof. Dipl.-Ing. Dr.techn. Andreas Kugi  
E376  
Institut für Automatisierungs- und Regelungstechnik

eingereicht an der  
Technischen Universität Wien  
Fakultät für Elektrotechnik und Informationstechnik

von  
Florian Schausberger  
Matrikelnummer: 0655648  
Leonfeldnerstraße 75/7/3, 4040 Linz, Österreich

Wien, im November 2016

---



Studiendekan: Univ.-Prof. Mag.rer.nat. Dr.rer.nat. Gottfried Strasser

Tag des Rigorosums: 28. November 2016

Betreuer: Univ.-Prof. Dipl.-Ing. Dr.techn. Andreas Kugi

Erster Gutachter: Prof. Dr. André Desbiens

Zweiter Gutachter: Ao. Univ.-Prof. Dipl.-Ing. Dr.techn. Markus Vincze



---

## Vorwort

---

Die vorliegende Arbeit entstand im Rahmen meiner Tätigkeit als wissenschaftlicher Mitarbeiter am Institut für Automatisierungs- und Regelungstechnik (ACIN) der Technischen Universität Wien. Das Projekt wurde während seiner gesamten Laufzeit mit finanziellen Mitteln aus der Kooperation mit der AG der Dillinger Hüttenwerke unterstützt.

Ich möchte dieses Vorwort nutzen, um mich bei all jenen zu bedanken die zum erfolgreichen Abschluss dieser Arbeit beigetragen haben. Insbesondere gilt mein Dank Prof. Dr. Andreas Kugi für die Betreuung dieser Arbeit und seine fachliche Unterstützung in Form seines fundierten Wissens auf dem Gebiet der Modellierung und Regelungstechnik. Mein weiterer Dank gilt den Professoren Desbiens und Vincze für die Erstellung der Gutachten und Prof. Gawlik für die Übernahme des Prüfungsvorsitzes.

Dr. Andreas Steinböck möchte ich für seine fachliche Unterstützung, den notwendigen Freiraum zur Verwirklichung eigener Ideen und sein stets offenes Ohr bei Problemen danken. Vielen Dank an meine Kollegen Dr. Katrin Blank, Dr. Michael Baumgart, Dr. Thomas König und Robert Brauneis aus der Gruppe der Walzwerker für ihre fachliche und persönliche Unterstützung im Rahmen des Projektes. Danke auch an meinen Bürokollegen Paul Zeman für die vielen humorvollen Momente innerhalb und außerhalb der Arbeitszeit, die stets für eine kurzweilige Arbeitswoche gesorgt haben. Meinen Kolleginnen und Kollegen am ACIN danke ich für das gute Arbeitsklima, ihre fachlichen Ratschläge und ihre Hilfsbereitschaft.

Auf Seiten der AG der Dillinger Hüttenwerke möchte ich mich bei Dr. Martin Jochum, Dr. Daniel Wild und Joachim Groß für die Unterstützung bei Messungen und bei der Inbetriebnahme der entwickelten Algorithmen am Fertiggerüst danken. Der Führungsriege der AG der Dillinger Hüttenwerke gebührt mein Dank für die finanzielle Unterstützung dieser Arbeit und das entgegengebrachte Vertrauen um die Ergebnisse der vorliegenden Arbeit am Fertiggerüst testen zu dürfen.

Danke auch an meine Familie und meine Freunde für den nötigen Ausgleich zum Arbeitsalltag. Bei meinem Neffen Simon entschuldige ich mich für die verpassten Geburtstagsfeiern und Martinsfeste aufgrund der örtlichen Entfernung zwischen Wien und Adlwang und verspreche mich in dieser Hinsicht in Zukunft zu bessern. Schlussendlich möchte ich meiner Lebensgefährtin Katharina für ihr Verständnis und die liebevolle Unterstützung während der Zeit in Wien danken.

Wien, im November 2016

Florian Schausberger

*Für Katharina*





---

## Abstract

---

This thesis deals with the mathematical modeling, the estimation, and the control of the contour evolution in heavy-plate rolling. Reversing mill stands are used to reduce the thickness of heavy plates in consecutive rolling passes. During the rolling process, asymmetric rolling conditions in the lateral direction may lead to a deviation between the actual and the desired plate contour. This may cause a reduced product quality, product rejects, and in the worst case even damaged plant components around the rolling mill. Asymmetric rolling conditions are generally unknown and cannot be compensated in advance to prevent the plate from cambering. Therefore, a useful approach is to apply feedback if a shape defect occurs. Clearly, this requires a measurement of the contour of the plate. Precise measurements of the contour (longitudinal boundaries and shape of the head and tail end) can be used to optimize the adjustment of the mill stand to reduce the camber.

First, the estimation of the plate contour is discussed. Infrared cameras mounted at the ceiling of the rolling mill are used to capture images of the plate during the rolling passes. A threshold-based edge detection is performed in the infrared bitmaps. The detected edges are then used in an optimization-based approach which utilizes the restrictions of the movement of the plate being clamped in the rolling gap. Herein, a polynomial representation of the longitudinal boundaries of the plate is estimated based on the detected edges of several consecutive images. In addition to the contour of the plate, the translational and angular movement of the plate is estimated by the presented approach. A validation by means of a downstream contour measurement device shows a high accuracy of the proposed contour estimation method.

Second, a static model of the contour evolution is derived. The continuum-mechanics-based model predicts the contour of the plate after the rolling pass based on the contour before the rolling pass and the input and output thickness profiles. It is used to analyze the effects of temperature gradients in the lateral and

longitudinal direction on the contour evolution. Measurements of a plate rolled during the standard production process are used to validate the model. Moreover, a model covering the relation between the contour and the movement of the plate is presented. In particular, the model links the curvature and the angular velocity at the entry of the rolling gap with the curvature and the angular velocity at the exit of the rolling gap. The model is validated using the angular velocity and curvature of the plate obtained from the contour estimation approach.

The mathematical models are used in different control approaches for the reduction of contour errors. First, a feedforward control strategy to determine the required asymmetry of the rolling gap height to compensate contour errors in single passes is discussed. The optimization-based approach utilizes the continuum-mechanics-based model of the contour evolution. The control objectives can be changed in an intuitive manner by changing weighting factors of the objective function and input constraints are systematically incorporated. Moreover, the asymmetric compliance of the mill stand as a function of the rolling forces is identified and compensated based on the desired rolling forces. The resulting asymmetry of the output thickness after each pass is estimated and used to compensate disturbances affecting the asymmetry of the rolling gap. Furthermore, feedback control during the rolling pass is discussed. The measurement of the contour of the plate is subject to a transport delay. Hence, the presented approach utilizes the delay-free measurement of the angular movement of the plate in a two degrees-of-freedom control structure containing a Smith-predictor. Furthermore, a proof of the robust stability of the proposed control concept is presented. In general, compensating a contour error results in an inhomogeneous thickness profile in the lateral direction. Therefore, a method to determine a rolling schedule covering several rolling passes is presented which achieves both the desired contour and a homogeneous thickness profile of the final product.

Finally, simulation results and measurements for the proposed control approaches are shown. The influence of weighting and tuning factors on the control behavior is discussed by means of simulations. Measurements from the considered industrial rolling mill show that the proposed measures can significantly improve the contour of the rolled plates.

---

## Kurzzusammenfassung

---

Diese Arbeit beschäftigt sich mit der mathematischen Modellierung, der Schätzung und der Regelung der Konturentwicklung beim Walzen von Grobblech. Die sogenannten Walztafeln werden an Reversierwalzgerüsten in mehreren aufeinanderfolgenden Stichen auf eine bestimmte Dicke ausgewalzt. Während der Walzung können asymmetrische Verhältnisse in Breitenrichtung Abweichungen zwischen der Soll- und Istkontur zur Folge haben. Dies kann zu verringerter Produktqualität, Produktausfällen und im schlimmsten Fall zur Beschädigung benachbarter Anlagenteile führen. Die während der Walzung auftretenden Dickenasymmetrien sind im Allgemeinen nicht bekannt und können daher nicht vorab kompensiert werden. Deshalb scheint es sinnvoll, Gegenmaßnahmen erst beim Auftreten von Konturfehlern zu ergreifen. Es ist also eine Messung der Walztafelkontur notwendig, um entsprechende Korrekturen der Anstellung des Walzgerüstes bestimmen zu können.

Zu Beginn wird die Ermittlung der Walztafelkontur diskutiert. Infrarotkameras an der Hallendecke des Walzwerkes nehmen Bilder der Walztafel während der Walzung auf. Die Kanten der Walztafel innerhalb der aufgenommenen Bilder werden anhand einer Schwellwertdetektion ermittelt. Die Information über die Lage der Walztafelkanten wird in einem optimierungsbasierten Verfahren zur Schätzung der Kontur und der Bewegung der Walztafel verwendet. Eine Validierung anhand von Messdaten einer nachgelagerten Konturvermessungsanlage bestätigt die hohe Genauigkeit des vorgestellten Verfahrens.

Anschließend wird ein mathematisches Modell der Entwicklung der Walztafelkontur vorgestellt. Das statische, kontinuumsmechanische Modell prädiziert die Kontur nach dem Stich aufgrund der Kontur vor dem Stich und der Ein- und Auslaufdickenprofile der Walztafel. Anhand des Modells wird der Einfluss von Temperaturgradienten in Quer- und Längsrichtung analysiert. Messungen einer Walztafel aus dem normalen Produktionsprozess werden zur Validierung des Modells verwendet. Zusätzlich wird ein Modell zur Beschreibung des Zusam-

menhanges zwischen der Bewegung und der Konturentwicklung der Walztafel präsentiert. Dieses Modell, welches die Krümmung und die Winkelgeschwindigkeit der Walztafel vor und nach dem Walzspalt in Verbindung bringt, wird anhand von Messdaten der Konturschätzung validiert.

Die mathematischen Modelle werden in verschiedenen Strategien zur Verminderung von Konturfehlern verwendet. Zunächst wird eine Vorsteuerungsstrategie zur Bestimmung der notwendigen Gerüstanstellung für die Beseitigung von Konturfehlern in einem einzelnen Stich diskutiert. Der optimierungsbasierte Ansatz verwendet das kontinuumsmechanische Modell der Entwicklung der Walztafelkontur. Das Regelverhalten kann durch Anpassung von Gewichtungsfaktoren gezielt beeinflusst und Beschränkungen der Stellgrößen systematisch berücksichtigt werden. Es konnte eine von der Walzkraft abhängige, asymmetrische Auffederung des Walzgerüstes beobachtet werden, welche anhand der Sollwerte der Walzkraft kompensiert wird. Die sich einstellende Asymmetrie der Auslaufdicke wird geschätzt und zur Kompensation von Störungen der Asymmetrie des Walzspaltes herangezogen. Anschließend wird eine Regelungsstrategie mit Rückkopplung zur Verringerung von Konturfehlern während des aktuellen Stiches vorgestellt. Die Messung der sich im Walzspalt ausbildenden Kontur der Walztafel kann nur mit einer Transportverzögerung erfolgen. Deshalb wird die verzögerungsfreie Messung der Winkelgeschwindigkeit der Walztafel zur Regelung in einem 2-Freiheitsgrade Regelungskonzept mit einem Smith-Prädiktor herangezogen. Zusätzlich wird die robuste Stabilität des Regelungskonzeptes bewiesen. Im Allgemeinen führt die Kompensation von Konturfehlern zu einem Dickenkeil in Querrichtung. Deshalb wird ein mehrere Stiche umfassender Optimierungsansatz zur Erzielung der Sollkontur bei homogener Enddicke präsentiert.

Zum Schluss werden Simulationsergebnisse und Messungen der entwickelten Verfahren gezeigt. Der Einfluss von Parametern und Gewichtungsfaktoren auf das Regelungsverhalten wird anhand von Simulationen erläutert. Am betrachteten industriellen Walzgerüst aufgenommene Messungen zeigen die Effektivität der vorgestellten Methoden zur Beseitigung von Konturfehlern.

---

# Contents

---

<b>List of symbols</b>	<b>xiii</b>
<b>1 Introduction</b>	<b>1</b>
1.1 Hot rolling of heavy plates . . . . .	2
1.2 Problem description and objectives of this work . . . . .	3
1.3 State of the art, new contributions of this work . . . . .	4
1.4 Structure of this thesis . . . . .	11
<b>2 Estimation of the plate contour</b>	<b>13</b>
2.1 Mathematical model of the movement of the plate boundary . . . . .	15
2.2 Optimization-based contour estimation . . . . .	18
2.2.1 Formulation of the optimization-based contour estimation	18
2.2.1.1 Parameterization of the head end . . . . .	18
2.2.1.2 Optimization problem with a head end in the FOV	19
2.2.1.3 Optimization problem without a head end in the FOV . . . . .	21
2.2.2 Numerical solution of the optimization problem . . . . .	21
2.3 Estimation of the plate velocity . . . . .	22
2.4 Receding horizon approach . . . . .	25
2.5 Recording and processing of image data . . . . .	27
2.6 Validation and statistics . . . . .	30
2.7 Summary . . . . .	35
<b>3 Modeling of the contour evolution</b>	<b>37</b>
3.1 Mathematical model for estimating camber and residual stresses . . . . .	38
3.2 Derivation of the boundary conditions . . . . .	42
3.3 Solution of the biharmonic equation . . . . .	43

3.3.1	Power series solution . . . . .	44
3.3.2	Parameterization of the plate contour . . . . .	46
3.3.3	Simulation results . . . . .	48
3.4	Effect of non-uniform elastic properties . . . . .	50
3.5	Effect of thermal expansion . . . . .	55
3.6	Validation . . . . .	55
3.7	Summary . . . . .	57
<b>4</b>	<b>Modeling of the plate movement during the rolling pass</b>	<b>59</b>
4.1	Movement of the plate . . . . .	60
4.2	Evolution of the camber . . . . .	62
4.3	Time-free formulation . . . . .	63
4.4	Validation . . . . .	64
4.5	Summary . . . . .	66
<b>5</b>	<b>Model-based control of the contour evolution</b>	<b>67</b>
5.1	Single pass-to-pass adjustment of the rolling gap (feedforward control) . . . . .	68
5.1.1	Parameterization of the thickness profiles and the centerline . . . . .	69
5.1.2	Approximation of the plastic strain . . . . .	70
5.1.3	Formulation of the optimization problem . . . . .	71
5.1.4	Estimation of the thickness asymmetry . . . . .	72
5.1.5	Compensation of the asymmetric mill stand deflection . . . . .	74
5.1.6	Combination of feedforward control and asymmetry estimation . . . . .	76
5.2	Feedback control during the rolling pass . . . . .	77
5.2.1	Plant model . . . . .	78
5.2.2	Camber control . . . . .	79
5.2.2.1	Inner loop . . . . .	80
5.2.2.2	Outer loop . . . . .	82
5.2.3	Implementation . . . . .	87
5.3	Multi-pass adjustment of the rolling gap . . . . .	88
5.3.1	Formulation of the optimization problem . . . . .	88
5.3.2	Rolling of annular sectors . . . . .	89
5.4	Summary . . . . .	91
<b>6</b>	<b>Numerical results and measurements</b>	<b>93</b>
6.1	Simulation results . . . . .	93
6.1.1	Single pass-to-pass adjustment . . . . .	93
6.1.1.1	Initial input thickness asymmetry . . . . .	95
6.1.1.2	Initial contour error . . . . .	97
6.1.1.3	Non-ideal control of actuator positions and asymmetry disturbance . . . . .	97

<i>Content</i>	xi
6.1.2 Feedback control . . . . .	99
6.1.3 Multi-pass adjustment . . . . .	101
6.1.3.1 Compensation of contour errors . . . . .	102
6.1.3.2 Rolling of annular sectors . . . . .	103
6.2 Measurements . . . . .	104
6.2.1 Single pass-to-pass adjustment . . . . .	104
6.2.2 Feedback control . . . . .	108
6.3 Summary . . . . .	111
<b>7 Conclusions</b>	<b>113</b>
7.1 Summary . . . . .	113
7.2 Conclusions . . . . .	115
7.3 Outlook . . . . .	116
<b>A Static optimization</b>	<b>119</b>
A.1 Newton method . . . . .	120
A.2 Quasi-Newton method . . . . .	121
A.3 Gauss-Newton method . . . . .	122
A.4 Line search . . . . .	122
A.4.1 Line search I . . . . .	122
A.4.2 Line search II . . . . .	123
<b>B Gradients used in the estimation of the plate contour</b>	<b>125</b>
<b>C Proof of the robust stability of the feedback control loop</b>	<b>129</b>
<b>Bibliography</b>	<b>131</b>





---

## List of symbols

---

---

### Greek symbols

---

$\beta_i$	weighting factor
$\Delta\xi, \Delta\eta, \varphi$	position and orientation of the plate-fixed coordinate frame (m, m, rad)
$\Delta h$	asymmetry of the plate thickness (m)
$\Delta$	Laplacian ( $1/\text{m}^2$ )
$\delta$	centerline of the plate (m)
$\delta'$	local slope of the centerline
$\delta''$	local curvature of the centerline ( $1/\text{m}$ )
$\nabla$	Nabla ( $1/\text{m}$ )
$\nu$	Poisson's ratio
$\Omega$	angular displacement per unit processed plate length (rad/m)
$\omega$	angular velocity (rad/s)
$\xi, \eta, \zeta$	Cartesian coordinate frame fixed to the mill stand (m)
$\xi_{pl}, \eta_{pl}, \zeta_{pl}$	Cartesian coordinate frame fixed to the plate (m)
$\delta_{max}$	maximum lateral deviation of the centerline (m)
$\epsilon$	strain
$\sigma$	stress ( $\text{N}/\text{m}^2$ )

---

### Latin symbols

---

$\mathcal{R}$	residual
$\Delta\mathbf{h}, \Delta\mathbf{H}$	vector and matrix of thickness asymmetries (m)
$\mathbf{A}, \mathbf{b}$	coefficient matrix and right-hand side of a linear equation
$\mathbf{g}$	gradient
$\mathbf{H}$	Hessian

<b>I</b>	identity matrix
<b>J</b>	Jacobian
<b>p</b>	coefficient vector of the polynomial $p$
<b>w</b>	vector of optimization variables
<b>x</b>	state vector
$E$	Young's modulus (N/m <sup>2</sup> )
$F$	Airy's stress function (N)
$F$	force (N)
$G$	shear modulus (N/m <sup>2</sup> )
$h$	thickness of the plate (m)
$I$	intensity measured by the infrared camera
$J$	objective function
$l$	length of the plate (m)
$N_B$	degree of the polynomials describing the plate boundary
$N_P$	number of grid points to describe the thickness asymmetry
$N_{rp}$	number of passes in the multi-pass approach
$p$	polynomial
$p_{Bi}$	polynomial defining the plate boundary
$s$	Laplace variable (1/m)
$T$	temperature (°C)
$t$	time (s)
$T_I, T_O$	PI-controller constants of inner and outer loop (m, m)
$t_k$	grid point of discrete-time axis (s)
$T_s$	sampling time (s)
$T_{s,fb}$	sampling time of the feedback controller (s)
$u$	displacement in $x$ -direction (m)
$v$	displacement in $y$ -direction (m)
$V_I, V_O$	PI-controller gains of inner and outer loop (1/m, 1/m)
$v_L$	longitudinal velocity (m/s)
$v_S$	sideways (lateral) velocity (m/s)
$w$	width of the plate (m)
$X$	Lagrangian coordinate in longitudinal direction (m)
$x, y, z$	Cartesian coordinate frame located at the center of the plate (m)
$x_i$	grid point to describe the asymmetry of the plate thickness (m)
$Y$	Lagrangian coordinate in lateral direction (m)

---

**Subscripts**

---

$0$	usually designating an initial value
$act$	actual
$bwd$	backward

<i>cam</i>	camera
<i>cmd</i>	contour measurement device
<i>comp</i>	compensation
<i>C</i>	cone
<i>des</i>	desired
<i>dist</i>	disturbance
<i>fb</i>	feedback signal
<i>ff</i>	feedforward signal
<i>fov</i>	field of view
<i> fwd</i>	forward
<i>hom</i>	homogeneous
<i>H</i>	head
<i>I</i>	inner
<i>k</i>	discrete-time index
<i>L</i>	in longitudinal direction
<i>max</i>	maximum
<i>mh</i>	referring to a measurement of a quantity at the head end
<i>min</i>	minimum
<i>ml</i>	referring to a measurement of a longitudinal quantity
<i>O</i>	outer
<i>part</i>	particular
<i>pl</i>	plate
<i>pred</i>	predicted
<i>ref</i>	reference
<i>rel</i>	relative
<i>req</i>	required
<i>roll</i>	rolling
<i>S</i>	sideways (lateral direction)
<i>th</i>	threshold
<i>V</i>	referring to a quantity of the velocity estimation
<i>xx</i>	normal component in <i>x</i> -direction
<i>xy</i>	shear component
<i>yy</i>	normal component in <i>y</i> -direction

---

**Superscripts**

---

<i>el</i>	elastic
<i>in</i>	input
<i>out</i>	output
<i>pl</i>	plastic
<i>rg</i>	rolling gap



# CHAPTER 1

---

## Introduction

---

The steel industry has a history of more than hundred years. Although the basics of modern steel production techniques were developed decades ago, the quality demands on steel products are still increasing. These demands are driven by the need for special material qualities and features that are only reached by today's high tech materials. Such materials are key enablers to build skyscrapers, to deliver oil and gas in pipelines across continents, and to harvest wind energy with offshore wind turbines. Furthermore, the steel industry is subject to governmental restrictions on the pollution of the environment and the energy consumption caused by the steel production. In addition, the legal frameworks and varying energy prices in different countries play an important role for steel manufacturers to remain competitive on the market. Main objectives of steel manufacturers are thus to increase the production quality and to reduce the emissions and the energy consumption caused by their production processes. Measures to cope with these challenges help to preserve the steel industry in high-wage countries with restrictive environmental regulations.

In this work, the production of heavy plates is considered. The quality of the final product is mainly characterized by the material properties, the shape, and the thickness of the plates. The usable area of the plate after edge trimming clearly depends on the shape of the plate. Hence, the resulting plate contour is of special interest in the production process. Imperfections of the plate contour may result from asymmetric rolling conditions in the lateral direction of the plate. This includes inhomogeneous input and/or output thickness profiles in the width direction and spatially inhomogeneous as well as time-dependent temperature variations of the plate. These are the motivations for the development of control measures to improve the shape of the rolled products, in particular the plate contour.

## 1.1 Hot rolling of heavy plates

The considered rolling mill of AG der Dillinger Hüttenwerke, Germany, is outlined in Fig. 1.1. Here, the slabs from the slab yard are first reheated in one of the furnaces. During the heating, a scale layer builds up, which is removed in a descaling unit before the actual rolling steps at the roughing mill stand. After the beginning of the rolling process, the product is called plate. Following the lateral expansion phase to the desired width at the roughing mill, the plate is rolled in longitudinal direction to the desired plate thickness at the finishing mill. In the following cooling section, a specific reduction of the plate temperature may be enforced to obtain the desired mechanical properties of the plate material. Then, the plate is leveled to reduce residual stresses. Finally it is carried away and cut to the desired lateral and longitudinal dimensions. At the considered rolling mill, 3 to 400 mm thick plates with a length of up to 50 m and a maximum width of 4.7 m may be produced.

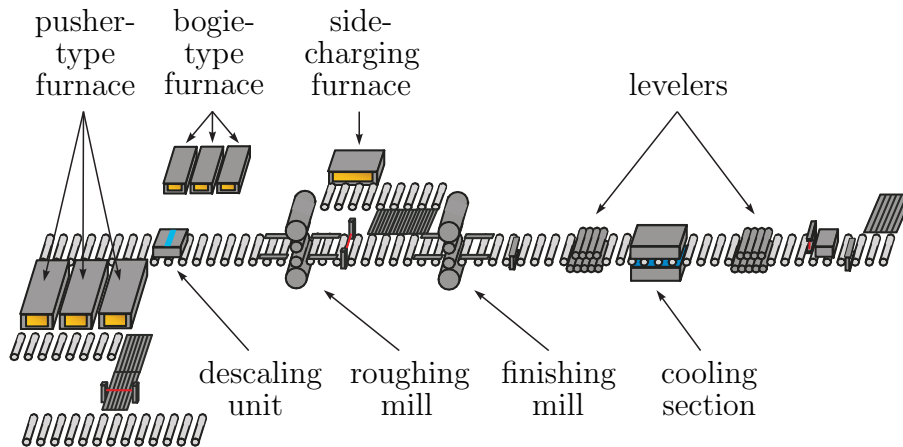


Figure 1.1: Processing line of AG der Dillinger Hüttenwerke, Germany.

The finishing mill considered in this work is a 4.8 m wide quatro-reversing mill stand and is shown in Fig. 1.2. The finishing mill can apply forces up to 90 MN to reduce the thickness of the plates in successive rolling passes. The term rolling pass or pass denotes a single reduction step of the thickness of the plate. Rolling passes are performed in alternating direction at reversing mill stands. Due to the compliance of the 16.5 m high mill stand and the acting forces, elastic deflections of up to 14 mm may occur. In comparison, the tolerances on the thickness of the plate are in the range of one tenth of a millimeter.

Moveable side guides are installed before and after the mill stand, which are especially used to center the plate in the lateral direction before each rolling pass. During the rolling pass the downstream side guides are opened. However, the upstream side guides are also used to center plates which sometimes tend to move sideways during the rolling pass.

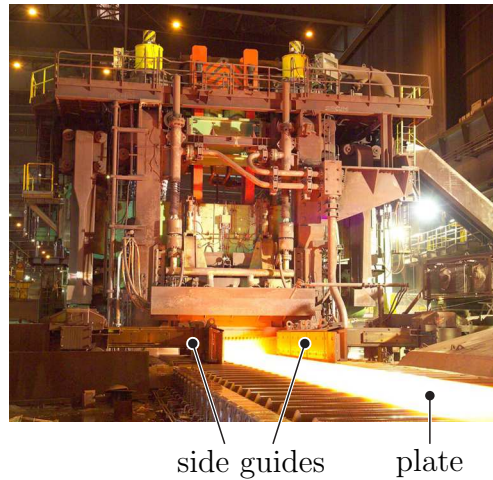


Figure 1.2: The considered mill stand at AG der Dillinger Hüttenwerke, Germany.

## 1.2 Problem description and objectives of this work

In general, the shape of the plate, as seen in top view, should be rectangular to maximize the usable area. The plastic deformation of the plate during the rolling pass can also lead to a deviation of the actual plate contour from the desired one, e.g., the contour of the plate may have a camber (cf. Fig. 1.3). This may cause a lowered product quality, product rejects, and in the worst case even damaged plant components around the rolling mill. The deviations may result from asymmetric conditions during the rolling process, e.g., non-homogeneous temperature or thickness distributions in the lateral direction.

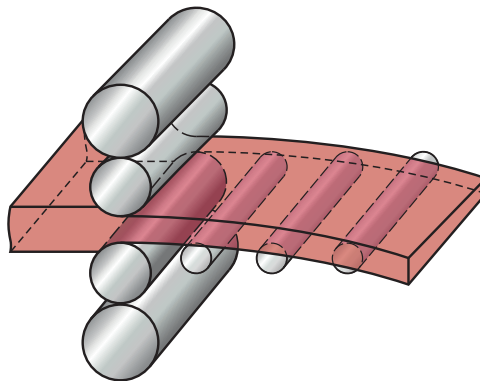


Figure 1.3: Contour error (camber) appearing during the rolling process.

Asymmetric rolling conditions are generally unknown and cannot be compensated in advance to prevent the plate from cambering. Therefore, a common approach is to apply feedback if a shape defect occurs. Clearly, this requires the

measurement of the contour of the plate. A precise knowledge of the contour (longitudinal boundaries and shape of the head and tail end) can be used to optimize the adjustment of the rolling mill to reduce the camber.

To determine the necessary control input of the mill stand to reduce contour errors, the evolution of the plate contour must be thoroughly understood. Here, mathematical models may be used to predict the evolution of the plate contour. However, real-time model-based control concepts require models with high accuracy and moderate computational effort. To meet these demands, a tailored mathematical model of the evolution of the plate contour is necessary.

Thus, the objectives of this work can be summarized as follows:

- *Estimation of the plate contour during the rolling pass*  
The longitudinal and lateral edges of the plate should be accurately and robustly estimated already during the rolling pass. In addition to the contour of the plate, the movement of the plate (rotational and lateral movement) should be estimated and the influence of these movements on the camber formation should be investigated. Furthermore, a tracking of the product during the rolling pass is necessary, i. e., a precise estimation of the longitudinal speed of the plate. Suitable measurement equipment should be selected and the necessary algorithms for the contour estimation implemented.
- *Mathematical modeling of the contour evolution*  
The mathematical model should be suitable for real-time control applications and it should accurately predict the evolution of the plate contour. Furthermore, the effects of temperature inhomogeneities on the camber formation should be investigated. The model should help to study the factors that influence the formation of camber. Finally, experiments have to be designed and conducted to validate the model.
- *Design and validation of camber reducing control concepts*  
Based on the estimation or measurement of the plate contour and the model of the contour evolution, control concepts to reduce the camber, which may occur during the rolling pass, should be designed. The control concepts should be implemented and validated at the considered rolling mill.

### 1.3 State of the art and new contributions of this work

This chapter gives a short overview of the literature published in the fields of measurement, mathematical modeling, and reduction of shape errors in hot rolling. Already in 1987, Tanaka et al. used three devices to measure the lateral position of the plate downstream of the mill (cf. [1]). Based on these measurements, a



polynomial representation of the actual plate profile is estimated and used for feedback control to reduce the occurring camber by modifying the output thickness wedge.

Soaring computer performance enabled the usage of image processing techniques for contour estimation as proposed in [2], where three 2D-CCD cameras capture neighboring areas of the plate. In this camera configuration, the acute angle between the plate surface and the optical axis of the camera requires a precise calibration of the camera to accurately reconstruct the real image. After this preprocessing step, a customized edge detection routine estimates the edge of the plate. The detected edges of neighboring images are joined based on the longitudinal speed of the plate and to ensure  $C_1$ -continuity of the estimated plate edges. A very similar approach using just one camera to estimate the centerline of the plate is discussed in [3].

Also in strip rolling, 2D-cameras are used to track the lateral position of the strip during the rolling process. Carruthers-Watt et al. (cf. [4]) used measurements from several cameras between the mill stands to determine the lateral position of the strip in the finishing train of a hot strip mill. The edge is identified as maximum of the gradient of the intensity of the image in the lateral direction and parameterized using Bezier curves. A similar measurement setup and a mathematical model of the lateral position of the strip for steering control is discussed in [5]. There, an  $H_2$  controller that is robust against heterogeneous properties of the different rolled products was designed using the tilts of several mill stands as control inputs.

An algorithm that stitches several images of the plate was developed in [6], [7], and [8]. Common feature points are identified on two consecutive images to determine the displacement between the images, which are captured by a CCD camera. Ollikkala et al. (cf. [9]) used a very similar approach. However, in this solution the inclined viewing angle of the CCD-camera requires a perspective correction of the recorded images. After this image rectification step, an edge detection algorithm is used to extract the boundaries of the plate.

The existing solutions for the detection of the plate contour are mainly based on specialized image processing techniques. In most published works in this field, neither lateral nor rotational movements of the plate are estimated or measured. The knowledge of the restrictions of the movement of the plate during the rolling process is also not taken into account, which may reduce the achieved accuracy of the contour estimation.

Clearly, the angular velocity is linked with the lateral movement (snaking) of the plate in the rolling gap. This movement may lead to an off-center position of the plate in the lateral direction. Because of the resulting asymmetric loading of the rolls, knowledge of the lateral position of the plate is also vital for the necessary adjustment of the rolling gap actuators.

Furthermore, the estimation of the longitudinal speed of the plate, which may be required for the detection of the contour, is not covered in many works. Usually,

the speed of the plate is calculated using a mathematical model (forward slip model) and measurements of the angular velocity of the rolls of the mill, see, e. g., [10]. In general, this results in an error-prone estimation of plate speed due to inaccuracies of the slip model and therefore in an additional error of the estimated contour. Hence, a more accurate method to determine the plate velocity seems favorable in terms of the contour detection.

Therefore, an approach to simultaneously estimate the contour and the movement of the plate during the rolling pass is discussed in this work. It uses a mathematical model of the movement of the plate and top-view images of the plate captured by a 2D-infrared camera. The model considers the restrictions of the lateral movement of the plate in the rolling gap. In addition to the contour, the angular movement and the longitudinal velocity of the plate are estimated.

In the past, different approaches were suggested to model the movement and the contour evolution of flat products in the rolling process. The existing models may be classified into two categories:

- Kinematic models only based on the conservation of mass.
- Continuum-mechanics-based models of the contour evolution.

Models from the first category mainly focus on the modeling of the lateral position of the plate during the rolling pass. In heavy plate rolling, the resulting contour of the plate and its evolution are of special interest. This contour defines the usable area of the final plate. These models typically require only moderate computational effort. The models belonging to the second category are using theory from continuum mechanics and elastoplastic material properties of the plate to estimate the plate contour. These models have a high accuracy but entail large computational effort, which may render them unsuitable for real-time control.

One of the models belonging to the first category is proposed in [11], where the effect of snaking of a strip in a tandem cold rolling mill was analyzed. The model utilizes the plastic deformation of the strip as well as the elastic deformation of the rolls and the mill housing to predict the angular velocity of the strip at the entry and exit of the rolling gap. The lateral position of the strip is derived from the angular velocity and the rigid body motion of the strip outside the rolling gap.

Shiraishi et al. (cf. [12]) investigated the relation between camber and a thickness wedge of the strip under restrictions of the lateral movement of the strip. The proposed model also includes the use of edgers at the rolling gap entrance and the application of tension on the rolled strip. A model based on the conservation of mass in the rolling gap is used to compute the curvature of the strip. Experimental results are provided from a laboratory rolling mill to investigate the effects of the restrictions of the lateral strip movement.

Models belonging to the second category are proposed, e. g., in [13], [14], [15], [16], and [17]. A FEM simulation was used in [13] to predict the camber and the lateral movement of a hot rolled strip with an elastic-plastic material model. The camber model covers roll deflection as well as roll flattening during the rolling process and shows a good agreement with measurements from a pilot plant.

Also in [14] FEM is used to simulate the evolution of camber during hot rolling. The influence of lateral temperature variations of the plate on the resulting camber is investigated with a two-dimensional analysis. Furthermore, three-dimensional FEM simulations with elastic-plastic material properties were conducted to examine the effects of non-uniform rolling forces. Strategies for the reduction of camber across several rolling passes were also discussed.

Trull et al. (cf. [15]) developed an advanced finite element model of a plate mill to simulate the shape evolution of a rolled plate. The model includes the stretch of the mill housing, the profile of the rolls and the material properties of the plate. It is used to investigate the influence of the roll condition on the shape of the plate.

The effects of width-wise asymmetric rolling conditions in strip rolling were analyzed in [16]. The mill stretch and the deformation of the roll stack are used to approximate the lateral thickness profile, the resulting camber, and the snaking of the strip at the exit of the rolling gap.

A three-dimensional FEM model was also used in [17] to predict the shape of heavy plates in hot rolling. In particular, a rigid plastic thermomechanical FEM was developed to investigate inhomogeneous plastic deformations. The evolution of uneven shapes in the longitudinal rolling process and the broadside-longitudinal rolling process were analyzed in detail.

A mathematical model bridging the gap between the two different model categories is presented in this work. This model predicts the contour of the plate, which is in contrast to the models from the first category. Additionally, it requires only a moderate computational effort compared to the models from the second category. It utilizes the input and output thickness of the plate as well as its input contour to predict the residual stresses and the contour of the plate after the rolling pass. Generally, the output thickness profile is assumed to be known in this work. It may come from measurements or a dedicated model of the rolling gap, which, however, is not further discussed here. The presented model serves as a basis for studying the factors that influence the formation of camber. Furthermore, the high accuracy of the proposed model and its moderate computational costs make it suitable for model-based control concepts for the reduction of an existing camber. The nexus between the evolution of the camber and the angular velocity of the plate is described by a supplementary kinematic model.

Several approaches to avoid contour errors and off-centering of the strip in hot strip rolling can be found in the literature. In the hot strip rolling process, a number of consecutive mill stands are used to reduce the thickness of the strip. Contrary to configurations with reversing mill stands, the rolling direction does not change. Kiyota et al. (cf. [18]) derived a model covering the plastic deformation of the strip in the rolling gap and the elastic deformation of the mill housing. Based on a linear model of the movement of the plate, an optimal regulator and a state observer were designed and validated using simulations. Furthermore, adjustment coefficients accounting for different rolling conditions were introduced. Sliding mode control and a state observer were presented in [19] to reduce the lateral movement of the strip. The controller design is based on a linear mathematical model using the asymmetry of the rolling gap as control input. Simulation and measurement results from an industrial plant show the achieved improvements. Also model predictive control (MPC) is used to reduce the lateral movement of strips in hot rolling (cf. [20]). The MPC formulation allows the systematic incorporation of input and state constraints into the design of the controller.

The strip tracking problem at a hot strip finishing mill during the tail-out phase was discussed in [21]. A mathematical model based on first principles is the basis for a linear model predictive controller with the mill stand tilt as control input. The states of the mathematical model are estimated using a Kalman filter where the rolling forces are used as measurements. Based on simulations the results of the MPC and a PID-controller were compared.

The reduction of contour errors during the rolling using reversing mill stands is only rarely discussed in the literature. An early control-based attempt to reduce the camber in plate rolling was presented in [1]. There, a model linking the thickness wedge with the contour of the plate as well as a setup to measure the camber of the plate were discussed. Correction coefficients have to be manually tuned to achieve an appropriate model accuracy. The camber of the plate is measured in the forward pass whereas the asymmetry of the rolling gap is only adjusted in the backward pass to reduce camber.

A FEM based simulator to predict camber in hot rolling was developed by Jeong et al. (cf. [22]). The plate is treated as a rigid perfectly plastic body in the three-dimensional problem formulation of the deformation in the rolling gap. The developed FEM simulator was used to design an output feedback fuzzy controller for the curvature and the lateral movement of the plate. The asymmetry of the rolling gap is adjusted during the actual pass. The resulting controller was compared with a PI-controller utilizing the presented simulator.

The camber reducing approaches found in the literature do not fully exploit the possibilities resulting from the alternating rolling direction during heavy plate rolling. The subsequent rolling passes on reversing mill stands offer the use of two different control strategies:

- Measure the plate contour and counteract to contour errors during the same

pass.

- Use the measurement of the plate contour to reduce occurring camber in the subsequent pass(es).

Plates with camber may collide with and thus damage plant components downstream the rolling mill. If a large camber occurs, the first approach seems more suitable because the camber is reduced earlier compared to the second one. In general, however, there exists a time delay between the generation and the measurement of the plate contour. Hence, all appearing errors can only be corrected with a delay. This is why it also seems suitable to adjust the inputs of the mill stand in the next pass as a feedforward compensation of contour errors. A drawback of the second approach is that it cannot eliminate contour errors appearing in the last pass.

In addition to the top-view shape of the plate, also the homogeneity of the plate thickness defines the quality of the final rolled plate. Hence, the effect of camber-reducing counter-measures on the thickness distribution of the plate should be considered in the controller design. The existing solutions to curb camber in heavy plate rolling only focus on one of the discussed control strategies. Also constraints on the maximum allowed asymmetry of the thickness of the plate are generally not taken into account.

In this work, an optimization-based approach utilizing a mathematical model of the contour evolution is presented. Optimization-based methods can be used with fairly general mathematical models and input and system constraints can be systematically incorporated. Furthermore, the control objectives can be considered in an intuitive manner by suitably shaping the objective function. In addition to the contour of the plate, the measurement of the angular velocity of the plate is used in a feedback control approach. The angular velocity of the plate can be measured with a much smaller delay than the contour of the plate. This facilitates to minimize contour errors emerging during the pass. The presented methods allow for systematic control actions during the rolling pass (feedback) and from one pass to the next pass (feedforward) in a two degrees-of-freedom control structure.

The mathematical model of the contour evolution is also used in an optimization-based estimation approach. Here, the asymmetry of the output thickness is estimated using the contour of the plate before and after the respective rolling pass. This information about the rolling gap can be utilized to minimize negative effects of asymmetric rolling conditions on the plate thickness.

In the course of this PHD thesis, parts of the obtained results were already published in journals and presented at conferences.

### Contour and velocity estimation

- [23] F. Schausberger, A. Steinboeck, and A. Kugi, “Optimization-based estimator for the contour and movement of heavy plates in hot rolling”, *Journal of Process Control*, vol. 29, pp. 23–32, 2015.
- [24] F. Schausberger, K. Speicher, A. Steinboeck, M. Jochum, and A. Kugi, “Two illustrative examples to show the potential of thermography for process monitoring and control in hot rolling”, in *Proceedings of 16<sup>th</sup> IFAC Symposium on Control, Optimization and Automation in Mining, Mineral & Metal Processing (MMM)*, Oulu, Finland, Aug. 2015, pp. 48–53.
- [25] F. Schausberger, A. Steinboeck, A. Kugi, M. Jochum, D. Wild, and T. Kiefer, “Vision-based material tracking in heavy-plate rolling”, in *Proceedings of 17<sup>th</sup> IFAC Symposium on Control, Optimization and Automation in Mining, Mineral & Metal Processing (MMM)*, Vienna, Austria, Aug. 2016.

### Mathematical modeling of the contour evolution

- [26] F. Schausberger, A. Steinboeck, and A. Kugi, “Mathematical modeling of the contour evolution of heavy plates in hot rolling”, *Applied Mathematical Modelling*, vol. 39, pp. 4534–4547, 2015.

### Estimation and control concepts

- [27] F. Schausberger, A. Steinboeck, A. Kugi, M. Jochum, D. Wild, and T. Kiefer, “Estimation of the thickness asymmetry using models for the contour evolution and vision-based measurements of plates in hot rolling”, in *Proceedings of METEC and 2<sup>nd</sup> European Steel Technology and Application Days (ESTAD)*, Düsseldorf, Germany, Jun. 2015, pp. 1–8.
- [28] F. Schausberger, A. Steinboeck, and A. Kugi, “Optimization-based reduction of contour errors of heavy plates in hot rolling”, *Journal of Process Control*, vol. 47, pp. 150–160, 2016.
- [29] F. Schausberger, A. Steinboeck, and A. Kugi, “Feedback control of the contour shape in heavy-plate hot rolling”, *Submitted to IEEE Transactions on Control Systems Technology*, 2016.

## 1.4 Structure of this thesis

This work is organized as follows: The estimation of the contour and the movement of the plate are discussed in Chapter 2. In Chapter 3, a mathematical model of the contour evolution is presented. This model predicts the contour after a rolling pass based on the input and output thickness profile and the contour before the rolling pass. Furthermore, a mathematical model which links the angular velocity of the plate with the resulting contour is discussed in Chapter 4. These two models are the basis for the control concepts designed in Chapter 5. The proposed strategies are validated by means of simulations and measurements in Chapter 6. Finally, Chapter 7 concludes this work with a summary and an outlook on future work.





## CHAPTER 2

---

### Estimation of the plate contour

---

The methods to reduce occurring camber presented in this work essentially build on the knowledge of the plate contour. Here, the longitudinal edges as well as the shape of the head and tail end of the plate are of interest. In this chapter, the methods used to estimate the plate contour are discussed. Simply measuring the whole plate contour in one step, e. g., by means of edge detection of an image of the whole plate, is not possible in the considered application due to the following reasons:

- The contour of the plate is partly covered by plant components.
- The measurement should be performed during rolling in real-time.
- The length to width ratio of long plates is very different from the aspect ratio of common cameras.

Furthermore, the estimation of the contour should be carried out as close as possible to the rolling gap because of the following reasons:

- Short plates should also be captured.
- The time delay between the generation of a camber and its estimation should be kept as small as possible.

Keeping the time delay small is also important because a plate with a camber before the rolling pass may lead to an off-center position of the plate in the lateral direction. The consequences are asymmetric rolling forces and a non-homogeneous rolling gap which may further increase camber.

Therefore, the contour and the lateral position of the plate should be estimated during the rolling pass itself and close to the rolling mill. Directly at the mill

stand, the harsh environment may deteriorate the accuracy and the robustness of measurements. Also the lateral and rotational movement of the plate, which is not considered in many published contour estimation procedures, makes contour estimation difficult. In case of pure longitudinal movement, the contour could be obtained by simple integration of the plate velocity leading to the plate position and using measurement signals gathered at a spatially fixed position. Under real

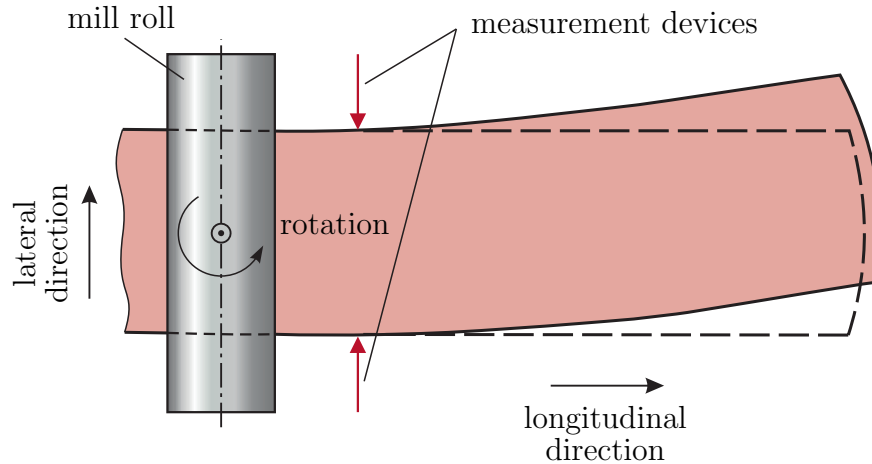


Figure 2.1: Measurement setup providing insufficient data for the estimation of the longitudinal boundaries of the plate. The solid line represents a rotating plate with camber. A rectangular plate with pure longitudinal movement is shown as dashed lines. Both contours may lead to the same position signals at the measurement devices, which are located at a spatially fixed position.

rolling conditions, this approach is insufficient because the plate may also rotate in addition to its main longitudinal motion (cf. Fig. 2.1). The possible rotation of the plate during the rolling process complicates the estimation of the contour.

To solve the contour estimation task, 2D-infrared cameras were installed before and after the considered rolling mill to measure the contour of the plate in both rolling directions. Here, the whole plate cannot be captured within a single image because the plate may be long and partly hidden by other plant components. Hence, the camera can only capture parts of the rolled plate and the contour has to be determined using a series of images. The edges of the plate within a single image are determined using an edge detection algorithm. The result of the edge detection of several images is then fed into an optimization-based algorithm which yields the whole contour of the plate. The presented approach utilizes the knowledge about the restrictions of the plate movement resulting from the plate being clamped in the rolling gap. Additionally, the algorithm estimates the movement of the plate characterized by its angular and longitudinal velocity. Furthermore, the lateral position of the plate in the rolling gap is estimated which facilitates the adjustment of the rolling gap actuators to compensate for asymmetric loads caused by the off-centering of the plate. The contour estimation

yields the boundary contour as a series of boundary points defined in a Cartesian coordinate system. Large parts of this chapter have been published in [23] and [24].

## 2.1 Mathematical model of the movement of the plate boundary

The exit velocity of the plate leaving the rolling gap may be non-uniform along the lateral direction. This is because the plate can experience rotations with respect to its vertical axis in addition to the main longitudinal motion, as observed in [11]. The measured boundary position is thus a superposition of the plate contour and the plate movement. To analyze these effects, a mathematical model of the movement of the plate and the resulting measurement signal of the contour of the plate is deduced in this section. The algorithm is presented for one longitudinal edge of the plate and can be analogously applied to the second longitudinal edge.

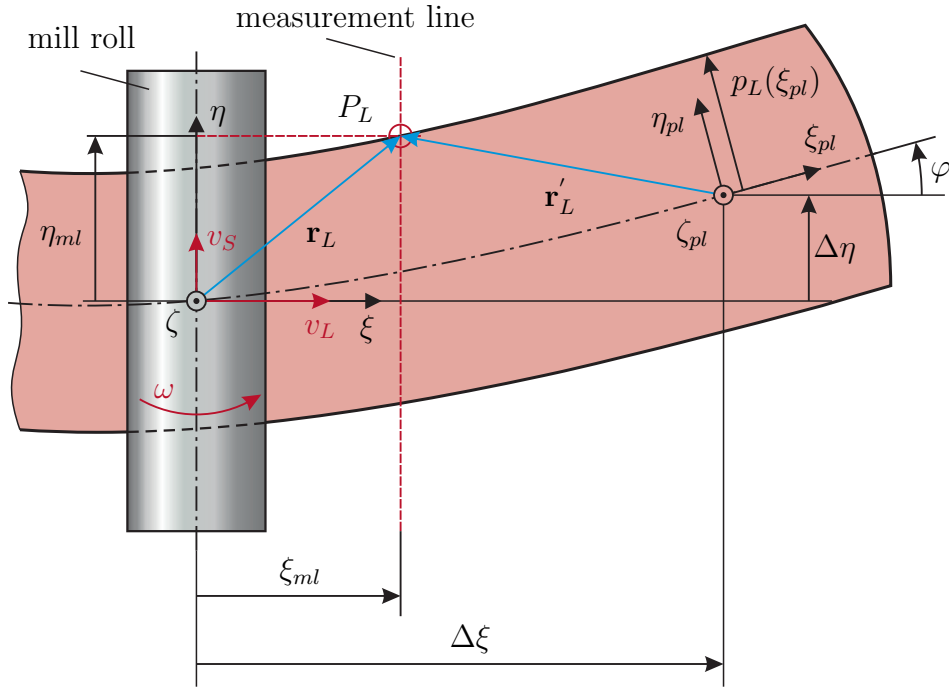


Figure 2.2: Top view of the rolling process with geometric parameterization of the plate contour.

A schematic representation of the mill roll and the rolled plate is shown in Fig. 2.2. The origin of a fixed global coordinate frame  $(\xi, \eta, \zeta)$  with base vectors  $\mathbf{e}_\xi, \mathbf{e}_\eta$  and  $\mathbf{e}_\zeta$  is located at the center of the rolling mill. At  $\xi = 0$ , the plate moves out of the rolling gap with the unknown velocity  $v_L$ .

Moreover, the velocity in the direction  $\eta$  at  $\xi = 0$  is denoted by  $v_S$ . Although  $v_S$  is generally zero because the material is clamped in the rolling gap,  $v_S$  will be taken into account in the mathematical model. The reason to introduce this velocity is that misalignments of the camera as shown in Fig. 2.3 may be present. The plate is still clamped in the rolling gap and the local velocity  $v$  of the plate is therefore perpendicular to the axis of the mill roll. Because of the misalignment of the camera and the rolls, this velocity induces a longitudinal and lateral (sideways) velocity component  $v_L$  and  $v_S$  in the  $(\xi, \eta, \zeta)$  coordinate frame. The non-zero lateral velocity  $v_S$  reduces the accuracy of the estimated contour if it is not considered in the mathematical model. Due to the assembling situation of the

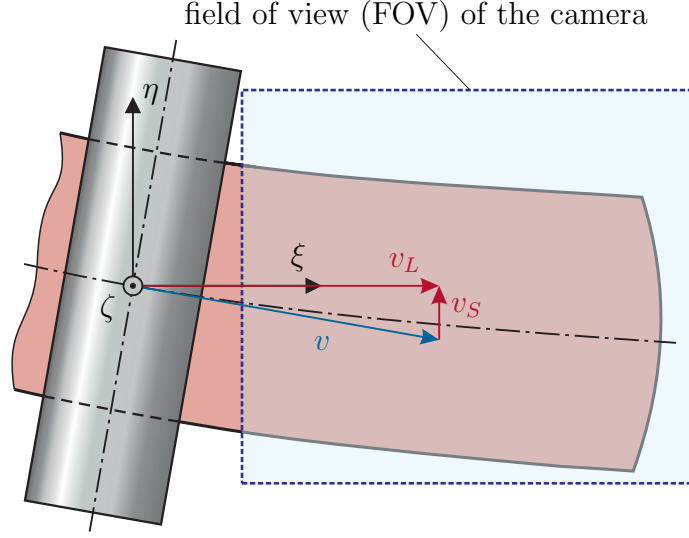


Figure 2.3: Angular misalignment of the camera and the rolls.

camera, a small but constant angular misalignment can be expected.

Furthermore, the plate contour is assumed to be constant after leaving the rolling gap. Let  $\omega$  be the angular velocity of the plate with respect to the axis  $\zeta$ . A second local coordinate frame (index  $pl$ ) that is fixed to the plate is used for parameterizing the longitudinal boundary by a polynomial

$$p_L(\xi_{pl}) = \sum_{i=0}^{N_L} c_{L,i} \xi_{pl}^i, \quad (2.1)$$

with degree  $N_L$  and so far unknown coefficients  $c_{L,i}$ . The origin of the coordinate frame  $(\xi_{pl}, \eta_{pl}, \zeta_{pl})$  is shifted by  $(\Delta\xi, \Delta\eta, 0)$  and rotated by the angle  $\varphi$  with respect to the axis  $\zeta$ . Hence, the nonlinear dynamical model of the plate movement reads as

$$\frac{d}{dt} \begin{bmatrix} \Delta\xi \\ \Delta\eta \\ \varphi \end{bmatrix} = \begin{bmatrix} v_L - \omega \Delta\eta \\ \omega \Delta\xi + v_S \\ \omega \end{bmatrix}, \quad (2.2)$$

with state vector  $\mathbf{x} = [\Delta\xi \quad \Delta\eta \quad \varphi]^\top$  and the inputs  $v_L$ ,  $v_S(t)$ , and  $\omega(t)$ .

Assume that  $P_L$  is the currently measured point on the longitudinal boundary of the plate as indicated in Fig. 2.2.  $P_L$  has the fixed distance  $\xi_{ml}$  with respect to the roll axis. In the local coordinate frame,  $P_L$  is described in vector representation as

$$\mathbf{r}'_L = [\xi_L(t) \quad \eta_L(t)]^\top = [\xi_L(t) \quad p_L(\xi_L(t))]^\top, \quad (2.3)$$

starting from the origin of the plate-fixed coordinate frame. The point  $P_L$  can also be described in the global coordinate frame with the vector

$$\mathbf{r}_L = [\xi_{ml} \quad \eta_{ml}(t)]^\top,$$

where  $\eta_{ml}(t)$  is the actual measurement signal at the considered measurement line, see Fig. 2.2. Position signals from several such measurement lines are obtained from edge detection algorithms within bitmaps of the plate, which are captured by a single infrared 2D-CCD camera mounted at the ceiling of the rolling mill building. A detailed description of the measurement setup is given in Section 2.5. The distance  $\xi_{ml}$  does not vary with time (in contrast to  $\eta_{ml}(t)$ ) because the measurement device has a fixed position and orientation in the global coordinate frame. An alternative representation of (2.3) is given by

$$\mathbf{r}'_L = \begin{bmatrix} \xi_L(t) \\ \eta_L(t) \end{bmatrix} = \mathbf{A}_\zeta(\varphi(t)) \begin{bmatrix} \xi_{ml} - \Delta\xi(t) \\ \eta_{ml}(t) - \Delta\eta(t) \end{bmatrix}, \quad (2.4)$$

where the rotation matrix  $\mathbf{A}_\zeta(\varphi(t))$  is defined in the form

$$\mathbf{A}_\zeta(\varphi(t)) = \begin{bmatrix} \cos(\varphi(t)) & \sin(\varphi(t)) \\ -\sin(\varphi(t)) & \cos(\varphi(t)) \end{bmatrix}.$$

Similar to (2.1), the head end of the plate is parameterized by the polynomial

$$p_H(\eta_{pl}) = \sum_{i=0}^{N_H} c_{H,i} \eta_{pl}^i, \quad (2.5)$$

with degree  $N_H$  and coefficients  $c_{H,i}$ . Hence, a point  $P_H$  on the head end may be written in vector representation as

$$\mathbf{r}'_H = [p_H(\eta_H(t)) \quad \eta_H(t)]^\top$$

using (2.5) or as

$$\mathbf{r}'_H = \begin{bmatrix} \xi_H(t) \\ \eta_H(t) \end{bmatrix} = \mathbf{A}_\zeta(\varphi(t)) \begin{bmatrix} \xi_{mh}(t) - \Delta\xi(t) \\ \eta_{mh} - \Delta\eta(t) \end{bmatrix} \quad (2.6)$$

in the local coordinate frame using measurements  $(\xi_{mh}(t), \eta_{mh})$  on the head end. In contrast to the measurements on the longitudinal boundaries, here the longitudinal

coordinate  $\xi_{mh}(t)$  varies with time and  $\eta_{mh}$  is constant. This is because spatially fixed measurement lines parallel to the axis  $\xi$  are used for the head end.

Note that (2.4) and (2.6) also depend on the states  $\mathbf{x}$  of the kinematic model (2.2). That is, the kinematic states  $\mathbf{x}$  constitute the link between position measurements from a camera bitmap in the global coordinate frame to a polynomial boundary representation in the local coordinate frame.

## 2.2 Optimization-based contour estimation

The challenging task of estimating the boundary of the plate also includes the estimation of the states and inputs of the system (2.2). Tailored versions of an Extended Kalman Filter (EKF), see, e. g., [30], may be used to estimate the states and the inputs of the system. But the large number of measurements (more than 1000) obtained by a single infrared camera makes the real-time execution of an EKF rather difficult due to the resulting extensive computational effort. Optimization-based state estimation is another option. An overview of this topic can be found in [31]. Because such methods are able to simultaneously estimate inputs, parameters, and states, an optimization-based approach is developed to estimate the contour and the movement of the plate (angular, lateral, and longitudinal velocity of the plate) based on the measurement signals.

### 2.2.1 Formulation of the optimization-based contour estimation

The optimization-based estimation of the contour of the plate can be divided into three parts. First, the coefficients of the polynomial (2.5) are calculated when the head end of the plate is in the field of view (FOV) of the camera for the first time. In the second part, the head end of the plate is still in the FOV, which enables the estimation of the longitudinal speed  $v_L$  of the plate. When the head end of the plate is no longer in the FOV (third part), the plate velocity in the longitudinal direction is estimated based on the approach presented in Section 2.3.

#### 2.2.1.1 Parameterization of the head end

The time  $t$  is set to zero, i. e.  $t = 0$  and the contour estimation starts when the plate length in the FOV exceeds a lower bound  $l_{min}$ . Then, the initial state of (2.2) is chosen as

$$\mathbf{x}(0) = \mathbf{x}_0 = [\xi_{ml,1} \quad 0 \quad 0]^T, \quad (2.7)$$

with  $\xi_{ml,1}$  representing the longitudinal position of the left-most measurement line of the FOV in the global coordinate frame. At this time step, the coefficients  $c_{H,i}$

of the polynomial (2.5) are calculated once by minimizing

$$\mathbf{p}_H \in \mathbb{R}^{N_H+1} \min \sum_{j=1}^{M_H} e_{H,j,0}^2(\mathbf{x}_0, 0; \mathbf{p}_H),$$

with the coefficient vector

$$\mathbf{p}_H = [c_{H,0} \quad c_{H,1} \quad \dots \quad c_{H,N_H}]^T,$$

the number  $M_H$  of rows used from the camera bitmap, and the (longitudinal) offset

$$e_H(\mathbf{x}(t), t; \mathbf{p}_H) = p_H(\eta_H(t)) - \xi_H(t) \quad (2.8)$$

between a measured point  $(\xi_{mh}(t), \eta_{mh})$  at the head end and its representation (2.6) in the least-squares sense.

### 2.2.1.2 Optimization problem with a head end in the FOV

A convenient method for determining the unknown polynomial coefficients  $c_{L,i}$  of the longitudinal boundary is to minimize the lateral offset  $e_L(\mathbf{x}(t), t; \mathbf{p}_L)$  between a measured boundary point  $(\xi_{ml}, \eta_{ml}(t))$  and its representation (2.3) during a certain time period. At the time  $t$ , this error is defined as

$$e_L(\mathbf{x}(t), t; \mathbf{p}_L) = p_L(\xi_L(t)) - \eta_L(t) \quad (2.9)$$

with the coefficient vector

$$\mathbf{p}_L = [c_{L,0} \quad c_{L,1} \quad \dots \quad c_{L,N_L}]^T \quad (2.10)$$

of the boundary polynomial (2.1). Additionally, the longitudinal offset (2.8) may be minimized to estimate the velocity  $v_L$  using the determined coefficient vector  $\mathbf{p}_H$  from Section 2.2.1.1 during a certain time period. The unknown velocity  $v_L$  is assumed to be constant during this time period.

Contrary to Section 2.2.1.1, a dynamic optimization problem has to be solved to minimize the longitudinal and lateral offset. The optimization problem, which is formulated in the plate-fixed coordinate frame, is used to estimate the unknowns  $\omega(t)$ ,  $v_S(t)$ ,  $\mathbf{p}_L$ , and  $v_L$ . In order to obtain a static optimization problem, (2.2) is discretized using the zero-order-hold scheme and a fixed sampling time  $T_s$ . Based on the assumptions  $\omega(t) = \omega_k$  and  $v_S(t) = v_{S,k}$  during a sampling interval  $kT_s \leq t < (k+1)T_s$ , (2.2) can be analytically solved. This yields the discrete-time

system

$$\begin{aligned} \mathbf{x}_{k+1} &= \begin{bmatrix} \Delta\xi_k \cos(\omega_k T_s) - \Delta\eta_k \sin(\omega_k T_s) \\ \Delta\xi_k \sin(\omega_k T_s) + \Delta\eta_k \cos(\omega_k T_s) \\ \varphi_k + \omega_k T_s \end{bmatrix} + \frac{v_L}{\omega_k} \begin{bmatrix} \sin(\omega_k T_s) \\ 1 - \cos(\omega_k T_s) \\ 0 \end{bmatrix} \\ &+ \frac{v_{S,k}}{\omega_k} \begin{bmatrix} \cos(\omega_k T_s) - 1 \\ \sin(\omega_k T_s) \\ 0 \end{bmatrix} \\ &= \mathbf{f}(\mathbf{x}_k, \omega_k, v_{S,k}, v_L) \end{aligned} \quad (2.11)$$

with the state  $\mathbf{x}_k = \mathbf{x}(kT_s) = [\Delta\xi_k \ \Delta\eta_k \ \varphi_k]^\top$ ,  $k \in \mathbb{N}_0$ .

Hence, the static optimization problem can be formulated as

$$\begin{aligned} &\min_{\substack{\boldsymbol{\omega} \in \mathbb{R}^N \\ \mathbf{v}_S \in \mathbb{R}^N \\ \mathbf{p}_L \in \mathbb{R}^{N_L+1} \\ v_L}} \underbrace{\sum_{k=0}^N \sum_{j=1}^{M_L} e_{L,j,k}^2(\mathbf{x}_k; \mathbf{p}_L) + \sum_{k=0}^N \sum_{j=1}^{M_H} e_{H,j,k}^2(\mathbf{x}_k)}_{J(\boldsymbol{\omega}, \mathbf{v}_S, \mathbf{p}_L, v_L)} \end{aligned} \quad (2.12a)$$

$$\text{subject to } \mathbf{x}_{k+1} = \mathbf{f}(\mathbf{x}_k, \omega_k, v_{S,k}, v_L) \quad (2.12b)$$

with the abbreviations

$$\begin{aligned} e_{L,j,k}(\mathbf{x}_k; \mathbf{p}_L) &= p_L \left( \underbrace{(\xi_{ml,j} - \Delta\xi_k) \cos(\varphi_k) + (\eta_{ml,j,k} - \Delta\eta_k) \sin(\varphi_k)}_{\xi_{L,j,k}} \right) \\ &- \left( \underbrace{(\eta_{ml,j,k} - \Delta\eta_k) \cos(\varphi_k) - (\xi_{ml,j} - \Delta\xi_k) \sin(\varphi_k)}_{\eta_{L,j,k}} \right) \end{aligned} \quad (2.13)$$

and

$$\begin{aligned} e_{H,j,k}(\mathbf{x}_k) &= p_H \left( \underbrace{(\eta_{mh,j} - \Delta\eta_k) \cos(\varphi_k) - (\xi_{mh,j,k} - \Delta\xi_k) \sin(\varphi_k)}_{\eta_{H,j,k}} \right) \\ &- \left( \underbrace{(\xi_{mh,j,k} - \Delta\xi_k) \cos(\varphi_k) + (\eta_{mh,j} - \Delta\eta_k) \sin(\varphi_k)}_{\xi_{H,j,k}} \right). \end{aligned} \quad (2.14)$$

The optimization variables are the coefficient vector  $\mathbf{p}_L$ , the vector of the angular velocities  $\boldsymbol{\omega} = [\omega_0 \ \omega_1 \ \dots \ \omega_{N-1}]^\top$ , the vector of the lateral velocities  $\mathbf{v}_S = [v_{S,0} \ v_{S,1} \ \dots \ v_{S,N-1}]^\top$ , and the longitudinal velocity of the plate  $v_L$ .  $M_L$  is the number of columns used from the camera bitmap. If no measurement  $(\xi_{ml,j}, \eta_{ml,j,k})$  is available at a certain time step  $k$  and measurement line  $j$ ,  $e_{L,j,k}(\mathbf{x}_k; \mathbf{p}_L)$  is set to zero. Similarly,  $e_{H,j,k}(\mathbf{x}_k)$  is set to zero if the head end of the plate is no longer



in the FOV of the camera. The considered time period ranges from  $t = 0$  to  $t = NT_s$ , i. e., there are  $N + 1$  sampling points and the optimization involves  $N$  values of  $\omega_k$  and  $v_{S,k}$ .

**Remark 2.1** *To estimate the contour polynomial and the movement of the plate, at least two measurement lines ( $M_L \geq 2$ ) at significantly different positions  $\xi_{ml,j}$  must be used. However, a larger number of measurements improves the robustness of the estimation as noise is suppressed by averaging.*

### 2.2.1.3 Optimization problem without a head end in the FOV

If the head end of the plate is already outside the FOV of the camera, the presented approach does not allow the estimation of the longitudinal speed  $v_L$  of the plate. Hence,  $v_L$  is obtained by a different estimation approach described in Section 2.3 and the optimization problem (2.12) simplifies to

$$\begin{aligned} \min_{\substack{\boldsymbol{\omega} \in \mathbb{R}^N \\ \mathbf{v}_S \in \mathbb{R}^N \\ \mathbf{p}_L \in \mathbb{R}^{N_L+1}}} & \sum_{k=0}^N \sum_{j=1}^{M_L} e_{L,j,k}^2(\mathbf{x}_k; \mathbf{p}_L) \end{aligned} \quad (2.15a)$$

$$\text{subject to } \mathbf{x}_{k+1} = \mathbf{f}(\mathbf{x}_k, \omega_k, v_{S,k}, v_L). \quad (2.15b)$$

## 2.2.2 Numerical solution of the optimization problem

In this subsection, the numerical solution of the optimization problem (2.12) is discussed. The presented approach can be analogously applied to the optimization problem (2.15) by omitting the optimization variable  $v_L$ . For a compact notation, all optimization variables are assembled in the vector

$$\mathbf{w} = \begin{bmatrix} \boldsymbol{\omega} \\ \mathbf{v}_S \\ \mathbf{p}_L \\ v_L \end{bmatrix} = [w_0 \ w_1 \ \dots \ w_{2N+N_L+1}]^T$$

and the objective function is written in the form  $J(\mathbf{w}) = J(\boldsymbol{\omega}, \mathbf{v}_S, \mathbf{p}_L, v_L)$ . The optimization problem is solved using the quasi-Newton method presented in Appendix A.2 and the line search from Appendix A.4.2. The quasi-Newton method proved to be more useful than the Gauss-Newton method because of the large number of addends in the objective function. This would lead to large matrices when using the Gauss-Newton method and hence to larger optimization times. The gradient of the objective function with respect to the optimization variables may be calculated by numerical differentiation. For the given optimization problem, however, the gradient is calculated analytically as described in Appendix B. Compared to the use of numerical differentiation, this leads to a more accurate

calculation of the gradient and hence to a faster convergence of the optimization algorithm (cf. [32]).

Three different termination criteria are used:

- The gradient  $\mathbf{g}_l$  is sufficiently small, i. e.,  $\|\mathbf{g}_l\|_\infty < \gamma_g(1 + \|\mathbf{g}_0\|_\infty)$  with a tuning parameter  $\gamma_g > 0$ .
- The step size is sufficiently small, i. e.,  $\|\mathbf{w}_{l+1} - \mathbf{w}_l\|_\infty < \gamma_x$  with a parameter  $\gamma_x > 0$ .
- The achieved improvement of the objective function value  $J$  along the current search direction is smaller than the constant  $\gamma_{dJ} > 0$ , i. e.,  $J(\mathbf{w}_l) - J(\mathbf{w}_{l+1}) < \gamma_{dJ}$ .

Properly chosen values for  $\gamma_g$ ,  $\gamma_x$ , and  $\gamma_{dJ}$  ensure both, a sufficiently accurate optimization result and a low number of iterations.

### 2.3 Estimation of the plate velocity

With the approach from Section 2.2, the rolling speed can only be estimated as long as the head end of the plate is in the FOV of the camera. In general, the rolling speed is held constant during the pass. Hence, the plate speed estimated for the head end could also be used for the remaining part of the plate. However, the assumption of a constant plate speed may only hold true as long as the plate is clamped in the rolling gap. After the plate has left the rolling gap, the velocity of the plate is influenced by the rotational speed of the roller table. Furthermore, the operator may change the rolling speed during the rolling pass. Consequently, it is necessary to estimate the velocity of the plate during the whole contour estimation process. One method to determine the velocity is to add a velocity sensor. This sensor should be located as near as possible to the rolling gap because the velocity of short plates should also be measured. However, such a configuration may be affected by steam, dust, and heat and requires costly robust sensors. To avoid these costs, a method to determine the velocity using the images of the already installed thermographic camera is presented.

As shown in Fig. 2.4, the surface temperature distribution  $T(\xi, \eta)$  is generally non-uniform. These inhomogeneities may be caused by non-uniform heating in the slab furnace or inhomogeneous conditions during the rolling process and are in general unfavorable. However, non-uniform plate temperatures along the direction  $\xi$  can be useful for determining the velocity of the plate by the method proposed in the following.

As a preparatory step, the mean surface temperature in lateral direction

$$\bar{T}(\xi_j, t_k) = \frac{1}{L+1} \sum_{i=\bar{L}-L/2}^{\bar{L}+L/2} T(\xi_j, \eta_i) \Big|_{t=t_k} \quad (2.16)$$

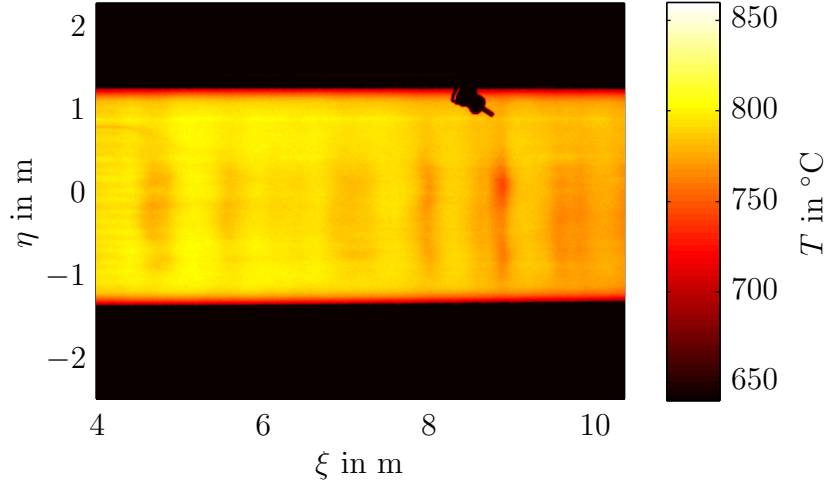


Figure 2.4: Thermographic image of a heavy plate with a spatially fixed disturbance (pyrometer).

of the image captured at time  $t_k = kT_s$  is calculated. The averaging in (2.16) utilizes a rectangular section of the image with  $L + 1$  rows symmetric to the row  $\bar{L}$ . Note that spatially fixed systematic disturbances, e. g., the pyrometer, must not be contained in this section of the image. Instead of the mean temperature distribution, it would also be possible to use the temperature values from a single row of the image. However, the larger number of measurements improves the robustness of the estimation against noise and local disturbances.

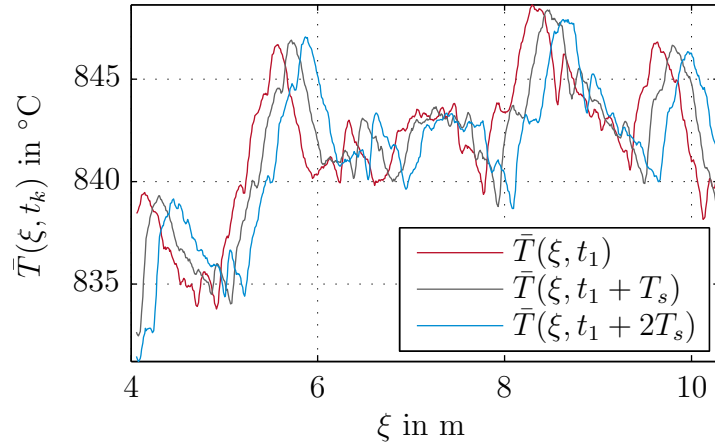


Figure 2.5: Mean temperature distribution for three consecutive images.

As an example, the resulting longitudinal temperature distribution for three consecutive images with  $L = 20$  is shown in Fig. 2.5. Since the images are captured with a high frame rate, the temperature of the plate of consecutive images is almost the same. The figure suggests that there is only a spatial shift of a more or less constant temperature distribution. In this case, the shift  $\Delta s$  between the

temperature distributions can be determined, e. g., by using the cross correlation function (see, e. g., [33]). Assuming a constant velocity within a sampling time  $T_s$ , the velocity of the plate  $v_L$  then follows as

$$v_L = \frac{\Delta s}{T_s}. \quad (2.17)$$

However, the temperature distribution is subject to minor changes and disturbances. Possible reasons are heat conduction processes or image distortions caused by the camera lens. Such disturbances entail additional deviations between the shifted temperature profiles and therefore deteriorate the velocity estimation, unless they are systematically considered in the estimation approach. From experience, it is known that these distortions depend on the spatial coordinate  $\xi$  of the image. Therefore, the empirical correction approach

$$\hat{T}(\xi, t_k) = p(\xi)\bar{T}(\xi, t_k), \quad (2.18)$$

with a polynomial scaling function

$$p(\xi) = \sum_{i=0}^{P_V} b_i \xi^i \quad (2.19)$$

with degree  $P_V$  and so far unknown coefficients  $b_i$ , is employed to compute a corrected temperature distribution  $\hat{T}(\xi, t_k)$ . As the averaged temperature distribution (2.16) is only defined at the spatial grid points of the bitmap, a linear interpolation is performed in (2.18) between the pixels to achieve sub-pixel resolution.

A convenient method for determining the velocity of the plate and the unknown polynomial coefficients  $b_i$  in (2.19) is to minimize the difference  $e(\xi, t_k; \Delta s, \mathbf{p})$  between consecutive temperature distributions. At the time  $t_k$ , this error is defined as

$$e(\xi, t_k; \Delta s, \mathbf{p}) = \hat{T}(\xi - \Delta s, t_k - T_s) - \hat{T}(\xi, t_k) \quad (2.20)$$

$\forall \xi \in [\Delta s_{max}, l_{fov} - \Delta s_{max}]$  with the coefficient vector  $\mathbf{p} = [b_1 \ b_2 \ \dots \ b_{P_V}]^T$  and the length  $l_{fov}$  of the FOV of the camera. The term  $\Delta s_{max} = v_{L,max} T_s$  represents the maximal expected shift as a function of the maximal rolling speed  $v_{L,max}$ .

The first coefficient is chosen as  $b_0 = 1$  because it would only scale the temperature distribution  $\bar{T}$  by a constant factor. Hence, a static optimization problem can be formulated as

$$\min_{\Delta s, \mathbf{p} \in \mathbb{R}^{P_V}} \sum_{k=1}^{N_V-1} \sum_{j=1}^{M_V} e^2(\xi_j, t_k; \Delta s, \mathbf{p}) \quad (2.21)$$

using  $M_V$  grid points and  $N_V$  images. Note that only the spatially overlapping parts of the temperature difference in (2.20) are used in (2.21), i. e.,  $\xi_j \in [\Delta s_{max}, l_{fov} - \Delta s_{max}]$ . Clearly, an implicit assumption made here is that  $v_L$  is constant during the time interval  $t_0 \leq t \leq t_{N_V-1}$ . Therefore, the time interval should not be too large. On the other hand, increasing the number  $N_V$  of consecutive images reduces noise in the estimation result, which is why a compromise has to be found. Once the optimization problem (2.21) is solved, the velocity of the plate follows from (2.17). The optimization problem is solved using the Gauss-Newton method from Appendix A.3, the line search from Appendix A.4.2, and the optimization variables  $\mathbf{w} = [\Delta s \quad \mathbf{p}^T]^T$ . The algorithm terminates if the maximum number of iterations is exceeded or the convergence criterion  $\|\mathbf{w}_{l+1} - \mathbf{w}_l\|_\infty < \gamma_V$  with a properly chosen constant  $\gamma_V > 0$  is fulfilled.

The derivative of  $e(\xi_j, t_k; \Delta s, \mathbf{p})$ ,  $j = 1, \dots, M_V$  and  $k = 1, \dots, N_V - 1$  with respect to  $\Delta s$  is required in the Gauss-Newton algorithm and is calculated using a Savitzky-Golay filter, see, e. g., [33], with degree 2 and window length 11.

## 2.4 Receding horizon approach

With the method proposed so far, the contour is estimated based on the whole set of measurements in one go after the plate has left the rolling gap. This global approach has two drawbacks:

1. There is a large number of optimization variables, which increases with the number of images used, leading to large computing times when solving the associated optimization problems, e. g., (2.12).
2. The contour information is only available after the rolling pass has finished. Thus, the contour information cannot be utilized for feedback control in the same pass.

These problems are avoided if the optimization routine is applied to overlapping sections along the plate. Such a receding horizon approach reduces the number of optimization variables and provides almost real-time contour information.

The beginning of the optimization procedure is outlined in Fig. 2.6, where the plate is shown at 2 different times. At any time, the FOV of the 2D-camera remains the same. As indicated in the upper part of Fig. 2.6, the first optimization starts at  $t = 0$  when the plate length in the FOV exceeds a lower bound  $l_{min}$ . The starting point of the optimization at the boundary of the plate is marked with a cross and the end point is marked with a circle. As the plate leaves the rolling gap with the speed  $v_L$ , the starting points (crosses) move through the FOV, i. e., they are fixed to the corner points of the plate. The end points (circles), however, have a fixed coordinate  $\xi$ , i. e. the circles move along the boundary as seen from a plate-fixed point of view. Therefore, the optimization horizon and hence the

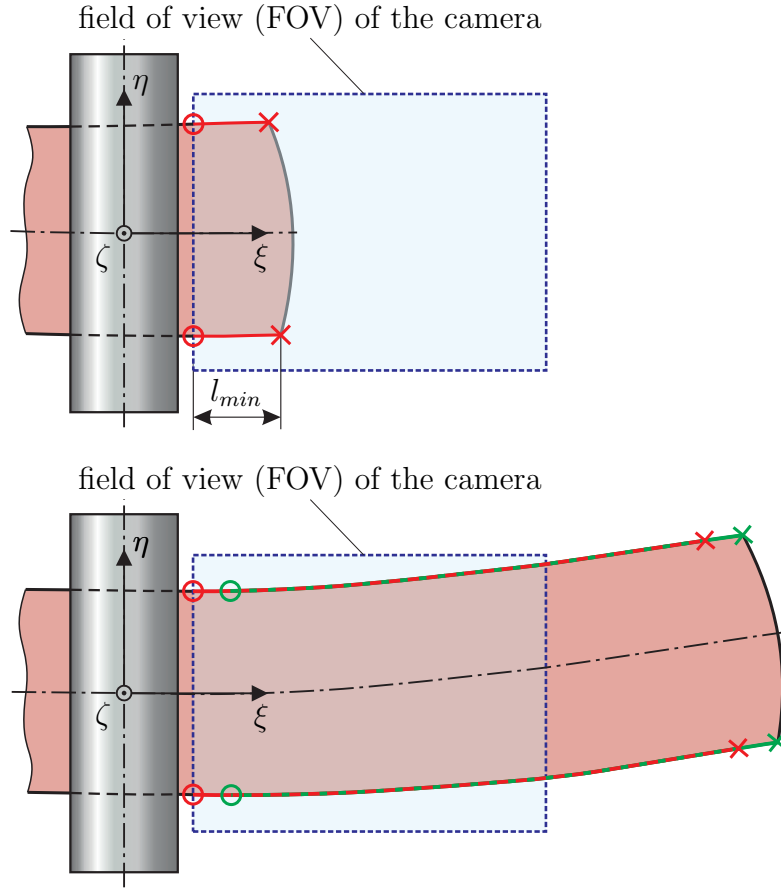


Figure 2.6: Receding horizon approach for the proposed contour estimation method.

number of optimization variables increases in every time step. This continues until the maximum number  $N$  of images used in one optimization horizon is reached. From this time onwards, the dimension of the optimization problem does not change anymore. Therefore, for every additionally captured image, the oldest image in the measurement set is discarded.

As indicated in the lower part of Fig. 2.6, the optimization regions are overlapping. In this case, the estimated boundary from the first optimization is shown in green. Without this spatial overlap, discontinuities at the junction of the optimization regions could occur. Nevertheless, a small but negligible deviation between the resulting contours of subsequent optimization horizons is present. It is defined that the overlapping part of the result from the most recent optimization overwrites the result from the previous run. In case of the example from the lower part of Fig. 2.6, the current estimate of the longitudinal boundaries consists of the green line between the red and green cross plus the whole red line.

The results of the actual optimization for  $v_L$  and the coefficients of the boundary polynomial  $p_L$  are taken as initial guess for the subsequent optimization. The

other optimization variables are initialized with zero. The contour estimation procedure stops when the tail end is detected. At this time step, the tail-contour is added to the already estimated contour to obtain the whole plate boundary.

**Remark 2.2** *With increasing plate length, also  $\Delta\xi_k$  increases. For large values  $\Delta\xi_k \gg 1$  and boundary polynomials  $p_L$  with a high degree  $N_L$ , the Hessian  $\nabla^2 J(\mathbf{w})$  and therefore the optimization problem become ill-conditioned. This property may be challenging in terms of the numerical solution of the optimization problem. An easy countermeasure is to regularly shift the plate-fixed local coordinate frame  $(\xi_{pl}, \eta_{pl}, \zeta_{pl})$  to a new position closer to the FOV and to reset the rotation of the coordinate frame to zero. Then, the estimated contour consists of different polynomials belonging to the respective optimization region. The parameters which define the displacements and the rotations of the coordinate frames have to be stored so that the whole contour can be assembled at the end of the rolling pass.*

## 2.5 Recording and processing of image data

The proposed optimization algorithm requires measurement pairs  $(\xi_{ml,j}, \eta_{ml,j,k})$ ,  $j = 1, \dots, M_L$  and  $k = 0, \dots, N$ , to estimate the plate contour. For the head end based estimation of the longitudinal velocity  $v_L$  of the plate, measurements  $(\xi_{mh,j,k}, \eta_{mh,j,k})$ ,  $j = 1, \dots, M_H$  and  $k = 0, \dots, N$ , from the head end of the plate are required. One possible measurement principle is to extract the actual plate boundary from a 2D-image that is taken by a 2D-infrared CCD camera mounted above the plate. It is thus natural to select a sampling time  $T_s$  that equals the frame rate of the camera or that is at least an integer multiple of it. The advantage of using a 2D-camera instead of a line scan device is that several measurement lines (depending on the camera resolution) are concurrently recorded. Furthermore, a single 2D-camera is cheaper than several line scan devices.

Compared to a standard color 2D-CCD camera, infrared cameras are superior for the considered application due to the following properties:

- Objects can be captured through a cloud of steam.
- The thermal contrast between the plate and its environment is high and therefore no illumination is needed.
- There is no disturbance of the images due to other light sources, e. g. sunlight.

The first property is beneficial for the subsequent edge detection because the plate may be covered by a cloud of steam resulting from cooling water sprayed onto the plate during the rolling process. Furthermore, the high thermal contrast (cf. Fig. 2.7) enables a simple threshold based edge detection. Clearly, visible light cameras are suffering from disturbing light sources leading to falsely detected edges, see, e. g., [3]. However, disturbing light sources are seldom in the measured infrared

range of the thermographic camera. Additionally, the temperature distribution of the surface of the plate can be used for process monitoring and process control.

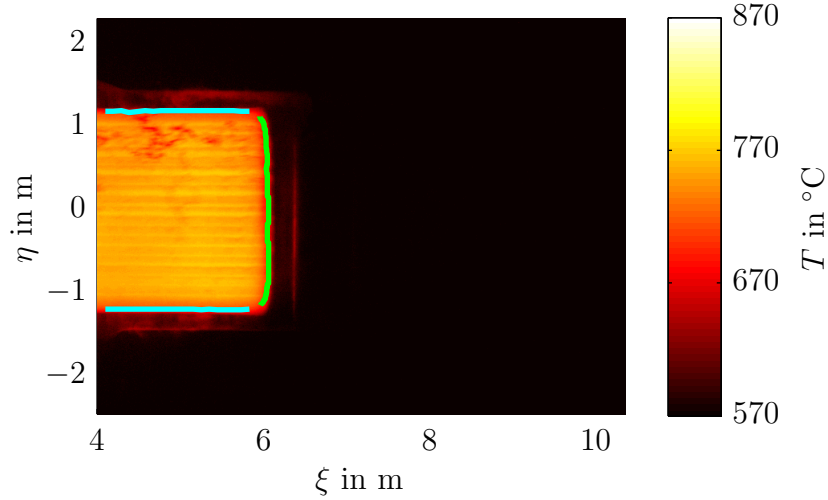


Figure 2.7: Bitmap of the temperature distribution of a rolled plate and currently detected edges (blue: longitudinal edges, green: lateral edge).

Fig. 2.8 shows the necessary tasks to estimate the plate contour. The camera is connected via a Gigabit Ethernet interface to a PC and addressed using the so called pylon API (Application Programming Interface) from the company Basler. The pylon API is based on the GenICam standard and allows an interface-independent control of the camera in the user application. Furthermore, the API allows to change a large number of parameters of the camera.

An important parameter is the exposure time of the CCD camera which has to be properly chosen to get high-contrast images. Especially when the plate enters the FOV, the exposure time should be quickly adjusted to a suitable value to ensure a reliable contour estimation at the beginning of the rolling pass. The camera features an automatic control of the exposure time. Here, the exposure time is adjusted until an average intensity of an area of interest (AOI) is reached.

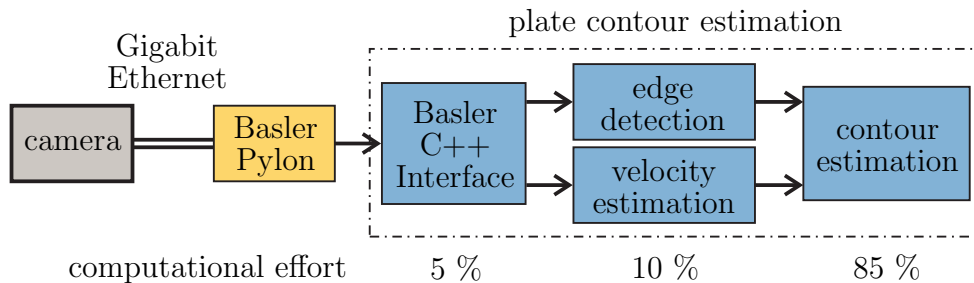


Figure 2.8: Necessary tasks and their computational effort for the estimation of the plate contour.



The area of interest is set to a rectangular region where the plate first enters the FOV. This selection ensures a fast settling of the controlled exposure time after the plate has entered the FOV.

The pylon API provides the image data in the form of an intensity distribution (12-bit resolution) of the detected infrared radiation. Instead of the temperature bitmap, the intensity bitmap is utilized for detecting the edges. This is favorable because the intensity features similar transitions from the hot plate to the cold surrounding area even for different temperature levels. Furthermore, there exists a huge intensity gradient between the plate and the surrounding area. The longitudinal and lateral edges of the plate are expected to be nearly parallel to the  $\xi$ -axis and the  $\eta$ -axis, respectively. These properties offer a simple edge detection approach based on an intensity threshold  $I_{th}$ . It is set to

$$I_{th} = I_{min} + k_{rel} (I_{max} - I_{min}),$$

with the minimum  $I_{min}$  and the maximum  $I_{max}$  of the intensity  $I$  in the considered image. The relative threshold  $k_{rel} \in [0, 1]$  is a user-defined constant. In every column of the image, the two outermost pixels where the threshold  $I_{th}$  is exceeded determine the longitudinal edges of the plate. A tail or head end is detected analogously by processing the rows of the image.

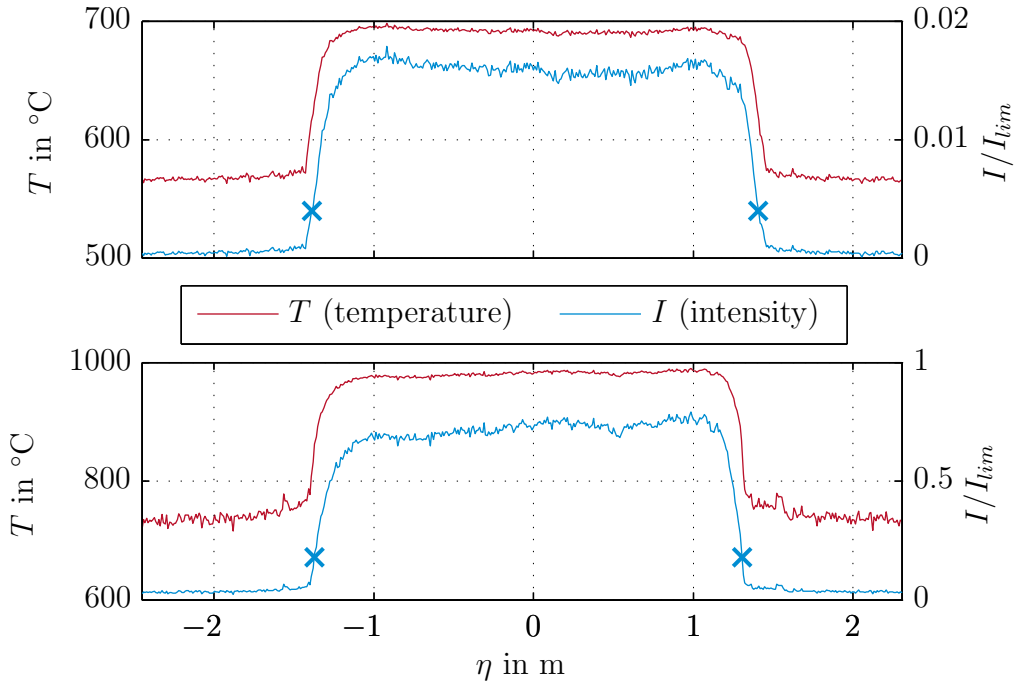


Figure 2.9: Intensity distribution normalized to the upper measurement limit  $I_{lim}$  of the infrared camera and temperature distribution of a cold and a hot plate as well as detected edge pixels for  $k_{rel} = 0.2$ .

Fig. 2.9 shows the intensity distribution of a single row of the bitmap for two different plates. The upper part of Fig. 2.9 shows the intensity of a cold plate and in the lower part a very hot plate is shown. Both plates feature a steep slope from the outside margin of the plate to its inner part which turned out to be characteristic. The parameter  $k_{rel}$  is chosen so that the detected edge pixels are in the region of the steep slope. The detected edge pixels for  $k_{rel} = 0.2$  are marked with crosses in Fig. 2.9.

**Remark 2.3** *The intensity is linked with the temperature by the Stefan-Boltzmann law  $I = \sigma T^4$ , where  $\sigma$  denotes the Stefan-Boltzmann constant (cf. [34]). Hence, an equivalent temperature threshold could alternatively be calculated and the edge detection could be performed using the temperature bitmap. However, the relation between the intensity measured by the camera and the temperature deviates from Stefan-Boltzmann's law because of imperfections of the intensity measurement. The mapping used in the software of the camera is generally not known which hampers a temperature based edge detection.*

Compared to standard algorithms for the detection of edges such as the Canny algorithm, see, e. g., [35], the presented approach requires smaller computational times and an inherent separation in longitudinal and lateral edges. The results of the edge detection algorithm and the velocity estimation from Section 2.3 are finally fed into the contour estimation from Section 2.2. Fig. 2.8 indicates the relative computational effort of the different processing tasks.

## 2.6 Validation and statistics

In the following, results for the estimated contour of a plate rolled in an industrial rolling mill of AG der Dillinger Hüttenwerke, Germany are given. An infrared 2D-CCD camera was installed 25 m above the pass-line level at the ceiling of the building before and after the finishing mill. This isolates the cameras from oscillations and harsh conditions (heat, dust, cooling water) near the rolling process. Using a 25 mm lens, a spatial resolution of 9.6 mm/pixel is achieved. The industrial IR camera used in this work captures 30 frames/s with an image resolution of 659 x 494 pixels.

The developed measurement system has proven to be robust against the harsh conditions at the rolling mill for the last two years without any maintenance. Measurement data from a contour measurement device (CMD) located at the downstream end of the production line is used to validate the estimated contour. This contour measurement is performed by means of a laser line scanner and some image processing algorithms. The scanner is arranged across the roller table. It captures images (1D arrays) as the plate is conveyed on the roller table along a strictly straight path (no rotation of the plate). The image frames are joined by software to generate a full 2D picture of the plate contour.

Parameter	Value	Parameter	Value	Unit
$N_L$	3	$k_{rel}$	0.2	
$N_H$	4	$T_s$	1/30	s
$N$	10	$l_{min}$	3	m
$M_L$	659	$\xi_{ml,1}$	4	m
$M_H$	100	$\gamma_g$	$10^{-10}$	
$L$	20	$\gamma_x$	$10^{-8}$	
$\bar{L}$	494/2	$\gamma_{dJ}$	$10^{-3}$	
$M_V$	659	$\gamma_V$	$10^{-3}$	
$N_V$	5	$l_{fov}$	6.3475	m

Table 2.1: Parameters used for the estimation of the plate contour.

The optimization problem (2.12) was implemented in C++ utilizing the linear algebra packages LAPACK and BLAS to speed up matrix and vector calculations. When considering both longitudinal edges of the plate, the optimization variables  $\mathbf{w}$  read as

$$\mathbf{w} = \left[ \boldsymbol{\omega}^T \quad \mathbf{v}_S^T \quad \mathbf{p}_{L,left}^T \quad \mathbf{p}_{L,right}^T \quad v_L \right]^T,$$

with the coefficient vectors  $\mathbf{p}_{L,left}$  and  $\mathbf{p}_{L,right}$  (cf. (2.1) and (2.10)) of the boundary polynomials for the left and the right longitudinal boundary as seen in rolling direction, respectively.

The initial guess  $\mathbf{w}_0$  is chosen as  $\boldsymbol{\omega}_0 = \mathbf{0}$ ,  $\mathbf{v}_{S,0} = \mathbf{0}$ , and  $v_{L,0} = 3$  m/s (common rolling speed). The first entries of  $\mathbf{p}_{L,left}$  and  $\mathbf{p}_{L,right}$  (constant terms of the polynomials) are set to the mean values of the respective edge in the first detected image. All other elements of  $\mathbf{p}_{L,left}$  and  $\mathbf{p}_{L,right}$  are initially set to 0.

A crucial parameter for the estimation accuracy is the chosen length  $N$  of the optimization horizon. A larger value of  $N$  results in a smoother estimated contour due to averaging. This is because of a better suppression of noise in the detected contour. Clearly,  $N$  also controls the time needed for solving the optimization problem. The actual choice of  $N$  is therefore a tradeoff between a sufficiently smooth contour and a reasonable computing time. For the considered measurement configuration,  $N = 10$  proved to be a good compromise. The remaining parameters used for the contour estimation are shown in Tab. 2.1. With these parameters, it takes less than 0.025 s (Standard PC with i7-2600 @ 3.4 GHz processor and 16 GB RAM) to solve the optimization problem (2.12) for one optimization horizon and thus facilitates contour estimation in real-time.

A requirement to achieve short optimization times is a good convergence rate of the method used to solve the optimization problem. Hence, the convergence properties for a single optimization horizon of the proposed optimization approach are analyzed. To prevent the optimization from premature termination, the

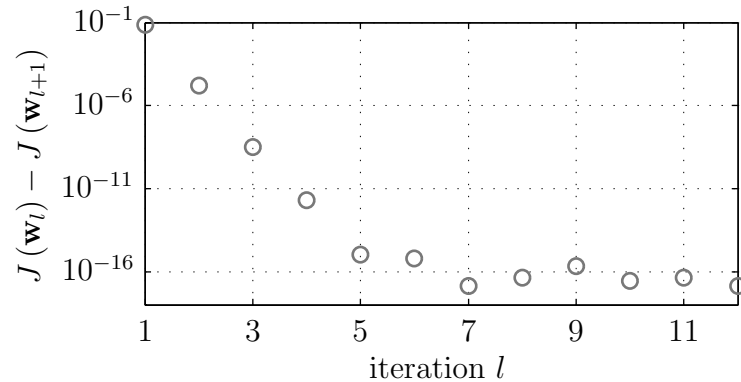


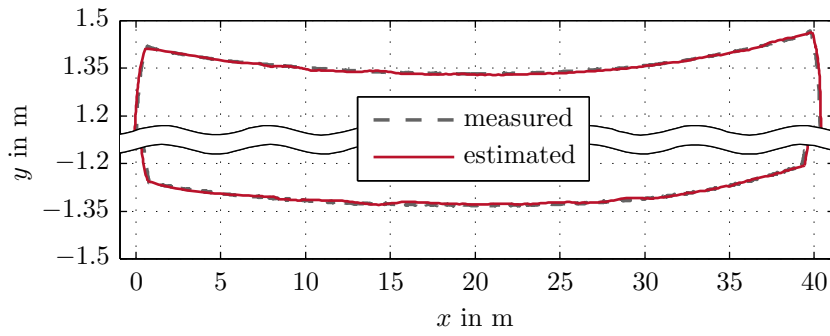
Figure 2.10: Decrease of  $J(\mathbf{w}_l)$  as a function of the iteration  $l$ .

termination criteria are temporarily set to  $\gamma_g = \gamma_x = \gamma_{dJ} = 0$ . Fig. 2.10 shows the decrease of the objective function  $J(\mathbf{w}_l)$  in every iteration  $l$ . The objective function value converges within only 5 iterations to the magnitude of machine precision ( $\approx 2.26 \cdot 10^{-16}$ ). When using the parameters from Tab. 2.1, the convergence criteria would have been already fulfilled after the second iteration. This shows that the convergence properties of this algorithm are quite good for the considered optimization problem. An important prerequisite for this behavior is the choice of the initial Hessian according to (A.4). Contrary, the initial guess  $\mathbf{w}_0$  of the optimization variables only slightly affects the convergence of the algorithm.

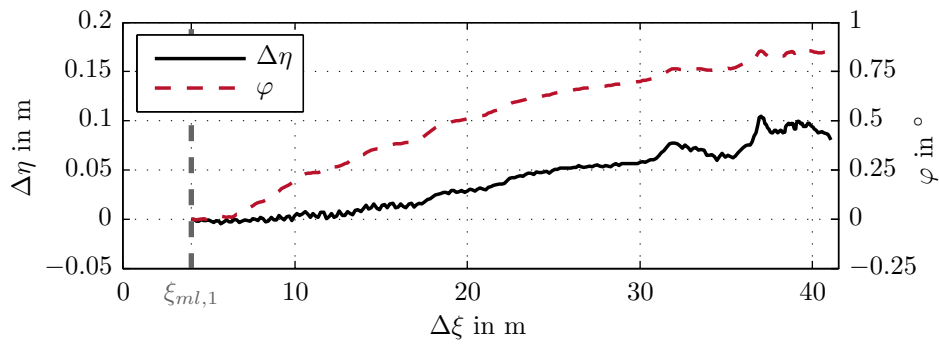
Fig. 2.11a shows the contour of the plate both measured by the downstream CMD and estimated by the proposed algorithm. The estimated contour is rotated and shifted to allow a comparison with the measured contour in the coordinate frame  $(x, y)$  of the CMD. The figure indicates a good accuracy of the contour estimation in the range of one centimeter in lateral direction. Also the shapes of the head and tail edges as well as the length of the plate are accurately estimated.

**Remark 2.4** In Fig. 2.11b - 2.11d, the longitudinal displacement  $\Delta\xi$  of the plate-fixed coordinate frame starts at  $\Delta\xi = \xi_{ml,1} = 4\text{ m}$  because of the chosen initial condition (2.7) and the parameters of the used measurement setup (cf. Tab. 2.1).

Fig. 2.11b shows the movement of the plate in the form of the position and orientation of the plate-fixed coordinate frame. In Fig. 2.11c, the estimated velocity  $v_S$  in lateral direction is shown. Although there are oscillations, they are not disturbing the estimation of the contour. This is because the lateral deviations resulting from these oscillations are very small, i. e., they are less than half a centimeter and therefore less than half of the width of a pixel. They could be caused by vibrations of the camera in lateral direction. Furthermore, the estimated longitudinal velocity  $v_L$  of the plate is shown in Fig. 2.11d. As mentioned in Section 2.2.1,  $v_L$  can only be estimated in conjunction with the contour as long as the head end of the plate is in the FOV of the camera. Therefore, the estimation approach from Section 2.3 is used for the remaining part of the plate.



(a) Measured and estimated contour.



(b) Position and orientation of the plate-fixed coordinate frame.

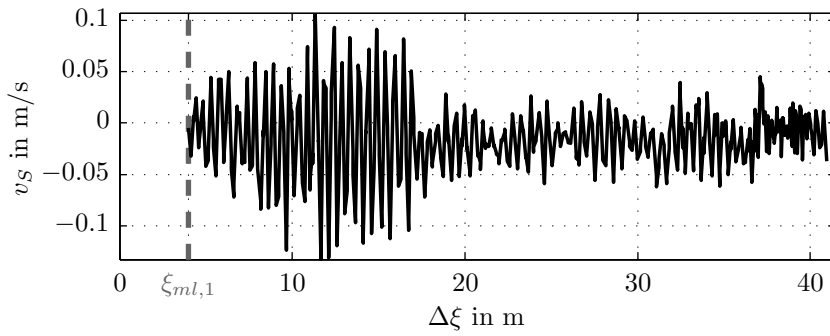
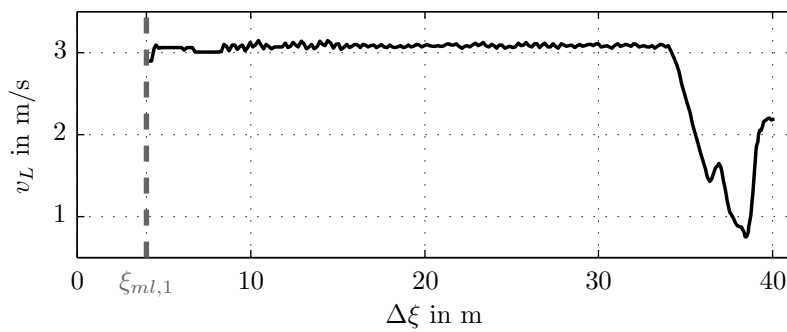
(c) Lateral velocity  $v_S$  of the plate.(d) Longitudinal velocity  $v_L$  of the rolled plate.

Figure 2.11: Measurement and estimation results for a rolled plate.

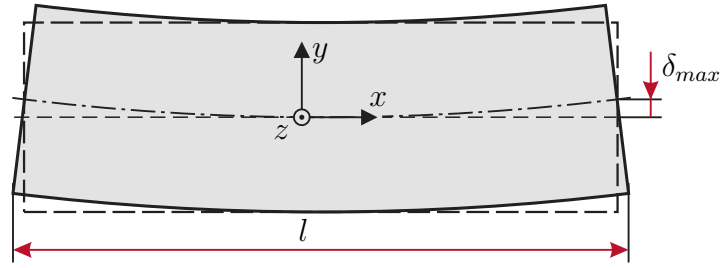


Figure 2.12: Definition of the maximum lateral deviation  $\delta_{max}$  and the length of the plate  $l$ .

The deceleration of the plate at the end of the rolling pass clearly shows that an estimation of the velocity during the whole contour estimation is necessary. The accurately estimated length of the plate (cf. Fig. 2.11a) indicates that the estimated velocity agrees well with its real (average) value. In Fig. 2.13, the results of the contour estimation system for several plates are compared with those of the CMD by means of the lateral deviation  $\delta_{max}$  of the centerline of the plate (cf. Fig. 2.12) and the plate length  $l$ .

The results shown in Fig. 2.13 cover more than 3000 plates which were rolled within two months and which had a minimum length of 20 m. Shorter plates are not considered because camber does not play such an important role for

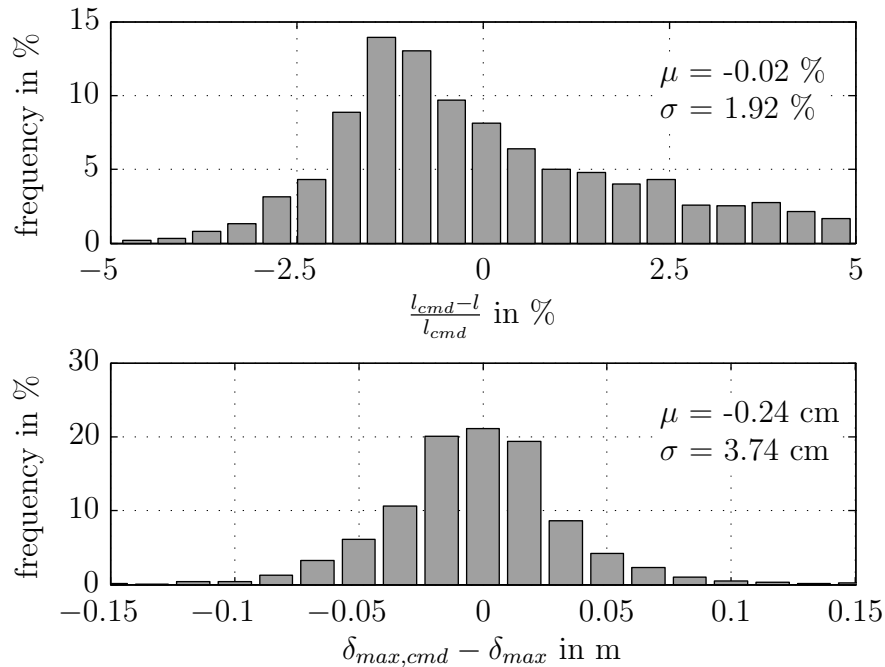


Figure 2.13: Frequency distribution in terms of maximum lateral deviation  $\delta_{max}$  and length of the plate  $l$ .

these plates. The upper part of Fig. 2.13 shows the frequency distribution of the relative error of the estimated length  $l$  of the plates. It indicates a sufficiently accurate estimation. The lower part of Fig. 2.13 shows the frequency distribution of the maximum lateral deviation  $\delta_{max}$ . The histogram agrees well with a normal distribution with over 90 percent of the estimated centerlines featuring an error of less than 5 cm.

## 2.7 Summary

In this chapter, a method for the estimation of the contour and the movement of the plate was discussed. The combination of a 2D-infrared camera as measurement device with optimization-based algorithms yields a robust and very accurate estimation of the plate contour. The contour estimation will be used with the mathematical model of the contour evolution presented in the following chapter to reduce camber by means of different control strategies. Furthermore, the estimated angular movement of the plate will be of interest to effectively reduce contour errors already during the actual rolling pass. Henceforth, the estimation of the plate contour and the movement of the plate are considered to be ideal. This is why the estimated quantities will be referred to as measurements in the following.





## CHAPTER 3

---

### Modeling of the contour evolution

---

The basis for the proposed methods to reduce camber in hot rolling is a suitable mathematical model of the contour evolution. The presented model is tailored to be used in real-time applications, where a precise prediction of the contour evolution and a moderate computational effort are the key prerequisites. The contour after the rolling pass is predicted by the model based on the contour before the rolling pass and the input and output thickness profile of the plate. The output thickness is assumed to be known, e. g., from measurements or from a model of the rolling gap and the mill stand [36]. Large parts of this chapter have been published in [26].

As indicated in Fig. 3.1, a Cartesian coordinate system with coordinates  $x$ ,  $y$  and  $z$  is used. The origin of the coordinate system is fixed to the spatial center of the plate before the rolling pass. In order to simplify the model, the following assumptions are made:

- The plate thickness profile  $h^{in}(x, y)$  in lateral and longitudinal direction is known before each rolling pass.
- The profile of the output thickness  $h^{out}(x, y)$  is also a given quantity.
- After the plate exits the rolling gap, no further plastic deformation occurs.
- Lateral expansion in the rolling gap is not considered.

Knowing the thickness  $h^{in}(x, y)$  of the plate before the rolling pass and the thickness  $h^{out}(x, y)$  at the exit of the rolling gap, the plastic strain in longitudinal direction is

$$\epsilon_{xx}^{pl} = \frac{h^{in}(x, y)}{h^{out}(x, y)} - 1. \quad (3.1)$$

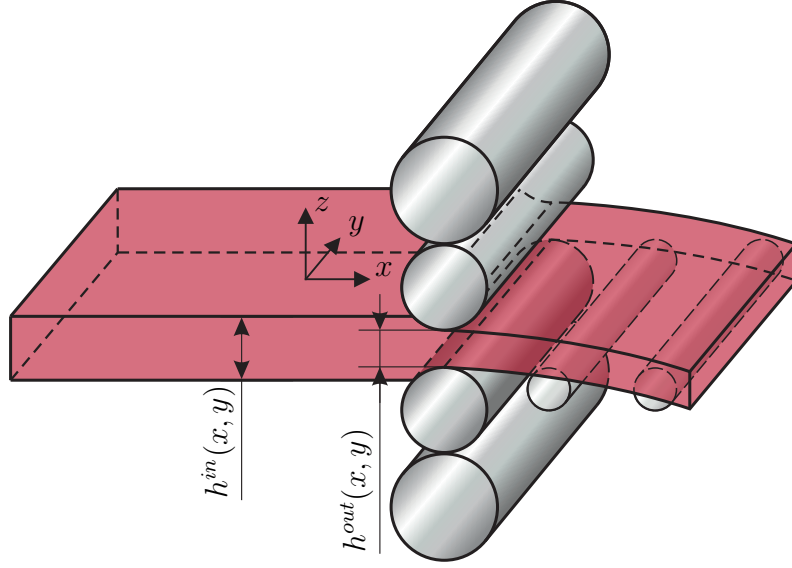


Figure 3.1: Plastic deformation in the rolling gap.

Note that both thickness profiles are defined in the coordinate system fixed to the plate before the rolling pass. The plastic strain  $\epsilon_{xx}^{pl}$  is an input of the following model.

### 3.1 Mathematical model for estimating camber and residual stresses

Before the first rolling pass, the plate has approximately the shape of a rectangular block. Therefore, the computational domain is initially chosen as a cuboid. As long as non-uniformities along the thickness direction of the plate are neglected, a two-dimensional problem formulation may be used. For the given problem, this simplifies the estimation of the strains and residual stresses in the plate. In the following derivation, the assumption of plane stress is made. It is motivated by the absence of surface tractions (outside the rolling gap) and the small dimension in thickness direction compared to the length and the width of the plate (cf. [37]). This implies that stresses along the  $z$ -direction vanish and all quantities are uniform along the  $z$ -direction.

If body forces are absent, the equilibrium equations for an infinitesimal volume element in the two-dimensional space read as

$$\frac{\partial \sigma_{xx}}{\partial x} + \frac{\partial \sigma_{xy}}{\partial y} = 0 \quad (3.2a)$$

$$\frac{\partial \sigma_{xy}}{\partial x} + \frac{\partial \sigma_{yy}}{\partial y} = 0, \quad (3.2b)$$

with the normal stresses  $\sigma_{xx}$  and  $\sigma_{yy}$  along the directions  $x$  and  $y$ , respectively, and the shear stress  $\sigma_{xy}$ . Furthermore, a linear elastic material behavior is assumed, i. e.,

$$\epsilon_{xx}^{el} = \frac{1}{E} (\sigma_{xx} - \nu\sigma_{yy}) \quad (3.3a)$$

$$\epsilon_{yy}^{el} = \frac{1}{E} (\sigma_{yy} - \nu\sigma_{xx}) \quad (3.3b)$$

and

$$\epsilon_{xy}^{el} = \frac{1}{2G} \sigma_{xy} \quad (3.3c)$$

with Young's modulus  $E$ , shear modulus  $G = \frac{E}{2(1+\nu)}$ , and Poisson's ratio  $\nu$ .

These elastic strains have to be added to the plastic strains  $\epsilon_{xx}^{pl}$ ,  $\epsilon_{yy}^{pl}$  and  $\epsilon_{xy}^{pl}$  that are induced during the rolling process. Hence, the total strains read as

$$\epsilon_{\Lambda} = \epsilon_{\Lambda}^{el} + \epsilon_{\Lambda}^{pl}, \quad \Lambda \in \{xx, xy, yy\}. \quad (3.4)$$

The displacement fields  $u = u(x, y)$  and  $v = v(x, y)$  in longitudinal and lateral direction are linked with the strains by

$$\epsilon_{xx} = \frac{\partial u}{\partial x} \quad (3.5a)$$

$$\epsilon_{yy} = \frac{\partial v}{\partial y} \quad (3.5b)$$

and

$$\gamma_{xy} = 2\epsilon_{xy} = \frac{\partial u}{\partial y} + \frac{\partial v}{\partial x}. \quad (3.6)$$

Furthermore, the three unknown strain components are subject to the compatibility equation

$$\frac{\partial^2 \epsilon_{xx}}{\partial y^2} + \frac{\partial^2 \epsilon_{yy}}{\partial x^2} = \frac{\partial^2 \gamma_{xy}}{\partial x \partial y}. \quad (3.7)$$

The latter ensures the existence of continuous, single-valued displacements (cf. [37]). Inserting Hooke's law (3.3) into the relations (3.4) and further into the compatibility equation (3.7) yields

$$\begin{aligned} & \frac{\partial^2}{\partial y^2} \left[ \frac{1}{E} (\sigma_{xx} - \nu\sigma_{yy}) \right] + \frac{\partial^2}{\partial x^2} \left[ \frac{1}{E} (\sigma_{yy} - \nu\sigma_{xx}) \right] - \frac{\partial^2}{\partial x \partial y} \left( \frac{1}{G} \sigma_{xy} \right) \\ &= -\frac{\partial^2 \epsilon_{xx}^{pl}}{\partial y^2} - \frac{\partial^2 \epsilon_{yy}^{pl}}{\partial x^2} + 2 \frac{\partial^2 \epsilon_{xy}^{pl}}{\partial x \partial y}. \end{aligned} \quad (3.8)$$

Summing up the derivatives of (3.2a) and (3.2b) with respect to  $x$  and  $y$ , respectively, gives

$$\frac{\partial^2 \sigma_{xy}}{\partial x \partial y} = -\frac{1}{2} \left( \frac{\partial^2 \sigma_{xx}}{\partial x^2} + \frac{\partial^2 \sigma_{yy}}{\partial y^2} \right).$$

This expression helps to eliminate the shear stress and Poisson's ratio from (3.8) using  $G = \frac{E}{2(1+\nu)}$  and the assumption of a uniform Young's modulus  $E$ . The simplified version of (3.8) thus reads as

$$\frac{\partial^2 \sigma_{xx}}{\partial x^2} + \frac{\partial^2 \sigma_{xx}}{\partial y^2} + \frac{\partial^2 \sigma_{yy}}{\partial x^2} + \frac{\partial^2 \sigma_{yy}}{\partial y^2} = -E \left( \frac{\partial^2 \epsilon_{xx}^{pl}}{\partial y^2} + \frac{\partial^2 \epsilon_{yy}^{pl}}{\partial x^2} - 2 \frac{\partial^2 \epsilon_{xy}^{pl}}{\partial x \partial y} \right). \quad (3.9)$$

As mentioned in [38], (3.9) shows that only plastic deformations with nonvanishing second derivatives induce residual stresses. That is, using a Taylor series expansion, constant and linear terms in the strain tensor would not induce additional elastic deformations. This is because the right-hand side of (3.9) vanishes for such terms resulting in the trivial solution  $\sigma_{xx} = \sigma_{yy} = \sigma_{xy} = 0$  for the considered case of absent surface tractions at the boundary of the plate.

An effective way to deal with the two-dimensional problem (3.9) was introduced in [39]. The so called *Airy's stress function*  $F = F(x, y)$ , which satisfies

$$\sigma_{xx} = \frac{\partial^2 F}{\partial y^2}, \quad \sigma_{yy} = \frac{\partial^2 F}{\partial x^2}, \quad \sigma_{xy} = -\frac{\partial^2 F}{\partial x \partial y}, \quad (3.10)$$

can be inserted into (3.9) to obtain the fourth order inhomogeneous partial differential equation

$$\Delta \Delta F = -E \underbrace{\left( \frac{\partial^2 \epsilon_{xx}^{pl}}{\partial y^2} + \frac{\partial^2 \epsilon_{yy}^{pl}}{\partial x^2} - 2 \frac{\partial^2 \epsilon_{xy}^{pl}}{\partial x \partial y} \right)}_{f(x,y)}, \quad (3.11)$$

with the Laplacian  $\Delta = \frac{\partial^2}{\partial x^2} + \frac{\partial^2}{\partial y^2}$ . Note that the plastic strains  $\epsilon_{\Lambda}^{pl}$ ,  $\Lambda \in \{xx, xy, yy\}$  are given model inputs.  $\epsilon_{xx}^{pl}$  follows from (3.1) whereas  $\epsilon_{xy}^{pl}$  and  $\epsilon_{yy}^{pl}$  are assumed to be zero. Eq. (3.11) is also known as extended biharmonic equation. The term *extended* hints at the inhomogeneous disturbance term on the right-hand side. In the absence of plastic strains, (3.11) is called biharmonic equation. Because of (3.11), the compatibility equation (3.7) is automatically fulfilled if the stresses are calculated according to the chosen ansatz (3.10). Another interesting feature of the (extended) biharmonic equation is its independence of Poisson's ratio  $\nu$ .

Instead of solving the initial partial differential equation for the unknown stresses, strains, and displacements subject to the compatibility equation (3.7), it is equivalent to solve (3.11) for the stress function  $F$ . Once  $F$  is known, the stresses are calculated based on (3.10) and the elastic strains follow from (3.3).

It remains to determine the displacements by integrating the strains (3.4) and (3.5) to

$$u(x, y) = \int_0^x \epsilon_{xx}^{el}(\bar{x}, y) d\bar{x} + \int_0^x \epsilon_{xx}^{pl}(\bar{x}, y) d\bar{x} + \frac{1}{E} \phi(y) \quad (3.12a)$$

and

$$v(x, y) = \int_0^y \epsilon_{yy}^{el}(x, \bar{y}) d\bar{y} + \int_0^y \epsilon_{yy}^{pl}(x, \bar{y}) d\bar{y} + \frac{1}{E} \psi(x), \quad (3.12b)$$

with scalar functions  $\phi(y)$  and  $\psi(x)$ . They define the boundary values of the displacements and cannot be arbitrarily chosen because the strains resulting from inserting (3.12) into (3.5) and (3.6) must fulfill (3.7). Note that (3.12) satisfies the displacement-strain relations (3.5) regardless of the choice of  $\phi(y)$  and  $\psi(x)$ . Combining (3.6), (3.4), and (3.3c) yields

$$\gamma_{xy} = \frac{\partial u}{\partial y} + \frac{\partial v}{\partial x} = 2\epsilon_{xy}^{el} + 2\epsilon_{xy}^{pl} = \frac{2(1+\nu)}{E} \sigma_{xy} + 2\epsilon_{xy}^{pl}$$

and, by inserting (3.12), it follows that

$$\begin{aligned} 2E\epsilon_{xy}^{pl} + 2(1+\nu)\sigma_{xy} &= E \int_0^x \frac{\partial \epsilon_{xx}^{el}(\bar{x}, y)}{\partial y} d\bar{x} + E \int_0^x \frac{\partial \epsilon_{xx}^{pl}(\bar{x}, y)}{\partial y} d\bar{x} + \frac{d\phi(y)}{dy} \\ &\quad + E \int_0^y \frac{\partial \epsilon_{yy}^{el}(x, \bar{y})}{\partial x} d\bar{y} + E \int_0^y \frac{\partial \epsilon_{yy}^{pl}(x, \bar{y})}{\partial x} d\bar{y} + \frac{d\psi(x)}{dx}. \end{aligned}$$

Proceeding with this expression and using (3.3a), (3.3b), and the definition (3.10) yields

$$\begin{aligned} \frac{d\psi(x)}{dx} + \frac{d\phi(y)}{dy} &= 2E\epsilon_{xy}^{pl} - 2(1+\nu) \frac{\partial^2 F}{\partial x \partial y} \\ &\quad - \int_0^x \left( \frac{\partial^3 F(\bar{x}, y)}{\partial y^3} - \nu \frac{\partial^3 F(\bar{x}, y)}{\partial \bar{x}^2 \partial y} \right) d\bar{x} \\ &\quad - \int_0^y \left( \frac{\partial^3 F(x, \bar{y})}{\partial x^3} - \nu \frac{\partial^3 F(x, \bar{y})}{\partial x \partial \bar{y}^2} \right) d\bar{y} \\ &\quad - E \left( \int_0^x \frac{\partial \epsilon_{xx}^{pl}(\bar{x}, y)}{\partial y} d\bar{x} + \int_0^y \frac{\partial \epsilon_{yy}^{pl}(x, \bar{y})}{\partial x} d\bar{y} \right) \\ &= \delta_1(x) + \delta_2(y). \end{aligned} \quad (3.13)$$

The left-hand side of (3.13) splits up into a term  $\delta_1(x) = \frac{d\psi(x)}{dx}$  depending only on  $x$  and a term  $\delta_2(y) = \frac{d\phi(y)}{dy}$  depending only on  $y$ . Integrating these terms gives

$$\psi(x) = \int_0^x \delta_1(\bar{x}) d\bar{x} + C_{\delta_1} \quad (3.14a)$$

and

$$\phi(y) = \int_0^y \delta_2(\bar{y}) d\bar{y} + C_{\delta_2}, \quad (3.14b)$$

with integration constants  $C_{\delta_1}$  and  $C_{\delta_2}$  representing the translational degrees of freedom of a rigid body motion of the plate. Equation (3.13) provides insight into the limitations of choosing the functions  $\psi(x)$  and  $\phi(y)$  such that the compatibility equation (3.7) is fulfilled by (3.12).

## 3.2 Derivation of the boundary conditions

In addition to fulfilling the extended biharmonic equation (3.11), a suitable stress function  $F$  has to satisfy certain boundary conditions. Two different types of boundary conditions can be identified: one giving a restriction on the displacements at the boundary and one constraining the stresses at the boundary. Only the latter one is discussed because the first one (rigid body motion) is not relevant in the considered problem.

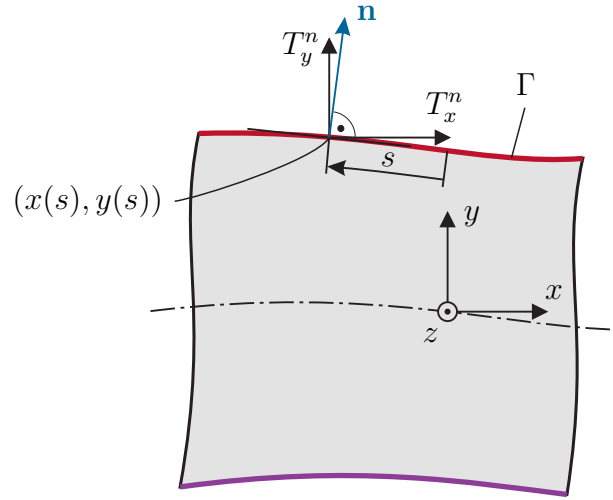


Figure 3.2: Boundary conditions at the plate contour.

The stresses at the boundary  $\Gamma$  of the plate (cf. Fig. 3.2) may be expressed by the components of the external stress vector, i. e.,  $T_x^n = T_x^n(s)$  in longitudinal and  $T_y^n = T_y^n(s)$  in lateral direction. They depend on the curvilinear coordinate  $s$  measured in the counter-clockwise direction and they are defined by

$$T_x^n = \sigma_{xx}n_x + \sigma_{xy}n_y \quad (3.15a)$$

and

$$T_y^n = \sigma_{xy}n_x + \sigma_{yy}n_y. \quad (3.15b)$$

Here,  $n_x$  and  $n_y$  denote the components of the unit normal vector

$$\mathbf{n} = \begin{bmatrix} n_x \\ n_y \end{bmatrix} = \begin{bmatrix} \frac{dy}{ds} \\ -\frac{dx}{ds} \end{bmatrix} \quad (3.16)$$

of the boundary  $\Gamma$ . The vector  $\mathbf{n}$  points outwards. A specific point on the boundary  $\Gamma$  is defined by its Cartesian coordinates  $(x(s), y(s))$ . Insertion of (3.10) and (3.16) into (3.15) yields

$$T_x^n = \frac{\partial^2 F}{\partial y^2} \frac{dy}{ds} + \frac{\partial^2 F}{\partial x \partial y} \frac{dx}{ds} \quad (3.17a)$$

and

$$T_y^n = -\frac{\partial^2 F}{\partial x \partial y} \frac{dy}{ds} - \frac{\partial^2 F}{\partial x^2} \frac{dx}{ds}. \quad (3.17b)$$

In the considered problem, surface tractions are absent, i. e. the boundary conditions are

$$T_x^n = T_y^n = 0. \quad (3.17c)$$

### 3.3 Solution of the biharmonic equation

Searching for an exact solution of (3.11) and the boundary conditions (3.17) is difficult. Only for trivial shapes, specific plastic deformations and particular boundary conditions, exact solutions may be obtained. To circumvent this difficulty, an approximate solution with a stress function that automatically satisfies (3.11) but not necessarily (3.17) is used.

The solution  $F_{hom}$  of the homogeneous biharmonic equation

$$\Delta \Delta F_{hom} = 0 \quad (3.18)$$

and the particular solution  $F_{part}$  of the extended biharmonic equation (3.11) are added to obtain the solution

$$F = F_{hom} + F_{part}. \quad (3.19)$$

This superposition approach is possible due to the linearity of (3.11).  $F_{part}$  fulfills (3.11) but not necessarily (3.17). Therefore,  $F_{hom}$ , which is independent of the plastic deformation (cf. (3.18)), is chosen so that  $F$  satisfies (3.17). In this work, power series are used for  $F$  to solve the extended biharmonic equation.

### 3.3.1 Power series solution

A method originally proposed in [40] is applied to obtain the power series solution. A single homogeneous solution term  $\Psi_i$  with degree  $p$  is characterized by

$$\Psi_i = \sum_{j=0}^p \sum_{q=0}^p b_{j,q} x^j y^q \quad (3.20)$$

with constant coefficients  $b_{j,q}$ . They are chosen so that the homogeneous biharmonic equation (3.18) is individually satisfied by each term  $\Psi_i$ . By insertion of  $\Psi_i$  into (3.18), a system of linear equations for determining the unknown coefficients  $b_{j,q}$  is obtained.  $F_{hom}$  is a linear combination of the terms  $\Psi_i$ , i. e.,

$$F_{hom} = \sum_{i=1}^n a_i \Psi_i = \mathbf{J}^T \mathbf{a} \quad (3.21)$$

with  $\mathbf{a} = [a_i]_{i=1,\dots,n}$  and  $\mathbf{J} = [\Psi_i]_{i=1,\dots,n}$  for some constants  $a_i$ ,  $i = 1, \dots, n$ . The coefficients  $a_i$  will be chosen to satisfy the boundary conditions (3.17). In an analogous manner, a series solution of the extended biharmonic equation (3.11) can be found if the given plastic strains are approximated by a two-dimensional power series

$$\epsilon_{\Lambda}^{pl} = \sum_{i=0}^{P_x} \sum_{q=0}^{P_y} \underbrace{c_{\Lambda,i,q} x^i y^q}_{\Phi_{\Lambda,i,q}}, \quad \Lambda \in \{xx, xy, yy\} \quad (3.22)$$

with constant coefficients  $c_{\Lambda,i,q}$ ,  $i = 0, \dots, P_x$  and  $q = 0, \dots, P_y$  and the degrees  $P_x$  and  $P_y$  in the longitudinal and lateral direction, respectively. Each individual solution term  $F_{part,i,q}$  of the particular solution

$$F_{part} = \sum_{i=0}^{P_x} \sum_{q=0}^{P_y} F_{part,i,q}$$

must satisfy the corresponding part of (3.11), i. e.,

$$\Delta \Delta F_{part,i,q} = -E \underbrace{\left( \frac{\partial^2 \Phi_{xx,i,q}}{\partial y^2} + \frac{\partial^2 \Phi_{yy,i,q}}{\partial x^2} - 2 \frac{\partial^2 \Phi_{xy,i,q}}{\partial x \partial y} \right)}_{f_{i,q}(x,y)} \quad (3.23)$$

with  $\Phi_{\Lambda,i,q}$  according to (3.22). Similarly to (3.20),  $F_{part,i,q}$  is formulated as a two-dimensional polynomial

$$F_{part,i,q}(x, y) = \sum_{i=0}^{\check{P}_x} \sum_{q=0}^{\check{P}_y} \check{b}_{i,q} x^i y^q$$



with the degrees  $\check{P}_x$  and  $\check{P}_y$  selected properly depending on the degree of  $f_{i,q}(x, y)$ . The polynomial coefficients  $\check{b}_{i,q}$  are found from a comparison of coefficients in (3.23).

As mentioned earlier, a solution that satisfies the boundary conditions in an approximate manner is derived. Inserting an approximate ansatz  $\hat{F}$  for Airy's stress function into the boundary conditions (3.17) gives the residuals

$$\begin{aligned}\mathcal{R}_x(\hat{F}) &= \frac{\partial^2 \hat{F}}{\partial y^2} \frac{dy}{ds} + \frac{\partial^2 \hat{F}}{\partial x \partial y} \frac{dx}{ds} \\ \mathcal{R}_y(\hat{F}) &= -\frac{\partial^2 \hat{F}}{\partial x \partial y} \frac{dy}{ds} - \frac{\partial^2 \hat{F}}{\partial x^2} \frac{dx}{ds}.\end{aligned}$$

The idea is that these residuals vanish in a weighted integral sense, i. e.,

$$\int_{\Gamma} v_x \mathcal{R}_x(\hat{F}) ds + \int_{\Gamma} v_y \mathcal{R}_y(\hat{F}) ds = 0, \quad (3.24)$$

with the weighting functions  $v_x$  and  $v_y$ . Two different weighting functions are necessary to avoid that only the sum  $\mathcal{R}_x(\hat{F}) + \mathcal{R}_y(\hat{F})$  vanishes. With  $\hat{F} = \hat{F}_{hom} + \hat{F}_{part}$  and  $\hat{F}_{hom} = \hat{\mathbf{J}}^T \mathbf{a}$  according to (3.19) and (3.21), respectively, the residual terms can be written as

$$\mathcal{R}_x(\hat{F}) = \left( \frac{\partial^2 \hat{\mathbf{J}}^T}{\partial y^2} \frac{dy}{ds} + \frac{\partial^2 \hat{\mathbf{J}}^T}{\partial x \partial y} \frac{dx}{ds} \right) \mathbf{a} + \frac{\partial^2 \hat{F}_{part}}{\partial y^2} \frac{dy}{ds} + \frac{\partial^2 \hat{F}_{part}}{\partial x \partial y} \frac{dx}{ds}$$

and

$$\mathcal{R}_y(\hat{F}) = \left( -\frac{\partial^2 \hat{\mathbf{J}}^T}{\partial x \partial y} \frac{dy}{ds} - \frac{\partial^2 \hat{\mathbf{J}}^T}{\partial x^2} \frac{dx}{ds} \right) \mathbf{a} - \frac{\partial^2 \hat{F}_{part}}{\partial x \partial y} \frac{dy}{ds} - \frac{\partial^2 \hat{F}_{part}}{\partial x^2} \frac{dx}{ds}.$$

Now a slightly modified least-squares method as reported in [41] is employed. The method suggests using the residuals  $\mathcal{R}_x(\Psi_i)$  and  $\mathcal{R}_y(\Psi_i)$  as weighting functions  $v_x$  and  $v_y$ , respectively. Other weighting functions are also possible for the given problem but  $\mathcal{R}_x(\Psi_i)$  and  $\mathcal{R}_y(\Psi_i)$  simplify the evaluation of the integrals in (3.24). Equation (3.24) must vanish individually for each pair of weighting functions  $v_x = \mathcal{R}_x(\Psi_i)$  and  $v_y = \mathcal{R}_y(\Psi_i)$ . This results in a system of linear equations

$$(\mathbf{A}_x + \mathbf{A}_y) \mathbf{a} = \mathbf{y}_x + \mathbf{y}_y \quad (3.25)$$

with the matrices

$$\mathbf{A}_x = \int_{\Gamma} \mathcal{R}_x(\hat{\mathbf{J}}) \mathcal{R}_x(\hat{\mathbf{J}}^T) ds \quad (3.26a)$$

$$\mathbf{A}_y = \int_{\Gamma} \mathcal{R}_y(\hat{\mathbf{J}}) \mathcal{R}_y(\hat{\mathbf{J}}^T) ds \quad (3.26b)$$

and the vectors

$$\mathbf{y}_x = - \int_{\Gamma} \mathcal{R}_x(\hat{\mathbf{J}}) \mathcal{R}_x(\hat{F}_{part}) ds \quad (3.27a)$$

$$\mathbf{y}_y = - \int_{\Gamma} \mathcal{R}_y(\hat{\mathbf{J}}) \mathcal{R}_y(\hat{F}_{part}) ds. \quad (3.27b)$$

The residual of a vector is just an assembly of the residuals of its components. The proposed method generates symmetric matrices  $\mathbf{A}_x$  and  $\mathbf{A}_y$ , which can be utilized when solving (3.25) for the unknown coefficients  $a_i$ . The numerical properties of  $\mathbf{A}_x$  and  $\mathbf{A}_y$  are of good nature, even for polynomial approximations with high degrees. For simplicity reasons, henceforth the approximate solution  $\hat{F}$  is no longer denoted with a hat.

### 3.3.2 Parameterization of the plate contour

There exist various methods to deal with curvilinear boundary domains of differential equations. In some cases, a change of the chosen coordinate system leads to a formally simpler representation of the boundary. Polar coordinates, for instance, should be used for circular computational domains.

However, the problem considered in this work requires a tailored definition of the boundary, which also allows to track the camber during several rolling passes. A closed-form parametric representation of the boundary seems favorable in terms of integration along the edges. As indicated in Fig. 3.3, a convenient formulation consists of four polynomials representing the four boundaries. A point on the

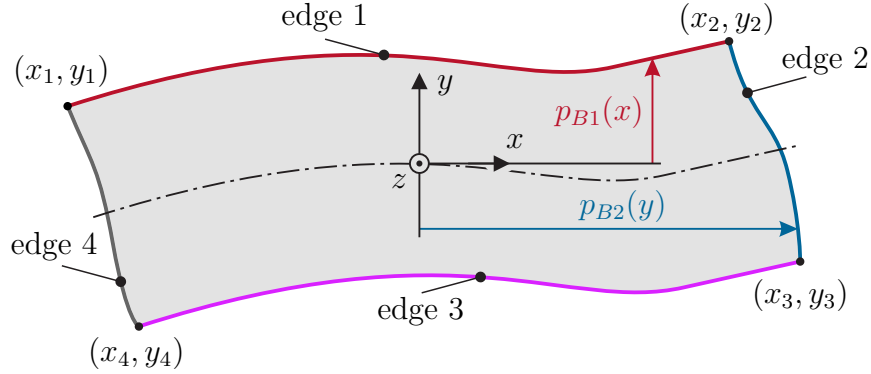


Figure 3.3: Definition of the edges of a plate with a curvilinear boundary.

edges 1 and 3 (longitudinal edges) is parameterized by a polynomial with degree  $N_B$  as

$$p_{Bj}(x) = \sum_{i=0}^{N_B} d_{j,i} x^i, \quad j = 1, 3$$

and on the edges 2 and 4 (head and tail) as

$$p_{Bj}(y) = \sum_{i=0}^{N_B} d_{j,i} y^i, \quad j = 2, 4.$$

Hence, the curvilinear boundary  $\Gamma$  is described by

$$\begin{aligned} \Gamma = & \left\{ (x, y) \mid x \in [x_1, x_2], y = p_{B1}(x) \right\} \cup \left\{ (x, y) \mid y \in [y_3, y_2], x = p_{B2}(y) \right\} \\ & \cup \left\{ (x, y) \mid x \in [x_4, x_3], y = p_{B3}(x) \right\} \cup \left\{ (x, y) \mid y \in [y_4, y_1], x = p_{B4}(y) \right\}. \end{aligned}$$

Due to the integration along a curved boundary  $\Gamma$ , e. g., in (3.24), it seems reasonable to introduce a curvilinear coordinate  $s$  defined by

$$ds = \sqrt{1 + \left( \frac{dp_{Bj}(x)}{dx} \right)^2} dx$$

for  $j \in \{1, 3\}$  and

$$ds = \sqrt{1 + \left( \frac{dp_{Bj}(y)}{dy} \right)^2} dy$$

for  $j \in \{2, 4\}$ .

A curved shape  $\Gamma$  generally precludes an analytical integration of (3.24). Therefore, the integrals are numerically evaluated by Gaussian quadrature. An integral is thus approximated by a weighted sum

$$\int_{-1}^1 f(\xi) d\xi \approx \sum_{i=1}^{N_q} w_i f(\xi_i), \quad (3.28)$$

where  $N_q$  denotes the quadrature order and  $w_i$  represents the weight for the function value  $f(\xi_i)$  at the sampling point  $\xi_i$ . Krylov (cf. [42]) showed that the sampling points of one possible quadrature method can be found as the roots of the Legendre polynomial

$$p_{N_q}(x) = \frac{1}{2^{N_q} N_q!} \frac{d^{N_q}}{dx^{N_q}} \left[ (x^2 - 1)^{N_q} \right]$$

and that the corresponding weights are defined by

$$w_i = \int_{-1}^1 \prod_{\substack{q=0 \\ q \neq i}}^{N_q} \frac{x - x_q}{x_i - x_q} dx.$$

Additionally, a transformation

$$\int_{x_{lo}}^{x_{up}} f(x)dx = \frac{x_{up} - x_{lo}}{2} \int_{-1}^1 f(\xi)d\xi$$

with

$$x = \frac{x_{up} + x_{lo}}{2} + \frac{x_{up} - x_{lo}}{2}\xi$$

and properly chosen integration boundaries  $x_{lo}$  and  $x_{up}$  (cf. Fig. 3.3) has to be performed. This transformation maps the different integration boundaries in (3.26) and (3.27) to the interval  $[-1, 1]$  used in (3.28). The weights  $w_i$  and the sampling points  $\xi_i$  are only calculated once and stored, so that their numerical values can be used in the evaluation of the integrals.

### 3.3.3 Simulation results

In the following, simulation results demonstrate the feasibility of the proposed contour evolution model. As inputs of the computations, input and output thickness profiles based on thickness measurements are used. The thickness profiles are assumed to be constant and quadratic in longitudinal and lateral direction, respectively. A quadratic polynomial is used in the lateral direction because the thickness measurement device installed at the considered rolling mill measures the thickness of the plate only at three different positions along the direction  $y$ . Hence, only a polynomial with degree less or equal than two can be fitted uniquely in the width direction of the plate. The plastic deformations  $\epsilon_{yy}^{pl}$  and  $\epsilon_{xy}^{pl}$  are assumed to vanish. Moreover, the temperature profile is assumed to be constant and a rectangle with the dimensions  $l = 29.4$  m and  $w = 2.7$  m is used as initial shape of the plate (before the first rolling pass). The results obtained by

Parameter	Value	Unit
$E$	140	kN/mm <sup>2</sup>
$\nu$	0.3	
$n$	70	
$P_x$	8	
$P_y$	8	
$N_B$	4	
$N_q$	20	

Table 3.1: Parameters used for the computations.

the power series solution method using the parameters from Tab. 3.1 are shown in Fig. 3.4. For both passes, Fig. 3.4 shows the input and output thickness profile of the plate and the resulting plastic deformation  $\epsilon_{xx}^{pl}$ , approximated by polynomials

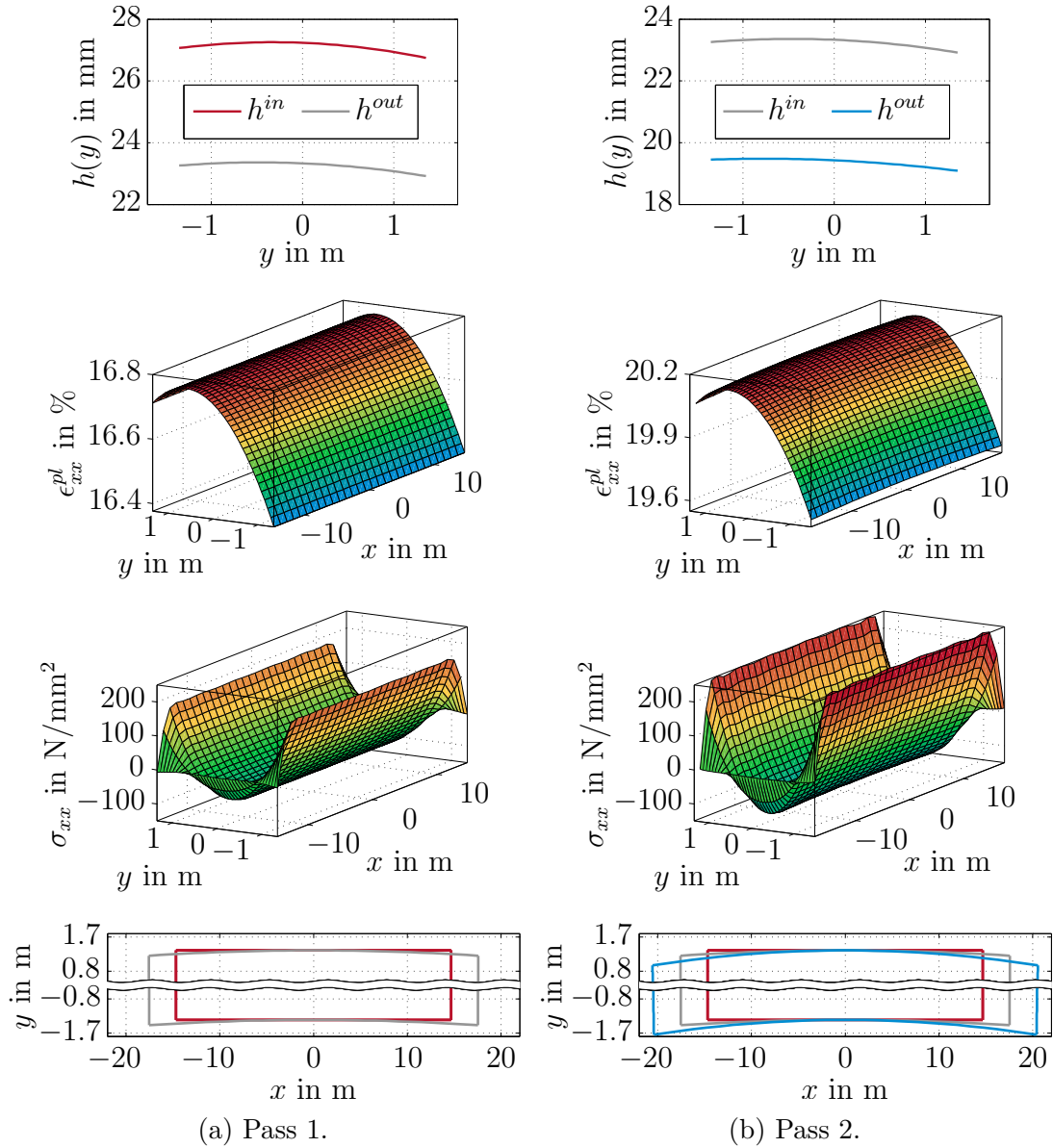


Figure 3.4: Simulation results for 2 consecutive passes utilizing the power series solution scheme.

of degree  $P_x = P_y = 8$ . Due to the uniform thickness profile along the plate length  $l$ , the plastic deformation  $\epsilon_{xx}^{pl}$  is also uniform along the longitudinal direction  $x$ .

Furthermore, the residual normal stress  $\sigma_{xx}$  in longitudinal direction and the resulting plate shape after the pass are shown. Fig. 3.4 indicates the approximate satisfaction of the stress boundary conditions at the head and the tail end of the plate. The slight violation of the boundary conditions can be further reduced by increasing the order of the ansatz function for Airy's stress function  $F$ . As seen in the lower part of Fig. 3.4, the contour of the plate shows a considerable

camber after the second pass. This contour error is caused by the change of the asymmetry of the plate thickness which is too small to see in Fig. 3.4. The asymmetry is characterized by the absolute asymmetry  $\Delta h(x)$  in the form

$$\Delta h(x) = h(x, w/2) - h(x, -w/2).$$

For the given simulation scenario,  $\Delta h_i(x)$  in the  $i$ -th pass is independent of the longitudinal coordinate  $x$  and has the values  $\Delta h_1^{in} = -319 \mu\text{m}$ ,  $\Delta h_1^{out} = \Delta h_2^{in} = -340 \mu\text{m}$ , and  $\Delta h_2^{out} = -361 \mu\text{m}$ .

For the considered plate, these absolute asymmetries result in a maximum lateral deviation of 0.4 m. That is, the sensitivity of the contour evolution with respect to the thickness asymmetry is high, especially for long and thin plates. This simulation illustrates that the reduction of contour errors is a delicate task because even small deviations from the desired thickness profile may lead to large contour errors.

### 3.4 Effect of non-uniform elastic properties

In the previous sections, a homogeneous elastic behavior was assumed. However, in many real heavy-plate rolling scenarios, temperature gradients in the plate may be a consequence of inhomogeneous heating in the slab reheating furnace. As a consequence of its temperature dependency, Young's modulus is thus also non-uniform. Assuming a homogeneous temperature distribution along the thickness of the plate, the inverse of Young's modulus  $E(x, y)$  may be approximated by a Taylor series, i. e.,

$$p_E(x, y) = \frac{1}{E(x, y)} = \sum_{i=0}^{P_E} \sum_{q=0}^{P_E} c_{E,i,q} x^i y^q \quad (3.29)$$

with the polynomial degree  $P_E$  and the coefficients  $c_{E,i,q}$ . The coefficients of the polynomial (3.29) are determined utilizing the least-squares method. Insertion of (3.29) into (3.8) leads to

$$\begin{aligned} & \frac{\partial^2}{\partial y^2} \left[ p_E(x, y) (\sigma_{xx} - \nu \sigma_{yy}) \right] + \frac{\partial^2}{\partial x^2} \left[ p_E(x, y) (\sigma_{yy} - \nu \sigma_{xx}) \right] \\ & - \frac{\partial^2}{\partial x \partial y} \left[ 2(1 + \nu) p_E(x, y) \sigma_{xy} \right] \\ & = - \left( \frac{\partial^2 \epsilon_{xx}^{pl}}{\partial y^2} + \frac{\partial^2 \epsilon_{yy}^{pl}}{\partial x^2} - 2 \frac{\partial^2 \epsilon_{xy}^{pl}}{\partial x \partial y} \right) \end{aligned}$$

With the reasonable assumption  $\nu = \text{const.}$  (cf. [43]), the extended biharmonic equation then reads as

$$\begin{aligned}
& \left[ \frac{\partial^2 p_E(x, y)}{\partial x^2} \left( \frac{\partial^2}{\partial x^2} - \nu \frac{\partial^2}{\partial y^2} \right) + \frac{\partial^2 p_E(x, y)}{\partial y^2} \left( \frac{\partial^2}{\partial y^2} - \nu \frac{\partial^2}{\partial x^2} \right) \right. \\
& + 2(1 + \nu) \frac{\partial^2 p_E(x, y)}{\partial x \partial y} \frac{\partial^2}{\partial x \partial y} + 2 \frac{\partial p_E(x, y)}{\partial x} \left( \frac{\partial^3}{\partial x^3} + \frac{\partial^3}{\partial x \partial y^2} \right) \\
& + 2 \frac{\partial p_E(x, y)}{\partial y} \left( \frac{\partial^3}{\partial y^3} + \frac{\partial^3}{\partial x^2 \partial y} \right) \\
& \left. + p_E(x, y) \left( \frac{\partial^4}{\partial x^4} + 2 \frac{\partial^4}{\partial x^2 \partial y^2} + \frac{\partial^4}{\partial y^4} \right) \right] F(x, y) \\
& + \underbrace{\left( \frac{\partial^2 \epsilon_{xx}^{pl}}{\partial y^2} + \frac{\partial^2 \epsilon_{yy}^{pl}}{\partial x^2} - 2 \frac{\partial^2 \epsilon_{xy}^{pl}}{\partial x \partial y} \right)}_{\check{f}} \\
& = \mathcal{D}(F(x, y)) = 0. \tag{3.30}
\end{aligned}$$

The inhomogeneous Young's modulus causes some additional terms in the extended biharmonic equation compared to (3.11) for uniform  $E$ . However, linearity of the equation is preserved. Simple adaption of the proposed solution scheme fails for this case because it is rather difficult to find exact solutions for (3.30).

Therefore, exact satisfaction of the extended biharmonic equation is abandoned and the equation is only satisfied in an integral sense over the considered domain  $I$ . For this purpose, the boundary condition (3.24) is extended by a weighted residual of the extended biharmonic equation (3.30). This gives

$$\iint_I \mathcal{D}(F(x, y)) v_D dx dy + \int_{\Gamma} \mathcal{R}_x(F(x, y)) v_x ds + \int_{\Gamma} \mathcal{R}_y(F(x, y)) v_y ds = 0$$

with the additional weighting function  $v_D$ .

The stress function  $F(x, y)$  is chosen as

$$F(x, y) = \sum_{i=0}^{\check{P}_x} \sum_{q=0}^{\check{P}_y} \check{a}_{i,q} x^i y^q = \check{\mathbf{J}}^T \check{\mathbf{a}} \tag{3.31}$$

with the degrees  $\check{P}_x$  and  $\check{P}_y$  in the lateral and longitudinal direction, respectively. Note that the coefficients  $\check{a}_{0,0}$ ,  $\check{a}_{1,0}$  and  $\check{a}_{0,1}$  are set to zero because they neither contribute to the boundary condition (3.17) nor to the extended biharmonic equation (3.30).

Equation (3.31) does not automatically satisfy the extended biharmonic equation (3.30) and therefore the coefficients  $\check{a}_{i,q}$  are used to approximately fulfill (3.30) and the boundary condition (3.24). Therefore, it is no longer distinguished

between a homogeneous and a particular solution. Even the number of solution terms in (3.31) should be raised compared to the homogeneous case to achieve a sufficient fulfillment of (3.30).

By analogy to the case with uniform  $E$  (see (3.25)), the weighted residual ansatz results in a system of linear equations

$$\left(\check{\mathbf{A}}_x + \check{\mathbf{A}}_y + \check{\mathbf{A}}_{ext}\right) \check{\mathbf{a}} = \check{\mathbf{y}} \quad (3.32)$$

with the coefficient matrices

$$\begin{aligned} \check{\mathbf{A}}_x &= \int_{\Gamma} \mathcal{R}_x(\check{\mathbf{J}}) \mathcal{R}_x(\check{\mathbf{J}}^T) ds \\ \check{\mathbf{A}}_y &= \int_{\Gamma} \mathcal{R}_y(\check{\mathbf{J}}) \mathcal{R}_y(\check{\mathbf{J}}^T) ds \\ \check{\mathbf{A}}_{ext} &= \iint_I \mathcal{D}(\check{\mathbf{J}})\Big|_{\check{f}=0} \mathcal{D}(\check{\mathbf{J}}^T)\Big|_{\check{f}=0} dx dy \end{aligned} \quad (3.33)$$

and the vector

$$\check{\mathbf{y}} = - \iint_I \mathcal{D}(\check{\mathbf{J}})\Big|_{\check{f}=0} \check{f} dx dy. \quad (3.34)$$

Again the coefficient matrix from (3.32) is symmetric.

In addition to the integration along the boundary  $\Gamma$  of the plate, a two-dimensional integral over the plate surface has to be evaluated in (3.33) and (3.34). The evaluation of these double integrals must be handled separately. This is caused by the curvilinear boundaries of the plate, where the integration order cannot be selected arbitrarily. Depending on the actual shape of the plate, the integration domain  $I$  has to be divided into several subdomains. Fig. 3.5 shows an

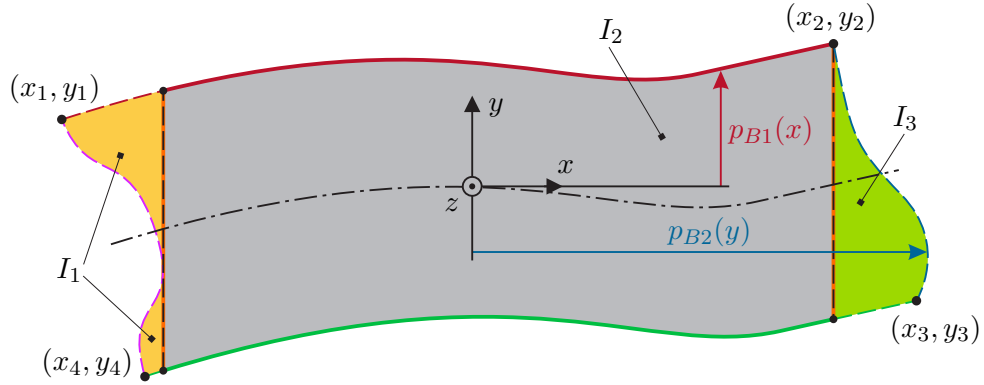


Figure 3.5: Integration area split up into three subdomains.

exemplary plate contour parameterized by polynomials where three subdomains are necessary. For the inner subdomain  $I_2$  of the shown plate, the integration is first performed along the  $y$ -direction and then along the  $x$ -direction. For the



remaining subdomains  $I_1$  and  $I_3$  the integration order has to be changed. Because the boundaries of the subdomains  $I_1$  and  $I_3$  can be uniquely defined as a function of the coordinate  $y$ , no additional subdomains are necessary.

In the following, the influence of an inhomogeneous Young's modulus will be studied to determine its relevance for the formation of camber defects. First, Young's modulus  $E(x, y)$  is calculated from a given temperature distribution  $T(x, y)$  by

$$E(x, y) = f_T(T(x, y))$$

with an appropriate function  $f_T(T)$ . As proposed in [43],  $f_T(T)$  may be approximated as an affine function

$$E(x, y) = E_0 + E_1 (T(x, y) - T_0),$$

with the parameters  $E_0 = 200 \text{ kN/mm}^2$ ,  $E_1 = -83 \text{ N/(mm}^2 \text{ }^\circ\text{C)}$ , and  $T_0 = 20 \text{ }^\circ\text{C}$ .

The impact of two different temperature distributions on the plate contour and the residual stresses are analyzed utilizing the rolling process from Section 3.3.3. Here, the polynomial degree  $P_E = 3$  and  $n = 102$  coefficients  $\check{a}_{i,q}$  are used for the calculations, which is equivalent to a polynomial degree  $\check{P}_x = \check{P}_y = 13$  of the stress function  $F$ . In both cases, only the first pass and a time-independent linear temperature distribution are considered. The first temperature distribution is linear in longitudinal direction of the plate as indicated in Fig. 3.6. The resulting Young's modulus is therefore also affine in longitudinal direction (cf. Fig. 3.6), which leads to a decreasing stress distribution  $\sigma_{xx}$ . A temperature non-uniformity of  $200 \text{ }^\circ\text{C}$  occurs seldom in the real rolling process. Hence, the considered scenario provides a conservative estimation of the significance of non-uniform elastic properties.

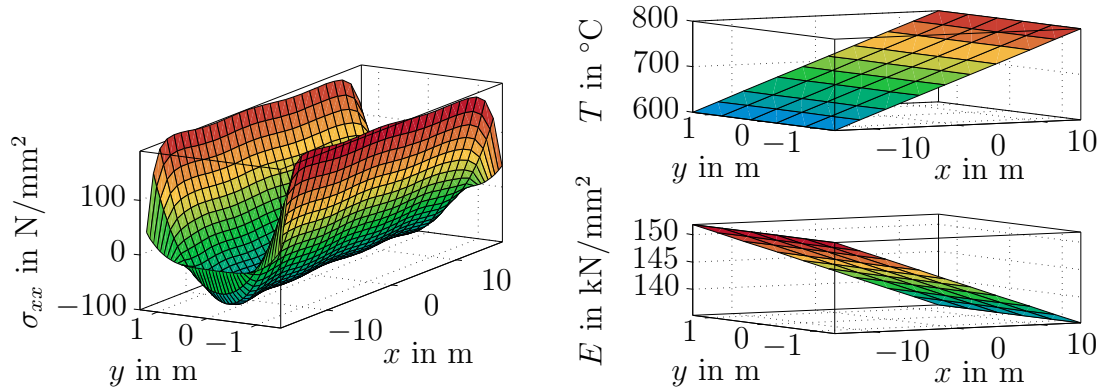


Figure 3.6: Normal stress distribution  $\sigma_{xx}$  for temperature gradient in longitudinal direction.

For the second case, the temperature is non-uniform along the lateral direction (cf. Fig. 3.8). Compared to the results for a plate with constant temperature

shown in Fig. 3.7, the differences are almost negligible. The same conclusion can be drawn from the maximum lateral deviation of the centerline of the plate (cf. Fig. 2.12). The inhomogeneous Young's modulus does not change the maximum lateral deviation by more than 0.7 mm.

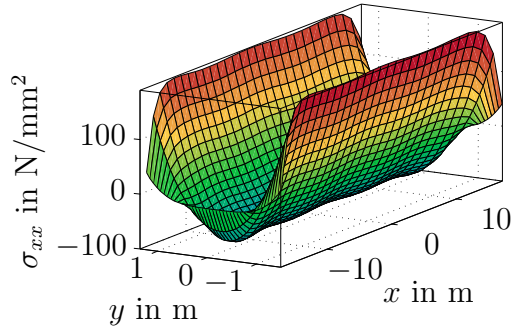


Figure 3.7: Normal stress distribution  $\sigma_{xx}$  for constant plate temperature  $T = 700^\circ\text{C}$ .

This result shows that an inhomogeneous temperature distribution has only little influence on the occurring camber caused by changes of the Young's modulus. This is why the influence of the temperature on the Young's modulus is neglected in all subsequent simulations and in the model-based control concepts to reduce the camber. However, the temperature distribution has a significant influence on the deformation resistance (yield stress) and thus on the resulting rolling gap profile. Note that the yield stress does not appear as a parameter in the proposed model.

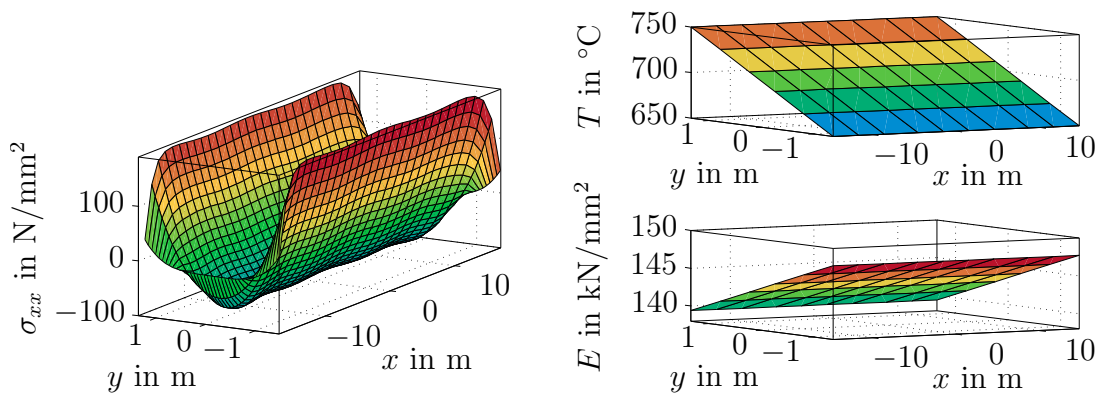


Figure 3.8: Normal stress distribution  $\sigma_{xx}$  for temperature gradient in lateral direction.

### 3.5 Effect of thermal expansion

The thermal expansion of the plate is another effect, which depends on the temperature distribution of the plate. In the simulation results from Section 3.4, the temperature was assumed to be constant over time and therefore no thermal strain  $\epsilon^{therm}$  occurred. However, the change of the temperature from  $T_0$  to  $T_1$  assuming an isotropic thermal material behavior induces the thermal strain

$$\epsilon_{\Lambda}^{therm} = \alpha (T_1(x, y) - T_0(x, y)), \quad \Lambda \in \{xx, yy\}$$

with the thermal expansion coefficient  $\alpha$ . No shear deformation is induced due to thermal expansion, i. e.,  $\epsilon_{xy}^{therm} = 0$ . As shown in [38], the thermal strains  $\epsilon_{\Lambda}^{therm}$  can be considered in the extended biharmonic equation in the form

$$\Delta\Delta F = -E \left( \frac{\partial^2 (\epsilon_{xx}^{pl} + \epsilon_{xx}^{therm})}{\partial y^2} + \frac{\partial^2 (\epsilon_{yy}^{pl} + \epsilon_{yy}^{therm})}{\partial x^2} - 2 \frac{\partial^2 \epsilon_{xy}^{pl}}{\partial x \partial y} \right). \quad (3.35)$$

The effect of thermal expansion can only be described with (3.35) as long as the thermal strains do not induce further plastic deformations in the plate. Because of the similarity of (3.35) with (3.23), (3.35) can be solved with the method presented in Section 3.3. I.e., the sum of the plastic and thermal strains are approximated by two-dimensional polynomials (cf. (3.22)), the resulting polynomial coefficients  $c_{\Lambda, i, q}$  are used to calculate the coefficients of the homogeneous solution of the biharmonic equation and further the displacements of the plate.

In the following, the effect of the thermal expansion on the rolling process from Section 3.4 is studied. For simplicity reasons, a constant thermal expansion coefficient  $\alpha = 12 \cdot 10^{-6} \text{ 1/K}$  is assumed for the simulations.

First, the temperature distribution shown in Fig. 3.6 is used as initial temperature  $T_0$ . It is assumed that the plate temperature becomes homogeneous and settles at  $T_1 = 700 \text{ }^\circ\text{C}$ . The vanishing longitudinal temperature gradient considered in this simulation scenario does not change the plate contour significantly.

In the second simulation scenario, a temperature distribution with a lateral gradient as shown in Fig. 3.8 is used as initial temperature  $T_0$  and the final temperature is chosen as  $T_1 = 700 \text{ }^\circ\text{C}$ . This change of the temperature in the lateral direction results in a reduction of the maximum lateral deviation of approximately 50 mm. A temperature non-uniformity of  $100 \text{ }^\circ\text{C}$  in the lateral direction occurs quite seldom in the real rolling process. Hence, the considered case constitutes a worst-case scenario of thermal expansion. Therefore, the influence of thermal expansion will be neglected in all subsequent considerations.

### 3.6 Validation

In this section, simulation results of the contour evolution model are compared to measurement results for a typical plate rolled at AG der Dillinger Hüttenwerke,

Germany. The considered plate is rolled out from an initial plate thickness

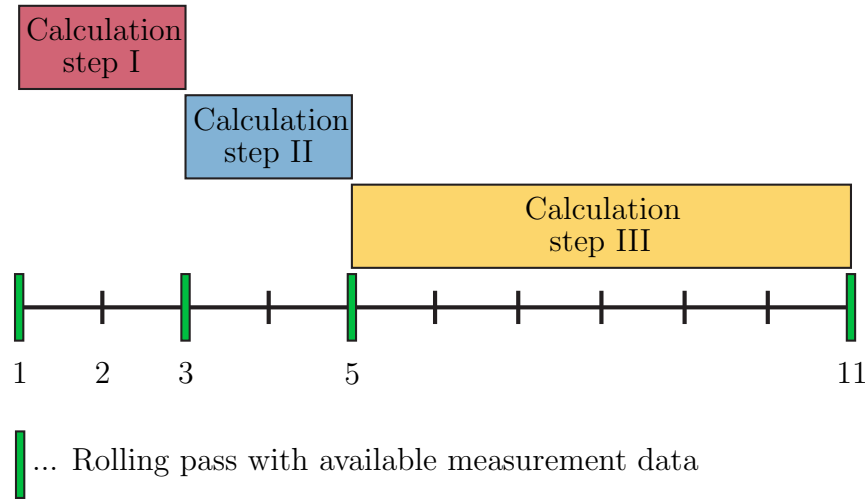


Figure 3.9: Explanation of the three calculation steps.

of 87 mm to its final thickness 36.5 mm using 11 rolling passes. As inputs of the computations, the input thickness and the output thickness of the plate are used. These thickness profiles are obtained from measurements. Moreover, the temperature is assumed to be uniform and the parameters used for the computations are listed in Tab. 3.1.

Measurement data is only available before and after the rolling passes 1, 3, 5 and 11. Therefore, the calculation is done in three steps, each covering at least two rolling passes, as indicated in Fig. 3.9. The simulation only uses the contour measurement from pass 1 as initial contour before calculation step I. The remaining measurements of the contour are only used for validation.

For the three calculation steps, Fig. 3.10a shows the plastic strains  $\epsilon_{xx}^{pl}$  approximated by polynomials of degree  $P_x = P_y = 8$ . The real plate contour is measured by means of a laser line scanner and some image processing algorithms. The scanner is arranged across the roller table. It captures images (1D arrays) as the plate moves along the roller table. Its images are joined by software to generate a full 2D picture of the plate contour. Due to the purely translational motion of the plate this is a consecutive arrangement of 1D arrays. This strategy gives a relatively low image resolution along the direction  $x$ , which does not allow an accurate measurement of the edges 2 and 4 (head and tail end of the plate). Consequently, only the edges 1 and 3 are shown and analyzed in the following. Fig. 3.10b shows the simulated and measured plate contours after all three calculation steps. Despite the fact that the calculation covers 10 rolling passes, the model mismatch is in an acceptable range. More accurate results would be achieved if the model were fed with measurement data not only at the beginning but after each rolling pass where measurements are available. With the

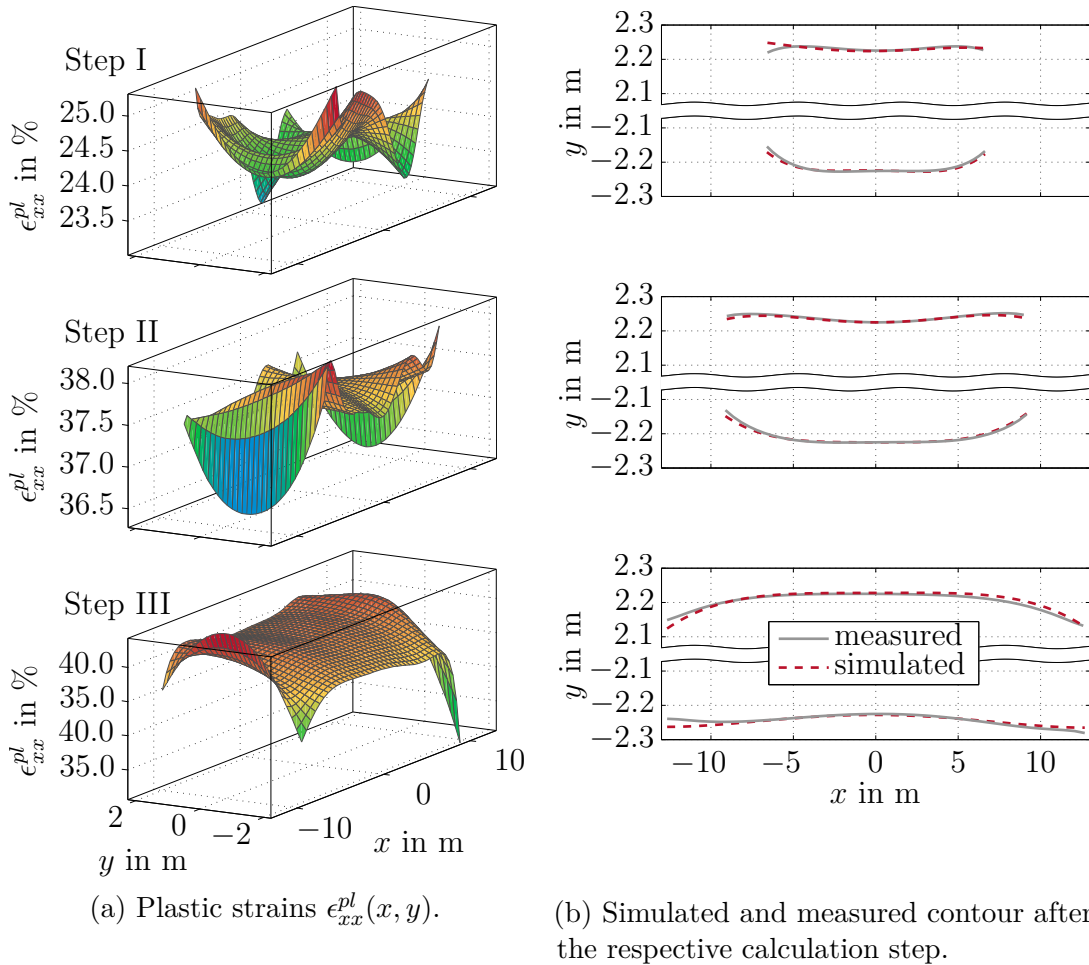


Figure 3.10: Results of the three calculation steps.

same hardware configuration as used for the contour measurement (cf. Section 2.6), a rolling pass can be simulated within less than 1 ms CPU time.

### 3.7 Summary

In this chapter, a continuum-mechanics-based model for the evolution of the plate contour was presented. The two-dimensional model predicts the contour after a rolling pass based on the contour before the rolling pass and the input and output thickness profiles. Simulation studies show that the influence of temperature gradients on the resulting plate contour can be neglected in the considered application. A validation of the model by means of measurements from a typical rolled plate demonstrates its high accuracy. In the following, the model of the contour evolution will be used in an optimization-based approach to reduce

contour errors in the subsequent pass. However, the presented quasi-static model does not cover the relation between the camber formation and the movement during the rolling pass and hence cannot be used for feedback control during the rolling pass. This is why a model linking the movement of the plate being clamped in the rolling gap with the camber formation is presented in the next chapter.

---

## Modeling of the plate movement during the rolling pass

---

A quasi-static mathematical model of the plate contour based on the input and output thickness profiles of the plate was presented in Chapter 3. Online feedback control during the rolling pass, however, requires also a mathematical model of the movement of the plate during the rolling pass. Therefore, a model covering the rotational movement and the camber formation during the rolling pass is discussed in this chapter. This model will serve as the basis for an online feedback control approach utilizing measurements of the plate contour and of the angular velocity of the plate up- and downstream of the mill stand. Fig. 4.1 shows a top view of the mill stand with the global coordinate frame  $(\xi, \eta, \zeta)$  (Eulerian coordinates). It is assumed that the material flow in the rolling gap is strictly perpendicular to the work roll axis, which implies that lateral spread of the plate in the rolling gap is neglected. The camber characterized by the lateral displacement  $\delta(\xi)$  of the centerline of the plate is of interest (cf. Fig. 4.1). The displacement  $\delta(\xi)$  is the arithmetical mean of the coordinates  $\eta$  of the longitudinal boundaries of the plate. Clearly,  $\delta(\xi)$  is a function of the time  $t$  because of the motion and deformation of the plate. For the sake of readability, the argument  $t$  is omitted in the following. The centerline  $\delta(\xi)$  can be computed based on the contour measurement. The local slope  $\delta'(\xi)$  of the centerline (with respect to the axis  $\xi$ ) is

$$\delta'(\xi) = \frac{\partial \delta(\xi)}{\partial \xi}$$

and the local curvature  $\delta''(\xi)$  follows in the form

$$\delta''(\xi) = \frac{\frac{\partial^2 \delta(\xi)}{\partial \xi^2}}{\left(1 + \left(\frac{\partial \delta(\xi)}{\partial \xi}\right)^2\right)^{\frac{3}{2}}} \approx \frac{\partial^2 \delta(\xi)}{\partial \xi^2}. \quad (4.1)$$

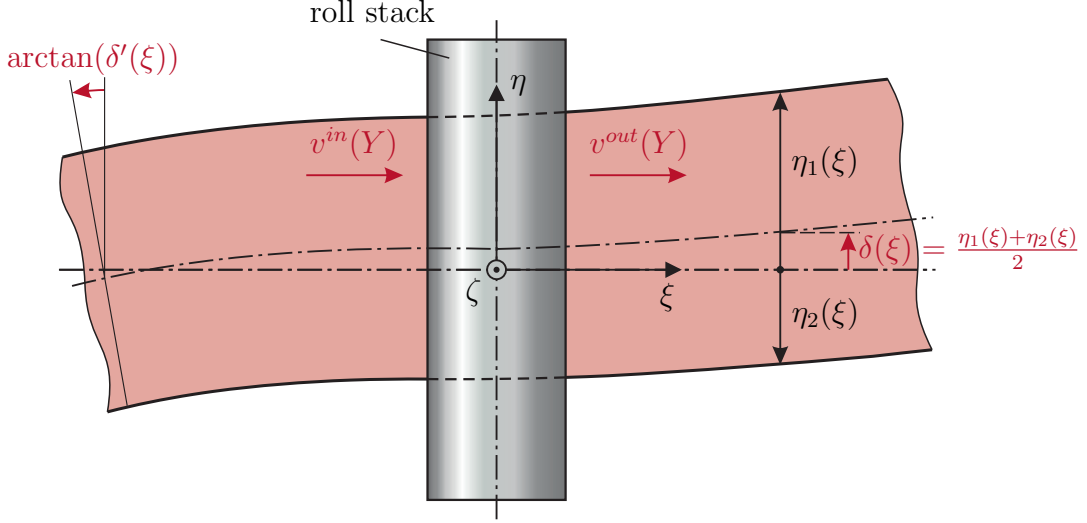


Figure 4.1: Top view of the rolling process.

Because the local slope  $\delta'(\xi)$  is expected to be very small the curvature  $\delta''(\xi)$  can be approximated by  $\partial^2\delta(\xi)/\partial\xi^2$ .

## 4.1 Movement of the plate

Consider the Lagrangian coordinate

$$Y = \eta - \delta(\xi)$$

which points along the direction  $\eta$  because the influence of the very small local slope  $\delta'(\xi)$  on the Lagrangian coordinate  $Y$  can be neglected.  $Y = 0$  holds at the centerline of the plate and  $Y = \pm w/2$  defines the boundaries of the plate, with  $w$  as the width of the plate. Neglecting any bending deflection or crown of the work rolls, the rolling gap height can be formulated as

$$h^{out}(Y) = \bar{h}^{out} + \tilde{h}^{out}(Y) = \bar{h}^{out} + \Delta h^{out} \frac{Y}{w}, \quad (4.2)$$

which implies  $\bar{h}^{out} = (h^{out}(w/2) + h^{out}(-w/2))/2$  and  $\Delta h^{out} = h^{out}(w/2) - h^{out}(-w/2)$ . In the same way, the input thickness at  $\xi = 0$  is parameterized in the form

$$h^{in}(Y) = \bar{h}^{in} + \tilde{h}^{in}(Y) = \bar{h}^{in} + \Delta h^{in} \frac{Y}{w}. \quad (4.3)$$

The plate enters the rolling gap with the velocity  $v^{in}(Y)$  and leaves it with the velocity  $v^{out}(Y)$ . These two velocities are linked at the point  $\xi = 0$  by the continuity equation

$$v^{in}(Y)h^{in}(Y) = v^{out}(Y)h^{out}(Y). \quad (4.4)$$



Specialization of (4.4) for  $Y = 0$  yields

$$\bar{v}^{in} \bar{h}^{in} = \bar{v}^{out} \bar{h}^{out} \quad (4.5)$$

with the spatial mean values  $\bar{v}^{in}$  and  $\bar{v}^{out}$  of the upstream and downstream velocities  $v^{in}(Y)$  and  $v^{out}(Y)$ , respectively. Because there are no external loads outside the rolling gap, the motion of the plate can be characterized as a rigid-body displacement both upstream and downstream of the rolling gap. Due to the assumption of zero material flow along the lateral direction  $\eta$  in the rolling gap, the upstream plate velocity  $v^{in}(Y)$  is given by

$$v^{in}(Y) = \bar{v}^{in} - Y\omega^{in}$$

and the downstream plate velocity  $v^{out}(Y)$  by

$$v^{out}(Y) = \bar{v}^{out} - Y\omega^{out}.$$

The upstream mean translational velocity follows in the form

$$\bar{v}^{in} = \frac{v^{in}(-w/2) + v^{in}(w/2)}{2}$$

and the upstream angular velocity is

$$\omega^{in} = \frac{v^{in}(-w/2) - v^{in}(w/2)}{w}$$

with respect to the axis  $\zeta$  at the origin. Similarly, the downstream mean translational velocity follows in the form

$$\bar{v}^{out} = \frac{v^{out}(-w/2) + v^{out}(w/2)}{2}$$

and the downstream angular velocity is

$$\omega^{out} = \frac{v^{out}(-w/2) - v^{out}(w/2)}{w}. \quad (4.6)$$

The mean velocity of the downstream plate follows from (4.5) in the form  $\bar{v}^{out} = \bar{v}^{in} \bar{h}^{in} / \bar{h}^{out}$ . The local velocity of the downstream plate follows from (4.4) in the form

$$v^{out}(Y) = v^{in}(Y) \frac{\bar{h}^{in} + \Delta h^{in} \frac{Y}{w}}{\bar{h}^{out} + \Delta h^{out} \frac{Y}{w}}, \quad (4.7)$$

where (4.2) and (4.3) have been inserted. The asymmetry of the input thickness and the asymmetry of the rolling gap height are expected to be small compared

to their mean values. Therefore, it is reasonable to linearize (4.7) at the point  $\Delta h^{in} = \Delta h^{out} = 0$  resulting in

$$v^{out}(Y) \approx (\bar{v}^{in} - Y\omega^{in}) \left( \frac{\bar{h}^{in}}{\bar{h}^{out}} + \frac{Y}{w\bar{h}^{out}}\Delta h^{in} - \frac{\bar{h}^{in}Y}{w(\bar{h}^{out})^2}\Delta h^{out} \right). \quad (4.8)$$

Insertion of (4.8) into (4.6) yields

$$\omega^{out} = \frac{\bar{v}^{in}}{w} \left( \frac{\bar{h}^{in}}{(\bar{h}^{out})^2}\Delta h^{out} - \frac{1}{\bar{h}^{out}}\Delta h^{in} \right) + \frac{\bar{h}^{in}}{\bar{h}^{out}}\omega^{in}. \quad (4.9)$$

That is, the angular velocity  $\omega^{out}$  of the downstream plate depends on the velocities of the upstream plate ( $\bar{v}^{in}$  and  $\omega^{in}$ ) and the input and output thickness of the plate. Here, a model of the forward and backward slip, see, e. g., [44] and [45], is not needed because the upstream as well as the downstream longitudinal and angular velocities are assumed to be measurable.

## 4.2 Evolution of the camber

The evolution of the camber defined in terms of the plate curvature  $\delta''(\xi)$  and its nexus with the angular velocities  $\omega^{in}$  and  $\omega^{out}$  of the plate are analyzed in the following. The objective of this analysis is to explore whether the camber can be computed based on the measurement of the angular velocities  $\omega^{in}$  and  $\omega^{out}$  and the longitudinal velocities  $\bar{v}^{in}$  and  $\bar{v}^{out}$  of the plate according to Chapter 2. If the machine vision system is directly used for camber measurement of the part of the plate that is currently in the FOV of the camera, there is an inherent transport delay between camber generation and camber measurement. This delay is clearly undesirable for feedback control of the camber. However, this delay can be avoided by using measurements of the angular velocity of the plate.

The plate enters the rolling gap with the curvature  $(\delta^{in})'' = \delta''(0^-)$  and leaves it with the curvature  $(\delta^{out})'' = \delta''(0^+)$ . Because of the very small expected slope of the centerline  $\delta'(\xi)$ , the angle  $\varphi(\xi) = \arctan(\delta'(\xi))$  of the centerline may be approximated by  $\varphi(\xi) = \delta'(\xi)$  and the angular velocity of the material follows in the form

$$\underbrace{\frac{d\varphi(\xi, t)}{dt}}_{\omega} = \frac{\partial\delta'(\xi)}{\partial t} + \frac{\delta'(\xi)}{\partial\xi} \underbrace{\frac{d\xi}{dt}}_v.$$

Hence, the angle  $\delta'(0)$  changes according to

$$\frac{\partial\delta'(0^-)}{\partial t} + (\delta^{in})'' \bar{v}^{in} = \omega^{in} \quad (4.10a)$$

$$\frac{\partial\delta'(0^+)}{\partial t} + (\delta^{out})'' \bar{v}^{out} = \omega^{out}. \quad (4.10b)$$

Because of the thickness reduction  $\bar{h}^{out}/\bar{h}^{in}$  in the rolling gap at  $Y = 0$  and the associated elongation of the plate, the downstream slope  $\delta'(0^+)$  follows in the form

$$\delta'(0^+) = \frac{\bar{h}^{out}}{\bar{h}^{in}} \delta'(0^-). \quad (4.11)$$

Hence, the derivatives  $\delta'(\xi)$  and  $\delta''(\xi)$  can be discontinuous at  $\xi = 0$ . In the following, it is considered that  $\bar{h}^{out}/\bar{h}^{in}$  is constant. Elimination of  $\delta'(0^-)$  and  $\delta'(0^+)$  in (4.10) and (4.11) and insertion of (4.5) yields

$$(\delta^{out})'' = \frac{\omega^{out}}{\bar{v}^{out}} - \frac{\bar{h}^{out}}{\bar{h}^{in}} \frac{\omega^{in}}{\bar{v}^{out}} + \left( \frac{\bar{h}^{out}}{\bar{h}^{in}} \right)^2 (\delta^{in})'', \quad (4.12)$$

i. e., a relation between the angular velocities  $\omega^{in}$  and  $\omega^{out}$  and the curvature of the plate before and after the rolling gap.

### 4.3 Time-free formulation

So far, most of the quantities have been parameterized in terms of the time  $t$ . This implies that the dynamical behavior depends on the plate velocities  $\bar{v}^{in}$  and  $\bar{v}^{out}$ , which can vary, e. g., if the rotational speed of the work roll changes. Hence, the dynamical model is generally time variant and the transport delay between the mill stand and some downstream curvature measurement device can entail time delays of various lengths. These drawbacks can be circumvented if the processed downstream plate length is used as an independent coordinate instead of the time  $t$ . Let

$$X(t) = \int_0^t \bar{v}^{out}(\tau) d\tau \quad (4.13)$$

be the length of the already rolled part of the plate measured along the direction  $\xi$ . More precisely,  $X(t)$  is the curvilinear distance from the mill stand to the head end of the plate. During a rolling pass that starts at the time  $t = 0$  (head end of the plate enters the rolling gap),  $X(t)$  grows from 0 to the plate length. From (4.13), it follows that

$$\dot{X}(t) = \bar{v}^{out}(t) \quad (4.14)$$

or equivalently

$$dX = \bar{v}^{out}(t) dt.$$

Based on this relation, the angular displacements per unit processed plate length are defined in the form

$$\Omega^{in} = \frac{\omega^{in}}{\bar{v}^{out}} \quad (4.15a)$$

$$\Omega^{out} = \frac{\omega^{out}}{\bar{v}^{out}}. \quad (4.15b)$$

Insertion of these relations and (4.5) into (4.9) and (4.12) yields the time-free description of the camber evolution

$$\Omega^{out} = \frac{1}{w\bar{h}^{out}}\Delta h^{out} - \frac{1}{w\bar{h}^{in}}\Delta h^{in} + \frac{\bar{h}^{in}}{\bar{h}^{out}}\Omega^{in} \quad (4.16a)$$

$$(\delta^{out})'' = \Omega^{out} - \frac{\bar{h}^{out}}{\bar{h}^{in}}\Omega^{in} + \left(\frac{\bar{h}^{out}}{\bar{h}^{in}}\right)^2 (\delta^{in})''. \quad (4.16b)$$

Note that all variables in (4.16) can be formulated as functions of the variable  $X$  (in lieu of  $t$ ).

## 4.4 Validation

In this section, the model of the movement of the plate covering the static equations (4.16) is validated. For the validation of (4.16a), the input and the output thickness (mean value and asymmetry) of the plate have to be known. The reached tolerances of the mean thickness of the plate are tight and therefore the desired values of the input and output thickness are used for  $\bar{h}^{in}$  and  $\bar{h}^{out}$ . Hence, it is sufficient to measure the asymmetries of the input and output thickness. However, at the considered rolling mill a thickness measurement device is only installed downstream of the mill stand. Therefore, the thickness of the plate and hence the thickness asymmetry can only be measured after every second pass. This is why (4.16a) cannot be validated by means of measurements.

Contrary, (4.16b) can be validated because no thickness asymmetries appear in (4.16b). In the validation, the curvature of the downstream plate is calculated based on (4.16b) and then compared to the curvature calculated from the measurement of the downstream centerline according to (4.1). All necessary quantities in the validation are determined by the contour measurement approach from Chapter 2. A Savitzky-Golay filter with degree 3 and window length 31 is used to calculate the curvature based on the measurement of the centerline.

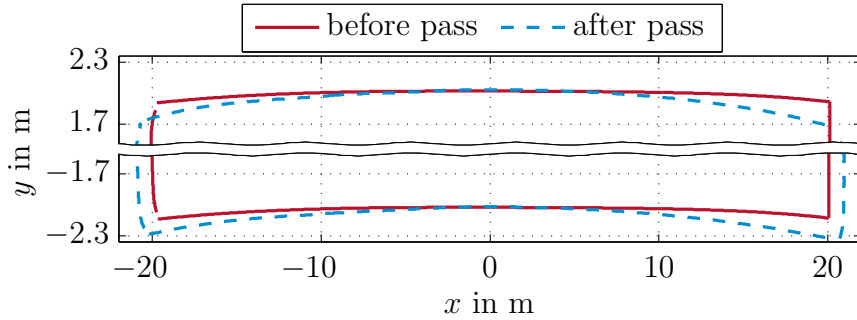


Figure 4.2: Contour of the plate before and after the considered rolling pass.

The curvature of the upstream plate can be calculated during the contour measurement itself based on the centerline of the already rolled part of the plate.

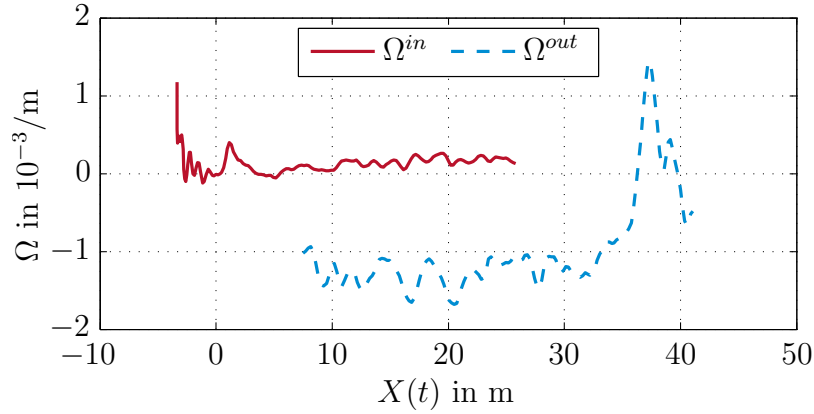


Figure 4.3: Measured upstream and downstream angular displacements  $\Omega^{in}$  and  $\Omega^{out}$ , respectively.

However, the curvature of the downstream plate can only be calculated after the contour measurement at the downstream camera. To this end, the measured plate contour is shifted in time based on the movement of the plate to compensate for the transport delay and to determine the curvature in the rolling gap.

Clearly, the curvature of the upstream plate of the actual pass could be determined from the measured downstream contour of the previous pass. However, as the upstream measurements of the angular movement and the curvature should be compatible, the upstream curvature is determined by means of the upstream contour measurement.

The thickness of the plate used in the validation is reduced from 19.9 mm to 18.5 mm in the considered pass. Fig. 4.2 shows the measured contours before and after the rolling pass of the plate with a desired plate length of 43.3 m.

Furthermore, Fig. 4.3 shows the measured upstream and downstream angular displacements as a function of the already rolled plate length  $X$ . Only the overlapping part of the angular displacements in Fig. 4.3 can be used for the validation of (4.16b). Hence, the measurements of a long plate are used for the validation to have a large overlap.

In this scenario, the upstream angular displacement of the plate is almost zero. This is because the upstream side guides were positioned close to the plate edges to prevent the plate from rotations and from moving sideways. Contrary, the downstream plate can rotate due to the opened downstream side guides. For rolled plate lengths  $X(t)$  larger than approximately 35 m, the plate is no longer between the upstream side guides. This leads to a change of the almost constant downstream angular displacement of the plate (cf. Fig. 4.3).

Fig. 4.4 shows the measured and the calculated downstream curvature of the considered plate. The mismatch between the measured and the calculated values is in an acceptable range. The missing upstream guidance of the plate for  $X \geq 35$  m may also be seen in Fig. 4.4. It leads to a higher magnitude of the

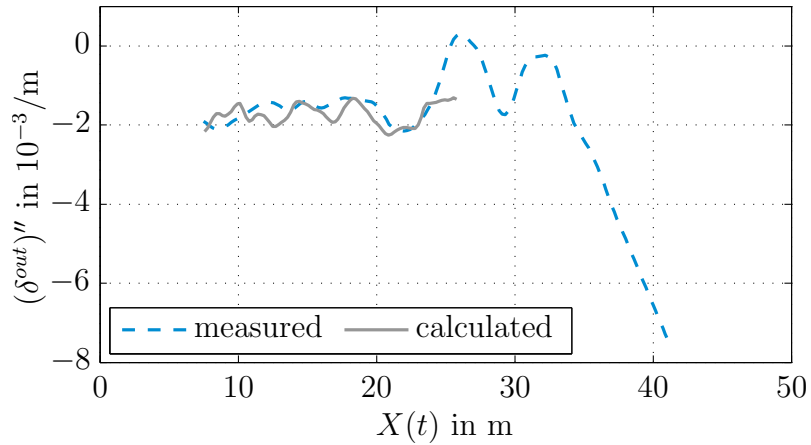


Figure 4.4: Measured and calculated downstream curvature of the plate  $(\delta^{out})''$ .

curvature near the end of the plate.

## 4.5 Summary

A model describing the nexus between the movement of the plate and the evolution of the centerline of the plate during a rolling pass was discussed in this chapter. The model was validated by means of measurements of a plate rolled during the standard production process. The model will be used in a feedback control approach to reduce errors between the desired and the actual curvature of the centerline during the rolling pass. In particular, a new two degrees-of-freedom control structure with a Smith-predictor utilizing the time-delay free measurement of the angular velocity is presented in the following chapter.

---

### Model-based control of the contour evolution

---

In this chapter, the method to measure the plate contour presented in Chapter 2 as well as the mathematical models from Chapters 3 and 4 are utilized in different control approaches to reduce contour errors during the rolling process. A feedforward strategy is discussed first. Here, the measurement of the plate contour is used to determine the required asymmetry of the output thickness profile to obtain the desired contour after the rolling pass. This approach requires knowledge of the input asymmetry before the rolling pass. Because a measurement of the input asymmetry is not available in every rolling pass, a method to estimate this quantity based on contour measurements is presented.

Despite the feedforward controller, imperfections like disturbances, model plant mismatches, or inaccurate rolling gap control may lead to a deviation between the required and the actual output thickness profile and hence to a deviation between the desired and the resulting contour. In particular after the last rolling pass, no further correction of the contour is possible with the discussed feedforward approach. Hence, an additional feedback controller seems favorable to reduce contour errors emerging during the current rolling pass.

The FOV of the camera used for the measurement of the plate contour is located a few meters downstream of the rolling gap. Hence, the resulting plate contour is measured with a time delay (transport delay), which in general complicates the use of feedback controllers. However, the angular velocity of the plate is linked with the contour evolution. The measurement of the angular velocity does not have a delay and is therefore utilized in the presented feedback control approach. In particular, a two degrees-of-freedom (2-DOF) control structure with a Smith-predictor, i. e. a combination of a feedforward controller and a feedback Smith-predictor controller is used. Furthermore, the proof of robust stability of the proposed control concept is given.

The automation system installed at the considered rolling mill allows two different ways to adjust the rolling gap height. First, the desired output thickness can be set before the beginning of the next pass, which is used to apply the feedforward approach. Second, an extra value may be added to the set point of the asymmetry during the rolling pass, which makes feedback control possible during the rolling pass.

Consider a plate with a homogeneous thickness and a camber. In general, the compensation of the camber within a single pass results in an inhomogeneous thickness after the rolling pass. This drawback can be avoided by using a control approach covering several passes. Then, the output thickness in interim passes is determined such that both the desired contour and a homogeneous thickness of the final plate can be simultaneously achieved. Parts of this chapter have been published in [28] and [29].

## 5.1 Single pass-to-pass adjustment of the rolling gap (feedforward control)

In this section, an optimization-based reduction of camber of heavy plates is presented. To this end, the contour measurement described in Chapter 2 is used to determine the downstream plate contour. Based on the mathematical model discussed in Chapter 3 and the measured contour, the required asymmetry of the output thickness to achieve the desired contour after the next pass is computed. The calculation is performed once after every pass. Based on the

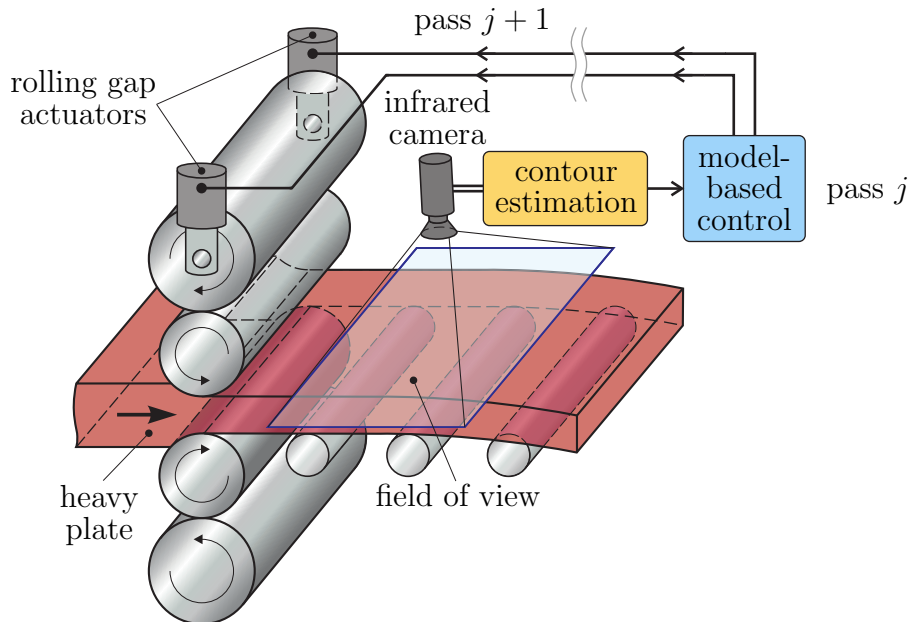


Figure 5.1: Overview of the camber reducing feedforward control approach.



required asymmetry to reduce the camber, the actuators of the rolling gap (cf. Fig. 5.1) are adjusted using the subordinate automatic gauge control (AGC) system, see, e. g., [46].

### 5.1.1 Parameterization of the thickness profiles and the centerline

The optimization-based methods presented in this section require a parameterization of the thickness profile of the plate. The automation system installed at the considered rolling mill can adjust the center-thickness  $\bar{h}^{out}$  and the asymmetry  $\Delta h^{out}$  of the rolling gap height according to desired values defined on a regular spatial grid in the longitudinal direction of the plate. A linear interpolation is performed between the grid points. Consequently, the profile of the output thickness  $h^{out}(x, y)$  is parameterized as

$$h^{out}(x, y) = \bar{h}_i^{out} + \frac{\bar{h}_{i+1}^{out} - \bar{h}_i^{out}}{x_{i+1} - x_i} (x - x_i) + \frac{y}{w} \left[ \Delta h_i^{out} + \frac{\Delta h_{i+1}^{out} - \Delta h_i^{out}}{x_{i+1} - x_i} (x - x_i) \right] \quad \forall x_i \leq x \leq x_{i+1} \quad (5.1)$$

with the grid points  $x_i, i = 1, \dots, N_P$  and the plate width  $w$ . The center-thickness  $h^{out}(x, 0)$  may be adjusted by the coefficients  $\bar{h}_i^{out}, i = 1, \dots, N_P$ , whereas the coefficients  $\Delta h_i^{out}$  determine the asymmetry of the output thickness. The profile of the input thickness  $h^{in}(x, y)$  is parameterized analogously using the coefficients  $\bar{h}_i^{in}$  and  $\Delta h_i^{in}, i = 1, \dots, N_P$ .

Additionally, the centerline of the plate as shown in Fig. 5.2 is parameterized by  $\delta(x)$  and is used as an aggregate measure of the lateral plate contour. The centerline  $\delta^{in}(x)$  of the plate before the rolling pass is calculated in the form (see Fig. 3.3)

$$\delta^{in}(x) = \frac{p_{B1}(x) + p_{B3}(x)}{2} \quad (5.2)$$

with the polynomials  $p_{B1}(x)$  and  $p_{B3}(x)$  of degree  $N_B$  of the longitudinal edges of the plate. The polynomials  $p_{B1}(x)$  and  $p_{B3}(x)$  follow from a least-squares approximation of the longitudinal boundaries of the plate before the rolling pass. The predicted centerline  $\delta_{pred}^{out}(x)$  of the plate after the rolling pass follows as (cf. Fig. 5.2)

$$\delta_{pred}^{out}(x + u(x, \delta^{in}(x))) = \delta^{in}(x) + v(x, \delta^{in}(x))$$

with the displacements  $u(x, y)$  and  $v(x, y)$  from (3.12).

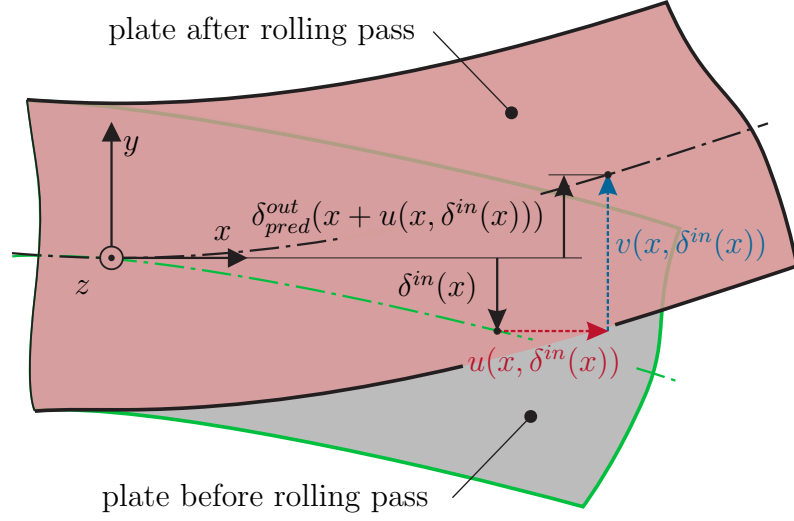


Figure 5.2: Centerline of the plate before and after the rolling pass.

### 5.1.2 Approximation of the plastic strain

The mathematical model of the camber evolution expects the plastic strain to be parameterized as a polynomial (cf. (3.22)). However, the parameterization of the input and output thickness according to (5.1) does not directly yield a polynomial strain (cf. (3.1)). Therefore, the plastic strain (3.1) is approximated by the polynomial representation (3.22) using a weighted residual method, see, e. g., [41]. To this end, the residual

$$\mathcal{R} = \left( \frac{h^{in}(x, y)}{h^{out}(x, y)} - 1 \right) - \underbrace{\sum_{i=0}^{P_x} \sum_{q=0}^{P_y} c_{xx,i,q} x^i y^q}_{\boldsymbol{\lambda}^T(x, y) \mathbf{c}}$$

is forced to vanish in a weighted integral sense, i. e.,

$$\iint_I \lambda(x, y) \mathcal{R} dx dy = 0. \quad (5.3)$$

The coefficients  $c_{xx,i,q}$  are arranged in the vector  $\mathbf{c}$  and the vector  $\boldsymbol{\lambda}(x, y)$  contains the corresponding terms  $x^i y^q$ . In (5.3), the weighting function is denoted by  $\lambda(x, y)$  and the integration domain  $I$  is the area of the plate as shown in Fig. 3.3. It is required that (5.3) vanishes for each element of  $\boldsymbol{\lambda}$  used as weighting function  $\lambda(x, y)$ . This approach yields the coefficient vector  $\mathbf{c}$  as solution of the linear equation

$$\mathbf{A} \mathbf{c} = \mathbf{b} \quad (5.4)$$

with the matrix

$$\mathbf{A} = \iint_I \boldsymbol{\lambda} \boldsymbol{\lambda}^T dx dy \quad (5.5)$$

and the vector

$$\mathbf{b} = \iint_I \left( \frac{h^{in}(x, y)}{h^{out}(x, y)} - 1 \right) \boldsymbol{\lambda} dx dy. \quad (5.6)$$

The numerical properties of (5.4) are of good nature iff the components of  $\boldsymbol{\lambda}$  are linearly independent because then  $\mathbf{A}$  is positive definite. The integrations are performed analytically in (5.5) and by means of Gaussian quadrature in (5.6).

### 5.1.3 Formulation of the optimization problem

In the following, the asymmetry of the output thickness  $\Delta h_i^{out}$ ,  $i = 1, \dots, N_P$  is adjusted to reduce the camber. The coefficients  $\bar{h}_i^{out}$  of the center-thickness are set to the desired thickness value  $h_{des}^{out}$ , i. e.,  $\bar{h}_i^{out} = h_{des}^{out}$ . Additionally, the profile of the input thickness  $h^{in}(x, y)$  has to be known. At the considered rolling mill, measurements of the input thickness profile are not available at every pass because there is only one thickness measurement device. It is located downstream of the rolling mill and the thickness over the whole plate is only measured after the last pass in the standard production process. Hence, instead of using measurements to determine the coefficients  $\bar{h}_i^{in}$  of the center-thickness, they are set to the desired plate thickness of the previous pass. The asymmetry of the input thickness characterized by  $\Delta h_i^{in}$ ,  $i = 1, \dots, N_P$  is estimated based on the method presented in Section 5.1.4.

The asymmetry of the output thickness  $\Delta h_i^{out}$  is determined by solving the optimization problem

$$\min_{\Delta \mathbf{h}^{out} \in \mathbb{R}^{N_P}} J(\Delta \mathbf{h}^{out}) \quad (5.7a)$$

with

$$\Delta \mathbf{h}^{out} = [\Delta h_1^{out} \quad \Delta h_2^{out} \quad \dots \quad \Delta h_{N_P}^{out}]^T$$

and the objective function

$$\begin{aligned} J(\Delta \mathbf{h}^{out}) &= \frac{1}{M_{CL}} \sum_{j=1}^{M_{CL}} \left( (\delta_{des}(\bar{x}_j))'' - (\delta_{pred}^{out}(\bar{x}_j))'' \right)^2 + \frac{\beta_1}{N_P} \sum_{i=1}^{N_P} (\Delta h_i^{out})^2 \\ &+ \frac{\beta_2}{N_P - 1} \sum_{i=1}^{N_P-1} \left( \frac{\Delta h_{i+1}^{out} - \Delta h_i^{out}}{x_{i+1} - x_i} \right)^2 + \frac{\beta_3}{N_P} \sum_{i=1}^{N_P} P(\Delta h_i^{out}). \end{aligned} \quad (5.7b)$$

Here, the curvature of the desired centerline is denoted by  $(\delta_{des}(x))''$  and  $M_{CL}$  is the number of values used for evaluating the curvature deviation  $(\delta_{des}(x))'' - (\delta_{pred}^{out}(x))''$  on an equally spaced grid  $\bar{x}_j$ ,  $j = 1, \dots, M_{CL}$ . In general, a straight centerline is desired, i. e.,  $(\delta_{des})'' = 0$ .

Besides weighting the difference between the desired and the predicted curvature of the centerline, the positive constants  $\beta_1$  and  $\beta_2$  are used to weight the asymmetry of the output thickness and its variation along the plate length, respectively. Note that  $x_i$ ,  $i = 1, \dots, N_P$ , represents a grid point of the parameterization of the output thickness (cf. (5.1)).

The term  $\beta_3/N_P \sum_{i=1}^{N_P} P(\Delta h_i^{out})$  with  $\beta_3 > 0$  penalizes asymmetries outside the allowed range  $\Delta h_i^{out} \in [\Delta h_{min,i}^{out}, \Delta h_{max,i}^{out}]$ . The penalty function

$$P(\Delta h_i^{out}) = \begin{cases} (\Delta h_i^{out} - \Delta h_{min,i}^{out})^2 & \text{if } \Delta h_i^{out} < \Delta h_{min,i}^{out} \\ (\Delta h_i^{out} - \Delta h_{max,i}^{out})^2 & \text{if } \Delta h_i^{out} > \Delta h_{max,i}^{out} \\ 0 & \text{else} \end{cases}$$

is used to form a soft constraint, see, e. g., [47]. This soft-constraint formulation does not ensure that the constraints  $\Delta h_{min,i}^{out} \leq \Delta h_i^{out} \leq \Delta h_{max,i}^{out}$  are exactly fulfilled. However, a properly chosen weighting factor  $\beta_3$  keeps the violation of the constraints within an acceptable range. Note that (5.7b) is a sum of squares and can be written in the form  $J(\Delta \mathbf{h}^{out}) = \mathbf{e}^T \mathbf{e}$  with the vector  $\mathbf{e}$ . This quadratic form of the objective function (5.7b) facilitates the use of the Gauss-Newton method (cf. Appendix A.3) with the line search from Appendix A.4.1 to solve the optimization problem.

Three termination criteria are used to decide whether the solution  $\Delta \mathbf{h}_l^{out}$  of the current iteration  $l$  is acceptable:

- The change of the optimization variable is sufficiently small, i. e.,  $\|\Delta \mathbf{h}_{l+1}^{out} - \Delta \mathbf{h}_l^{out}\|_\infty < \bar{\gamma}_x$  with a constant  $\bar{\gamma}_x > 0$ .
- The value of the objective function is small enough, i. e.,  $J(\Delta \mathbf{h}_l^{out}) < \bar{\gamma}_J$  with a tuning parameter  $\bar{\gamma}_J > 0$ .
- The improvement of the objective function achieved in the current iteration is smaller than the constant  $\bar{\gamma}_{dJ} > 0$ , i. e.,  $J(\Delta \mathbf{h}_l^{out}) - J(\Delta \mathbf{h}_{l+1}^{out}) < \bar{\gamma}_{dJ}$ .

#### 5.1.4 Estimation of the thickness asymmetry

The presented method for the reduction of contour errors requires the knowledge of the thickness asymmetry before the rolling pass. Because the thickness profile is not measured after every rolling pass, a method to estimate the thickness asymmetry is presented in this section. Clearly, the output thickness asymmetry of the actual pass is the relevant input asymmetry of the consecutive pass. In

the estimation approach, the parameterization from (5.1) is used for the input and output thickness profiles. The estimated values of the asymmetry coefficients  $\Delta h_i^{out}$ ,  $i = 1, \dots, N_P$  are denoted by  $\Delta \hat{h}_i^{out}$ . Again, the coefficients of the center-thickness  $\bar{h}_i^{in}$  and  $\bar{h}_i^{out}$ ,  $i = 1, \dots, N_P$  are set to their desired values. Additionally, the asymmetry coefficients of the input thickness profile  $\Delta h_i^{in}$  are assumed to be known. The estimated asymmetry of the output thickness characterized by the coefficients  $\Delta \hat{h}_i^{out}$ ,  $i = 1, \dots, N_P$  is found by solving the optimization problem

$$\min_{\Delta \hat{\mathbf{h}}^{out} \in \mathbb{R}^{N_P}} \hat{J}(\Delta \hat{\mathbf{h}}^{out}) \quad (5.8a)$$

with the objective function

$$\begin{aligned} \hat{J}(\Delta \hat{\mathbf{h}}^{out}) = & \frac{1}{M_{CL}} \sum_{j=1}^{M_{CL}} \left( (\delta^{out}(\bar{x}_j))^{\prime\prime} - (\delta_{pred}^{out}(\bar{x}_j))^{\prime\prime} \right)^2 + \frac{\hat{\beta}_1}{N_P} \sum_{i=1}^{N_P} (\Delta \hat{h}_i^{out})^2 \\ & + \frac{\hat{\beta}_2}{N_P - 1} \sum_{i=1}^{N_P-1} \left( \frac{\Delta \hat{h}_{i+1}^{out} - \Delta \hat{h}_i^{out}}{x_{i+1} - x_i} \right)^2 + \frac{\hat{\beta}_3}{N_P} \sum_{i=1}^{N_P} P(\Delta \hat{h}_i^{out}) \end{aligned} \quad (5.8b)$$

and the vector of the optimization variables

$$\Delta \hat{\mathbf{h}}^{out} = [\Delta \hat{h}_1^{out} \quad \Delta \hat{h}_2^{out} \quad \dots \quad \Delta \hat{h}_{N_P}^{out}]^T.$$

The centerline of the plate after the rolling pass  $\delta^{out}$  is calculated similarly to the centerline before the rolling pass (cf. (5.2)) based on the measurement of the plate contour.  $M_{CL}$  denotes the number of values used to evaluate the curvature of the centerline on an equidistant spatial grid  $\bar{x}_j$ ,  $j = 1, \dots, M_{CL}$ . The term  $\hat{\beta}_1/N_P \sum_{i=1}^{N_P} (\Delta \hat{h}_i^{out})^2$  may be omitted in the objective function. However, a properly chosen weighting factor  $\hat{\beta}_1$  leads to a numerically good-natured optimization problem while affecting the accuracy of its solution only insignificantly. The term with the weighting factor  $\hat{\beta}_2$  may be used to reduce the noise on the estimation result because it penalizes the change between neighboring asymmetry coefficients  $\Delta \hat{h}_i^{out}$ . The objective function (5.8b) also features a soft constraint to limit the estimated output asymmetry to the range  $\Delta \hat{h}_i^{out} \in [\Delta \hat{h}_{min,i}^{out}, \Delta \hat{h}_{max,i}^{out}]$  by choosing an appropriate weighting factor  $\hat{\beta}_3$ . Due to the similarity of (5.8) with (5.7), the Gauss-Newton method is also suitable for solving the optimization problem (5.8). Three termination criteria are used to decide whether the solution  $\Delta \hat{\mathbf{h}}_l^{out}$  of the current iteration  $l$  is acceptable:

- The change of the optimization variable is sufficiently small, i. e.,  $\|\Delta \hat{\mathbf{h}}_{l+1}^{out} - \Delta \hat{\mathbf{h}}_l^{out}\|_{\infty} < \hat{\gamma}_x$  with a constant  $\hat{\gamma}_x > 0$ .
- The value of the objective function is small enough, i. e.,  $\hat{J}(\Delta \hat{\mathbf{h}}_l^{out}) < \hat{\gamma}_J$  with a tuning parameter  $\hat{\gamma}_J > 0$ .

- The improvement of the objective function achieved in the current iteration is smaller than the constant  $\hat{\gamma}_{dJ} > 0$ , i. e.,  $\hat{J}(\Delta\hat{\mathbf{h}}_l^{out}) - \hat{J}(\Delta\hat{\mathbf{h}}_{l+1}^{out}) < \hat{\gamma}_{dJ}$ .

The presented approach allows the estimation of the output thickness profile of a single pass. Hence, if an initial thickness measurement of the plate is available, the first estimation of the output thickness profile may be performed. The estimated output thickness profile is then used as input thickness profile of the asymmetry estimation of the next pass and so forth. This recurrent estimation approach yields the input thickness profiles needed in the camber reduction approach from Section 5.1.3.

An accurate estimation result has been observed for thin plates whereas the estimation results are less accurate for thick plates. This behavior is due to the limited accuracy of the contour estimation in the range of one centimeter and due to the fact that large thickness asymmetries are necessary to produce a measurable camber on thick plates. Hence, the estimation of the thickness asymmetry is only performed for passes with a desired output plate thickness lower than the constant  $h_{est,max}^{out}$ . A limitation of the estimated output asymmetry is not mandatory in (5.8). However, the constraint is used as a safety measure to avoid excessive estimated asymmetries for thick plates.

Beside its usage in the pass-to-pass camber reduction approach, the estimation of the asymmetry can be used to monitor the condition of the mill stand during the rolling process. It allows, for instance, the identification and compensation of deviations between the desired and actual output asymmetry of the plate.

### 5.1.5 Compensation of the asymmetric mill stand deflection

Due to the rolling forces, the mill stand is subject to an elastic deflection of up to 14 mm. Generally, the compliance of the mill stand is not strictly the same on the drive side and on the operator side, which brings along a deflection that is asymmetric in the lateral direction and hence causes a cambered plate. The effect of this imperfection is analyzed by means of the evolution of the centerline of a plate rolled with zero control action (nominal value  $\Delta h_i^{out} = 0$ ) at the considered reversing mill stand. As shown in Fig. 5.3, the maximum lateral deviation  $\delta_{max}$  of the centerline of the plate (cf. Fig. 2.12) is unacceptably large and changes its sign although the nominal asymmetry of the output thickness profile is kept constant. The first passes show a positive camber, while  $\delta_{max}$  becomes negative in the last pass ending up with  $\delta_{max} \approx -20$  cm. Similar evolutions of the centerline have been observed for many other plates rolled without any form of camber correction.

This remarkable behavior seems to be linked with the respective rolling force. It is assumed that a change of the rolling force from one pass to the next pass may lead to a different asymmetry of the output thickness. For the considered plate, the averages of the measured total rolling force are shown in the lower

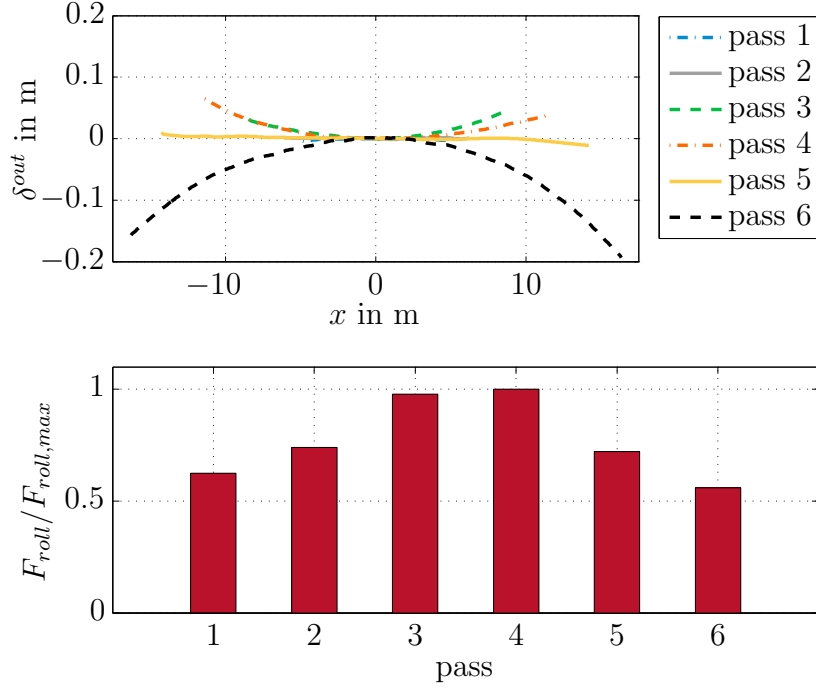


Figure 5.3: Measured evolution of the centerline for nominal values  $\Delta \mathbf{h}^{out} = \mathbf{0}$  and averages of the measured normalized rolling force.

part of Fig. 5.3. The figure indicates that the desired control action  $\Delta h_i^{out}$  is not accurately realized. Clearly, such a mismatch between the desired and the realized control action may jeopardize the effectivity of any camber control approach.

To analyze the asymmetric deflection of the mill stand, the dependence of the thickness asymmetry on the rolling force needs to be known. During a measurement campaign the thickness profile of the plate was measured after every forward pass. The thickness asymmetry of the plate after the backward pass was estimated using the approach presented in Section 5.1.4. In this approach, the measured input asymmetry and the measured contours before and after the considered rolling pass are used to estimate the output thickness asymmetry after the pass. Based on the measured and estimated thickness asymmetries of different plates and rolling passes, an almost linear relation between the disturbance of the output thickness asymmetry and the applied rolling forces can be observed. Moreover, this behavior is different for forward and backward rolling passes. Hence, the disturbance  $\Delta h_{dist}^{out}$  of the thickness asymmetry is empirically formulated as

$$\Delta h_{dist}^{out} = \begin{cases} \frac{w}{w_{cyl}} \Delta h_0 + \frac{w}{w_{cyl}} k_{fwd} F_{roll} & \text{in forward passes} \\ \frac{w}{w_{cyl}} \Delta h_0 + \frac{w}{w_{cyl}} k_{bwd} F_{roll} & \text{in backward passes} \end{cases} \quad (5.9)$$

with the compliance constants  $k_{fwd}$  and  $k_{bwd}$  for rolling passes in the forward and backward direction, respectively. Furthermore,  $\Delta h_0$  denotes an unknown offset of

the asymmetry and  $w_{cyl}$  is the lateral distance between the cylinders of the rolling gap actuator. The term  $w/w_{cyl}$  maps the asymmetric deflection of the mill stand to the output asymmetry of the plate, which has the width  $w$ . The deflection constants were identified as  $k_{fwd} = 15.0 \mu\text{m}/\text{MN}$  and  $k_{bwd} = 17.4 \mu\text{m}/\text{MN}$  utilizing the least-squares method and measurements of different plates and rolling passes.

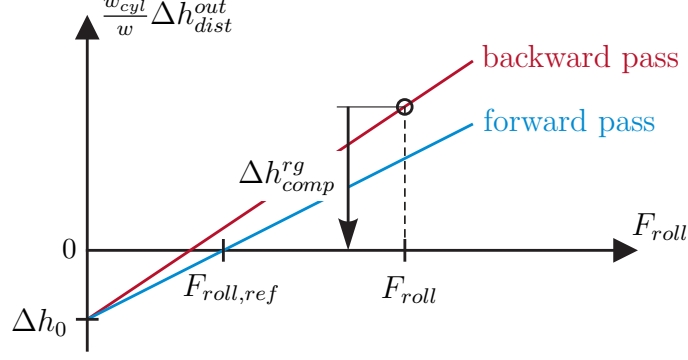


Figure 5.4: Compensation of the asymmetric deflection of the rolling mill relative to the reference rolling force  $F_{roll,ref}$ .

The idea of the compensation approach is to supplement the desired asymmetry of the rolling gap actuator by a compensation term  $\Delta h_{comp}^{rg}$  such that the disturbance (5.9) on the thickness asymmetry vanishes. The value of  $\Delta h_0$  in (5.9) may change because after every change of the work rolls a calibration routine that can modify  $\Delta h_0$  is performed. Here, the tilt of the rolls is manually adjusted to obtain a symmetric rolling gap profile in forward direction when applying the reference rolling force  $F_{roll,ref}$ . Therefore, the compensation  $\Delta h_{comp}^{rg}$  is done relatively to the deflection caused by the reference rolling force  $F_{roll,ref}$  (cf. Fig. 5.4) and is formulated as

$$\Delta h_{comp}^{rg} = \begin{cases} k_{fwd} (F_{roll,ref} - F_{roll}) & \text{in forward passes} \\ k_{fwd} F_{roll,ref} - k_{bwd} F_{roll} & \text{in backward passes} \end{cases}. \quad (5.10)$$

Note that the compensation  $\Delta h_{comp}^{rg}$  is defined at the lateral distance of the cylinders of the rolling gap actuator and is therefore independent of the plate width. The reference rolling force  $F_{roll,ref}$  is chosen in the range of the rolling forces applied during the last pass of the plates from the future production schedule.

### 5.1.6 Combination of feedforward control and asymmetry estimation

This section describes the combination of the feedforward control approach from Section 5.1.3 with the method to estimate the asymmetry from Section 5.1.4. Under real rolling conditions, the output asymmetry of the plate can be subject



to disturbances, e. g., due to a non-ideal control of the rolling gap actuators. That is, there exists a deviation between the desired output asymmetry  $\Delta \mathbf{h}^{out}$  and the estimated (real) output asymmetry  $\Delta \hat{\mathbf{h}}^{out}$ . The estimated deviation  $\Delta \tilde{\mathbf{h}}_j^{out}$  in the pass  $j$  is calculated using an IIR low-pass filter of the form

$$\Delta \tilde{\mathbf{h}}_j^{out} = \tilde{\beta} \Delta \tilde{\mathbf{h}}_{j-1}^{out} + (1 - \tilde{\beta}) (\Delta \hat{\mathbf{h}}_{j-1}^{out} - \Delta \mathbf{h}_{j-1}^{out}) \quad (5.11)$$

with the filter constant  $0 \leq \tilde{\beta} \leq 1$  and the initial value  $\Delta \tilde{\mathbf{h}}_0^{out} = \mathbf{0}$ . Clearly, an implicit assumption made in the estimation of  $\Delta \tilde{\mathbf{h}}_j^{out}$  is that the compensation of the asymmetric deflection of the mill stand is exact and therefore the estimated deviation is not influenced by the asymmetric deflection. The value of  $\tilde{\beta}$  may be used to reduce the noise on the estimated deviation  $\Delta \tilde{\mathbf{h}}_j^{out}$  as not only the actual deviation  $(\Delta \hat{\mathbf{h}}_{j-1}^{out} - \Delta \mathbf{h}_{j-1}^{out})$  but deviations from previous passes are also influencing the estimation. Clearly,  $\tilde{\beta} \approx 1$  yields in an almost constant deviation over several passes whereas  $\tilde{\beta} = 0$  does not take previous deviations into account. The result of the optimization problem (5.7) is supplemented by a compensation term for the estimated deviation  $\Delta \tilde{\mathbf{h}}_j^{out}$  and the compensation of the asymmetric mill stand deflection  $\Delta h_{comp}^{rg}$  from (5.10). The required asymmetry of the rolling gap cylinders  $\Delta \mathbf{h}_{req,j}^{rg}$  is thus computed in the form

$$\Delta \mathbf{h}_{req,j}^{rg} = \frac{w_{cyl}}{w} \Delta \mathbf{h}_{req,j}^{out} = \frac{w_{cyl}}{w} (\Delta \mathbf{h}_j^{out} - \Delta \tilde{\mathbf{h}}_j^{out}) + \Delta \mathbf{h}_{comp}^{rg} \quad (5.12)$$

with  $\Delta \mathbf{h}_{comp}^{rg} = [1 \ \dots \ 1]^T \Delta h_{comp}^{rg}$ . The values  $\Delta \mathbf{h}_{req,j}^{rg}$  are sent to the automation system of the rolling mill before the rolling pass  $j$ . Hence, the desired rolling forces  $F_{roll,des}$  are used in the compensation approach of the asymmetric mill stand deflection, i. e.,  $F_{roll} = F_{roll,des}$ . Fig. 5.5 shows the necessary calculations for the single pass-to-pass adjustment in graphical form after pass  $j - 1$ , i. e. how to calculate the required asymmetry  $\Delta \mathbf{h}_{req,j}^{rg}$  of the rolling gap cylinders for pass  $j$ .

Note that only a measurement of the downstream contour is necessary in the presented approach. This is because the centerline  $\delta_{j-2}^{out}$  of the downstream measurement of the preceding pass  $j - 2$  is used instead of the upstream centerline  $\delta_{j-1}^{in}$  to estimate the output thickness asymmetry of pass  $j - 1$ .

## 5.2 Feedback control during the rolling pass

A non-ideal control of the rolling gap actuators, model-plant mismatches or disturbances may lead to a deviation between the desired and the actual plate contour even if feedforward control is used. Hence, an additional feedback controller is used to (further) improve the contour of the plate. Simple feedback control utilizing the directly measured contour is difficult to apply because of the inherent transport delay between the camber generation in the rolling gap and the camber measurement. To circumvent this difficulty, a control approach using the delay-free

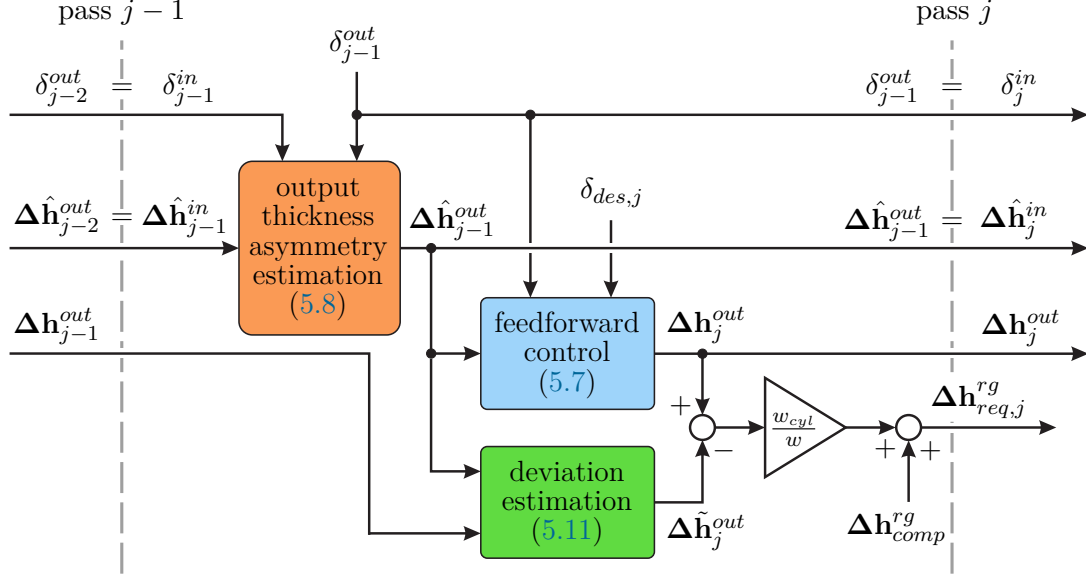


Figure 5.5: Single pass-to-pass adjustment of the rolling gap with compensation of the asymmetric mill stand deflection and the estimated deviation  $\Delta \hat{\mathbf{h}}^{out}$ .

measurement of the downstream and upstream angular velocities of the plate is presented. The mathematical model of the plate movement from Chapter 4 is used in the controller design. It describes the nexus between the angular velocity and the resulting curvature of the plate.

### 5.2.1 Plant model

As a preparatory step for the feedback controller design, the idealized time-free model (4.16) is supplemented by an output equation for the measured camber and by disturbances, which may, for instance, be caused externally or by modeling errors. The inputs of the system are

$$u_1 = \Delta h^{out}, \quad u_2 = \Delta h^{in}, \quad u_3 = \Omega^{in}, \quad u_4 = (\delta^{in})''.$$

Here,  $u_1$  is a control input (tilt of the rolling mill) whereas  $u_2$ ,  $u_3$ , and  $u_4$  are externally defined known inputs. The static model (4.16) is supplemented by disturbances (process noise)  $d_1$  and  $d_2$  to get the plant model

$$x_1(X) = \Omega^{out} = \frac{1}{w \bar{h}^{out}} \underbrace{\Delta h^{out}}_{u_1(X)} - \frac{1}{w \bar{h}^{in}} \underbrace{\Delta h^{in}}_{u_2(X)} + \frac{\bar{h}^{in}}{\bar{h}^{out}} \underbrace{\Omega^{in}}_{u_3(X)} + d_1(X) \quad (5.13a)$$

$$x_2(X) = (\delta^{out})'' = \underbrace{\Omega^{out}}_{x_1(X)} - \frac{\bar{h}^{out}}{\bar{h}^{in}} \underbrace{\Omega^{in}}_{u_3(X)} + \left( \frac{\bar{h}^{out}}{\bar{h}^{in}} \right)^2 \underbrace{(\delta^{in})''}_{u_4(X)} + d_2(X). \quad (5.13b)$$

It is assumed that the contour measurement described in Chapter 2 exactly measures the respective quantities, i. e., without errors. The machine vision system measures the current values  $\bar{v}^{in}$ ,  $\bar{v}^{out}$ ,  $\omega^{in}$ , and  $\omega^{out}$  as well as  $\delta''(\xi)$  for those parts of the plate that are currently inside the fields of view of the cameras. Therefore, the current (upstream) value  $u_4(X) = (\delta^{in})''$  is also known from images previously captured by the upstream camera. In contrast, a direct measurement of the current (downstream) value  $x_2(X) = (\delta^{out})''$  can only be made by the downstream camera after the plate has traveled the (constant) distance  $\xi_{cam} \geq \xi_{ml,1}$  from the rolling gap to the field of view of the downstream camera along the direction  $\xi$ . This causes a delay between the generation of the camber and its measurement. In the plant model, the camera system is represented by the output equations

$$y_1(X) = x_1(X) \quad (5.14a)$$

$$y_2(X) = x_2(X - (\xi_{cam} + \tilde{\xi}_{cam})). \quad (5.14b)$$

Here,  $\xi_{cam}$  is the known nominal distance, and  $\tilde{\xi}_{cam}$  is the unknown uncertainty of the distance. It is assumed that  $\xi_{cam}$  and  $\tilde{\xi}_{cam}$  are constant. Because of the unknown disturbances  $d_1$  and  $d_2$  in the (static) process model (5.13), there is no need to consider extra measurement noise in (5.14). The output  $y_1(X)$  is computed in the measurement system based on (4.15b) using the measured current values  $\bar{v}^{out}$  and  $\omega^{out}$ .

Note that the process model (5.13) is a static mapping. The only dynamical behavior of the plant model is the delay in the output equation (5.14b).

### 5.2.2 Camber control

The model (5.13) and (5.14) serves as a basis for the controller design and is rewritten in the compact form

$$x_1(X) = (A_1 + \tilde{A}_1)u_1(X) + (A_2 + \tilde{A}_2)u_2(X) + \frac{1}{A_3 + \tilde{A}_3}u_3(X) + d_1(X) \quad (5.15a)$$

$$x_2(X) = x_1(X) - (A_3 + \tilde{A}_3)u_3(X) + (A_3 + \tilde{A}_3)^2u_4(X) + d_2(X) \quad (5.15b)$$

$$y_1(X) = x_1(X) \quad (5.15c)$$

$$y_2(X) = x_2(X - (\xi_{cam} + \tilde{\xi}_{cam})), \quad (5.15d)$$

where the coefficients

$$A_1 + \tilde{A}_1 = \frac{1}{w\bar{h}^{out}} \quad (5.16a)$$

$$A_2 + \tilde{A}_2 = -\frac{1}{w\bar{h}^{in}} \quad (5.16b)$$

$$A_3 + \tilde{A}_3 = \frac{\bar{h}^{out}}{\bar{h}^{in}} \quad (5.16c)$$

are assumed to be constant.  $A_i + \tilde{A}_i$  represents the unknown true value of the respective coefficient and  $A_i$  is its known nominal counterpart used for all computations. Constancy of these values is a reasonable assumption if  $\bar{h}^{in}$  is constant and if the thickness controller ensures  $\bar{h}^{out}$  to be constant. This assumption is not necessary for practical control implementation but will simplify the proof of the closed-loop stability. The constants  $\tilde{A}_1$ ,  $\tilde{A}_2$ ,  $\tilde{A}_3$ , and  $\tilde{\xi}_{cam}$  capture the model-plant mismatch and satisfy  $|\tilde{A}_1| \ll A_1$ ,  $|\tilde{A}_2| \ll A_2$ ,  $|\tilde{A}_3| \ll A_3$ , and  $|\tilde{\xi}_{cam}| \ll \xi_{cam}$ . They will be of interest in an analysis of the robustness of the controller and are set to zero in the nominal model.

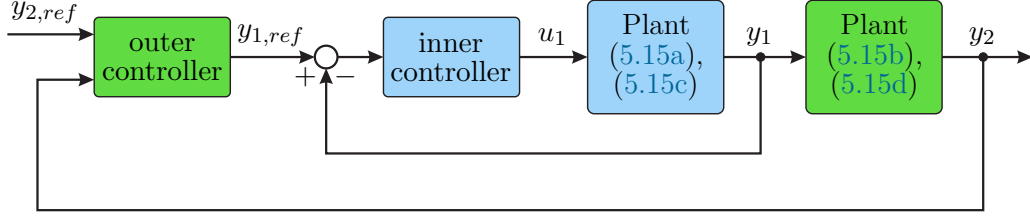


Figure 5.6: Cascade structure of the feedback controller.

Fig. 5.6 shows the proposed cascade control structure with two loops. The inner loop controls  $y_1 = \Omega^{out}$  with the control input  $u_1 = \Delta h^{out}$ , whereas the outer loop uses the control input  $y_{1,ref}$  to make  $y_2 = (\delta^{out})''$  follow  $y_{2,ref}$ . As usual for cascade control structures, the inner control loop is assumed to be ideal for the design of the outer control loop.

### 5.2.2.1 Inner loop

The inner control loop, which controls the plant (5.15a) and (5.15c), is outlined in Fig. 5.7. The control law is formulated as

$$u_1 = u_{1,ff}(X) + u_{1,fb}(X)$$

where the feedforward part  $u_{1,ff}(X)$  is calculated according to the optimization-based feedforward approach (cf. (5.12)). Note that the control input  $u_1$  (output asymmetry of the plate) is defined at the plate width  $w$  and hence has to be scaled by the factor  $\frac{w_{cyl}}{w}$  before it is sent to the automation system of the rolling gap height controller. The feedforward part  $u_{1,ff}(X)$  of the asymmetry is computed by linear interpolation in the form

$$u_{1,ff}(X) = \frac{w}{w_{cyl}} \left[ \Delta h_{req,i}^{rg} + \frac{\Delta h_{req,i+1}^{rg} - \Delta h_{req,i}^{rg}}{x_{i+1} - x_i} \left( \left( \frac{l_{des}}{2} - X \right) \chi \frac{\bar{h}^{out}}{\bar{h}^{in}} - x_i \right) \right]$$

$$\forall x_i \leq \left( \frac{l_{des}}{2} - X \right) \chi \frac{\bar{h}^{out}}{\bar{h}^{in}} \leq x_{i+1}$$

with the grid points  $x_i, i = 1, \dots, N_P$ . The feedback part

$$u_{1,fb}(X) = \frac{V_I}{A_1} T_I (y_{1,ref}(X) - y_1(X)) + \frac{V_I}{A_1} \int_0^X y_{1,ref}(\bar{X}) - y_1(\bar{X}) d\bar{X} \quad (5.17)$$

defines the PI-feedback controller  $C_I$  with the controller parameters  $V_I$  and  $T_I$ . The thickness asymmetry of the feedforward approach is defined in a coordinate system fixed to the center of the plate before the rolling pass (cf. Chapter 3). The term  $\left(\frac{l_{des}}{2} - X\right) \chi \frac{h^{out}}{h^{in}}$  with  $\chi \in \{-1, 1\}$  maps the already rolled plate length  $X$  to the coordinate  $x$  in the plate-fixed coordinate system. The desired plate length after the pass is denoted by  $l_{des}$ . A rolling pass in backward direction is characterized by  $\chi = -1$  and a rolling pass in forward direction by  $\chi = 1$ . In the

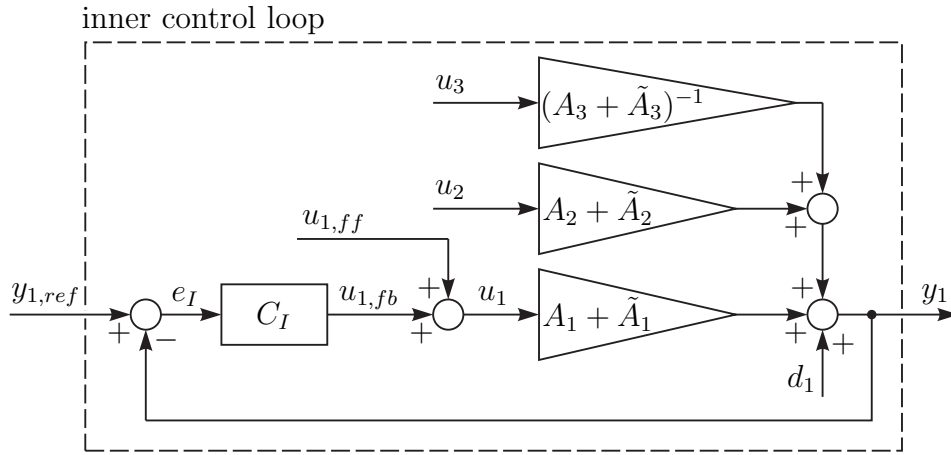


Figure 5.7: Inner control loop.

following, a hat  $\hat{\cdot}$  labels signals in the Laplace domain and  $s \in \mathbb{C}$  is the Laplace variable with the unit 1/m. The transfer function of the PI-feedback controller is

$$C_I(s) = \frac{V_I}{A_1} \frac{1 + sT_I}{s}. \quad (5.18)$$

In the Laplace domain, the input-output relation defined by (5.15a) and (5.15c) reads as

$$\hat{y}_1(s) = (A_1 + \tilde{A}_1)\hat{u}_1(s) + (A_2 + \tilde{A}_2)\hat{u}_2(s) + \frac{1}{A_3 + \tilde{A}_3}\hat{u}_3(s) + \hat{d}_1(s)$$

and the tracking error (closed-loop control error) follows in the form

$$\begin{aligned} \hat{e}_I(s) &= \hat{y}_{1,ref}(s) - \hat{y}_1(s) \\ &= \frac{\hat{y}_{1,ref}(s) - (A_1 + \tilde{A}_1)\hat{u}_{1,ff}(s) - (A_2 + \tilde{A}_2)\hat{u}_2(s) - \frac{1}{A_3 + \tilde{A}_3}\hat{u}_3(s) - \hat{d}_1(s)}{1 + (A_1 + \tilde{A}_1)C_I(s)}. \end{aligned} \quad (5.19)$$

For closed-loop stability, the denominator of (5.19) must be Hurwitz. Insertion of (5.18) into (5.19) shows that this is satisfied if  $V_I > 0$  and  $V_I T_I > -A_1/(A_1 + \tilde{A}_1) \approx -1$ . The scaling  $1/A_1$  in the control law (5.17) results in a closed-loop dynamics independent of  $w$  and  $\bar{h}^{out}$  for  $\tilde{A}_1 = 0$ . This property simplifies the choice of the controller parameters  $V_I$  and  $T_I$  as they do not have to be adjusted to plates with different dimensions. The final value theorem shows that

$$\lim_{X \rightarrow \infty} e_I(X) = \lim_{s \rightarrow 0} s \hat{e}_I(s) = 0$$

holds for constant inputs  $y_{1,ref}$ ,  $u_{1,ff}$ ,  $u_2$ ,  $u_3$ , and  $d_1$ , i. e., the steady-state error vanishes in this case.

### 5.2.2.2 Outer loop

The outer control loop, which controls the plant (5.15b) and (5.15d), is shown in Fig. 5.8. Here, a 2-DOF Smith-predictor control structure, i. e., a combination of a feedforward controller and a feedback Smith-predictor controller is used, see, e. g., [48] and [49]. For the design and the analysis of robust stability of this loop, the inner loop is assumed to be ideal, which means  $y_1 = y_{1,ref}$ . The control law

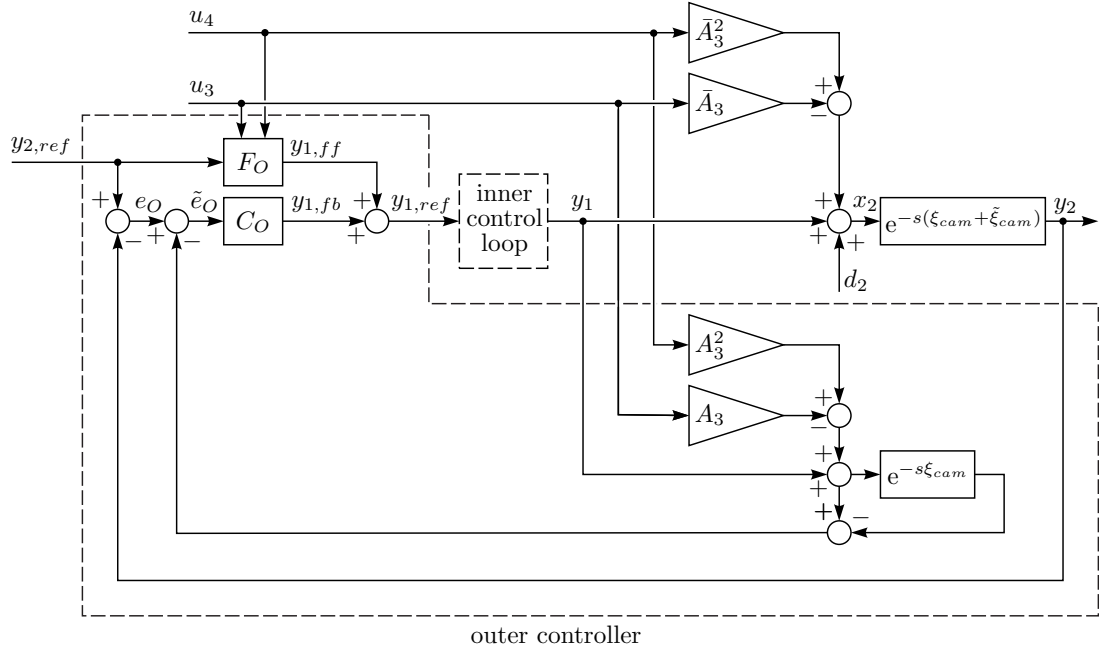


Figure 5.8: Outer control loop.

$$y_{1,ref}(X) = y_{1,ff}(X) + y_{1,fb}(X)$$

with the feedforward controller  $F_O$  defined by

$$y_{1,ff}(X) = y_{2,ref}(X + \xi_{cam}) + A_3 u_3(X) - A_3^2 u_4(X) \quad (5.20)$$

and the PI-feedback controller defined by

$$y_{1,fb}(X) = V_O T_O \tilde{e}_O(X) + V_O \int_0^X \tilde{e}_O(\bar{X}) d\bar{X}$$

is used for the outer control loop. The control law (5.20) of the feedforward controller follows from (5.15b)-(5.15d) with  $d_2 = 0$ ,  $\tilde{\xi}_{cam} = 0$ , and  $\tilde{A}_3 = 0$ . The PI-feedback controller of the outer control loop with the parameters  $T_O$  and  $V_O$  reads as

$$C_O(s) = V_O \frac{1 + sT_O}{s}. \quad (5.21)$$

As usual for a Smith-predictor, the input of the feedback controller is defined in the form

$$\begin{aligned} \tilde{e}_O(X) = & y_{2,ref}(X) - y_2(X) - \left( y_1(X) - A_3 u_3(X) + A_3^2 u_4(X) \right. \\ & \left. - y_1(X - \xi_{cam}) + A_3 u_3(X - \xi_{cam}) - A_3^2 u_4(X - \xi_{cam}) \right), \end{aligned}$$

where  $y_1(X) - A_3 u_3(X) + A_3^2 u_4(X)$  is the internal model prediction of  $x_2(X)$  (cf. (5.15b)).

In the Laplace domain, the input-output relation defined by (5.15b) and (5.15d) reads as

$$\hat{y}_2(s) = \left( \hat{y}_1(s) - \bar{A}_3 \hat{u}_3(s) + \bar{A}_3^2 \hat{u}_4(s) + \hat{d}_2(s) \right) e^{-s\bar{\xi}_{cam}}$$

with  $\bar{\xi}_{cam} = \xi_{cam} + \tilde{\xi}_{cam}$  and  $\bar{A}_3 = A_3 + \tilde{A}_3$ . The closed-loop transfer function relevant for internal stability can be written utilizing Fig. 5.8, (5.20), and (5.21) in the form

$$\begin{bmatrix} \hat{y}_{1,ref}(s) \\ \hat{y}_2(s) \end{bmatrix} = \mathbf{T}(s) \begin{bmatrix} \hat{y}_{2,ref}(s) \\ \hat{d}_2(s) \\ \hat{u}_3(s) \\ \hat{u}_4(s) \end{bmatrix} \quad (5.22)$$

with the matrix

$$\begin{aligned} \mathbf{T}(s) &= \frac{1}{1 + L(s)} \mathbf{N}(s) \\ &= \frac{1}{1 + C_O(s) \left( 1 + e^{-s\bar{\xi}_{cam}} - e^{-s\xi_{cam}} \right)} \\ &\quad \begin{bmatrix} N_{11}(s) & N_{12}(s) & N_{13}(s) & N_{14}(s) \\ N_{21}(s) & N_{22}(s) & N_{23}(s) & N_{24}(s) \end{bmatrix} \end{aligned} \quad (5.23)$$

and the abbreviations

$$\begin{aligned}
N_{11}(s) &= C_O(s) + e^{s\xi_{cam}} \\
N_{12}(s) &= -C_O(s)e^{-s\bar{\xi}_{cam}} \\
N_{13}(s) &= A_3 + C_O(s) \left( \bar{A}_3 e^{-s\bar{\xi}_{cam}} + A_3(1 - e^{-s\xi_{cam}}) \right) \\
N_{14}(s) &= -A_3^2 - C_O(s) \left( \bar{A}_3^2 e^{-s\bar{\xi}_{cam}} + A_3^2(1 - e^{-s\xi_{cam}}) \right) \\
N_{21}(s) &= \left( C_O(s) + e^{s\xi_{cam}} \right) e^{-s\bar{\xi}_{cam}} \\
N_{22}(s) &= \left( 1 + C_O(s)(1 - e^{-s\xi_{cam}}) \right) e^{-s\bar{\xi}_{cam}} \\
N_{23}(s) &= -\tilde{A}_3 N_{22}(s) \\
N_{24}(s) &= \tilde{A}_3(2A_3 + \tilde{A}_3)N_{22}(s).
\end{aligned}$$

Without any model-plant mismatch and with an exactly known position of the curvature measurement, i. e.  $\tilde{A}_3 = 0$  and  $\tilde{\xi}_{cam} = 0$ , satisfying  $V_O > 0$  and  $V_O T_O > -1$  ensures the BIBO stability of (5.22) and thus internal stability of the system.  $V_O > 0$  and  $V_O T_O > -1$  are assumed throughout this chapter.

In general, the position of the curvature measurement is uncertain, i. e.,  $\tilde{\xi}_{cam} \neq 0$ . The control loop is rearranged as shown in Fig. 5.9 for the test of internal stability. The task of proving internal stability is to show that the transfer functions between every input/output combination in the closed-loop system of the signals shown in Fig. 5.9 are BIBO-stable. The signal  $y_{1,ff}$  can be shifted and added to  $u_I$  and  $u_O$ . Furthermore, the signals  $u_I$  and  $u_O$  can be shifted behind the transfer function blocks  $1 - e^{-s\xi_{cam}}$  and  $e^{-s(\xi_{cam} + \tilde{\xi}_{cam})}$ , respectively, because these two transfer functions are BIBO-stable. Hence, the effect of  $u_I$  and  $u_O$  is equivalent to that of  $y_{2,ref}$ . Consequently,  $y_{1,ff}$ ,  $u_I$ , and  $u_O$  are not relevant for the stability analysis and are set to zero, i. e.,  $y_{1,ff} = u_I = u_O = 0$  and it is sufficient to show the stability of the control loop with the reference value  $y_{2,ref}$  as input and  $y_2$  as output.

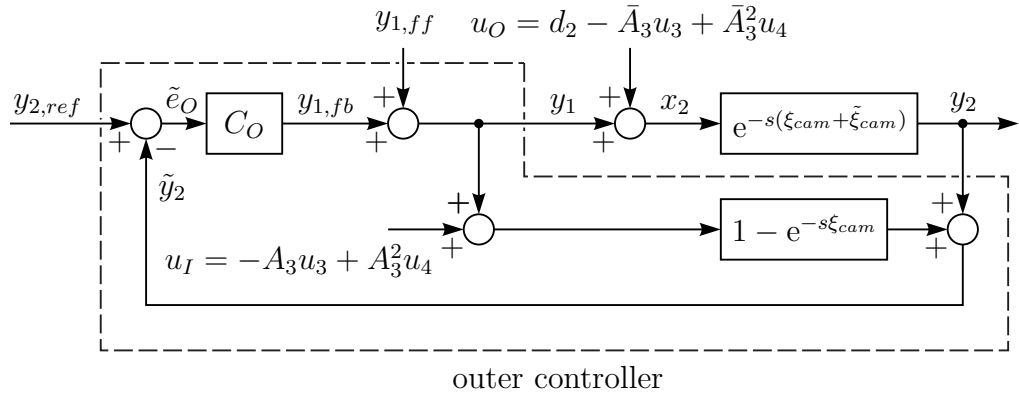


Figure 5.9: Proof of robust stability of the outer control loop.



However, it is easier to show the stability for the reference value  $y_{2,ref}$  as input and  $\tilde{y}_2$  as output because this input/output combination results in a SISO feedback control loop with  $L(s)$  in the forward branch and gain 1 in the feedback branch. Proving the stability for  $\tilde{y}_2$  is sufficient because when  $\tilde{y}_2$  is bounded also  $y_2$  is bounded. The test for internal stability is to analyze whether  $\frac{1}{1+L(s)} \in \hat{\mathcal{A}}$ , see [50], for all admissible values of  $\tilde{\xi}_{cam}$ , where  $\hat{\mathcal{A}}$  is the set of Laplace transforms of BIBO-stable impulse responses as defined in [50] or [51]. A Nyquist-like graphical stability test, see, e. g., [51], is used for this analysis which consists of two parts:

First, it must be shown that  $L(s)$  can be written in the form

$$L(s) = L_a(s) + L_r(s),$$

where  $L_a(s) \in \hat{\mathcal{A}}$  and  $L_r(s)$  is rational and strictly proper. Insertion of (5.21) into  $L(s)$  from (5.23) yields, see also Fig. 5.9,

$$L(s) = \underbrace{\left(\frac{V_O}{s}\right)}_{L_r(s) \text{ rational and strictly proper}} + \underbrace{V_O T_O \left(1 - e^{-s\tilde{\xi}_{cam}}(1 - e^{-s\tilde{\xi}_{cam}})\right) - \frac{V_O}{s} e^{-s\tilde{\xi}_{cam}} \left(1 - e^{-s\tilde{\xi}_{cam}}\right)}_{L_a(s) \in \hat{\mathcal{A}}}. \quad (5.24)$$

Second,  $1+L(s)$  has to be analyzed. Suppose that  $L(s)$  has  $p$  poles in  $\mathbb{C}_0^+$ . Here,  $\mathbb{C}_0^+$  denotes the right half of the complex plane, i. e.  $\mathbb{C}_0^+ = \{s \in \mathbb{C} : \Re\{s\} > 0\}$ , with  $\Re\{\cdot\}$  denoting the real part. Let  $\bar{N}_\infty$  be the so-called *Nyquist contour*, which is the semi-circle contour encompassing  $\mathbb{C}_0^+$  in the clockwise sense. This semi-circle has an infinite radius and its straight section is generally the  $j\omega$ -axis (imaginary axis). However, if  $L(s)$  features poles on the  $j\omega$ -axis, small *detours* around these poles have to be made. These detours are small semi-circles in the counterclockwise direction around these poles (so that the detours are in  $\mathbb{C}_0^+$ ). The radius of the detours is infinitesimally small, meaning that they do not exclude any relevant part of  $\mathbb{C}_0^+$ . Based on these definitions, the second part of the graphical stability test requires that

$$1 + L(s) \neq 0 \quad \forall s \in \bar{N}_\infty$$

and that  $1 + L(s)|_{s \in \bar{N}_\infty}$  encircles the origin ( $s = 0$ )  $p$  times in the counterclockwise sense.

From (5.24), it follows that  $p = 0$ . Therefore,

$$\Re\{1 + L(s)\} > 0 \quad \forall s \in \bar{N}_\infty \quad (5.25)$$

implies that the second part of the above graphical stability test is satisfied. Because (5.25) is sufficient but generally not necessary for the second part of

the graphical stability test, (5.25) may yield an overly conservative (yet safe) approximation of the true stability region. However, for the proposed outer loop, (5.25) is a tractable stability test.

The following statement is shown in Appendix C. For satisfaction of (5.25) with  $L(s)$  from (5.23) it is sufficient (though not necessary) that  $V_O > 0$ ,  $T_O > 0$ , and

$$\frac{1}{V_O} + T_O > \underbrace{2 \left| \sin \left( \omega \frac{\tilde{\xi}_{cam}}{2} \right) \right| \sqrt{T_O^2 + \frac{1}{\omega^2}}}_{rhs(\omega)} \quad \forall \omega \in \mathbb{R}.$$

The global maximum of  $rhs(\omega)$  occurs, see Appendix C, at the point

$$\omega = \begin{cases} 0 & \text{if } T_O \leq \frac{|\tilde{\xi}_{cam}|}{2\sqrt{3}} \\ \pm\omega^* & \text{otherwise} \end{cases},$$

where  $\omega^*$  is the smallest strictly positive solution of

$$0 = \left( \frac{\tilde{\xi}_{cam}\omega^*}{2} \right)^3 \left( \frac{2T_O}{\tilde{\xi}_{cam}} \right)^2 + \frac{\tilde{\xi}_{cam}\omega^*}{2} - \tan \left( \frac{\tilde{\xi}_{cam}\omega^*}{2} \right).$$

The values  $\omega^*$  and  $rhs(\omega)$  have to be numerically computed whereas  $rhs(0) = |\tilde{\xi}_{cam}|$ . These results show which conditions the tuning parameters  $V_O$  and  $T_O$  have to satisfy for robust closed-loop stability and conclude the stability analysis.

From (5.22), the tracking error of the outer loop follows in the form

$$\hat{e}_O(s) = \hat{y}_{2,ref}(s) - \hat{y}_2(s) = \frac{1}{1 + L(s)} \mathbf{E}(s) \begin{bmatrix} \hat{y}_{2,ref}(s) \\ \hat{d}_2(s) \\ \hat{u}_3(s) \\ \hat{u}_4(s) \end{bmatrix}$$

with the abbreviation

$$\mathbf{E}(s) = \begin{bmatrix} 1 - e^{-s\tilde{\xi}_{cam}} + C_O(s)(1 - e^{-s\xi_{cam}}) \\ (C_O(s)(e^{-s\xi_{cam}} - 1) - 1) e^{-s\tilde{\xi}_{cam}} \\ -\tilde{A}_3 (C_O(s)(e^{-s\xi_{cam}} - 1) - 1) e^{-s\tilde{\xi}_{cam}} \\ \tilde{A}_3 (2A_3 + \tilde{A}_3) (C_O(s)(e^{-s\xi_{cam}} - 1) - 1) e^{-s\tilde{\xi}_{cam}} \end{bmatrix}^T.$$

Using the final value theorem, it follows that

$$\lim_{X \rightarrow \infty} e_O(X) = \lim_{s \rightarrow 0} s \hat{e}_O(s) = 0$$

for constant inputs  $y_{2,ref}$ ,  $d_2$ ,  $u_3$ , and  $u_4$ , i. e.,  $\hat{y}_{2,ref}(s) = \frac{1}{s}\alpha_0$ ,  $\hat{d}_2(s) = \frac{1}{s}\alpha_1$ ,  $\hat{u}_3(s) = \frac{1}{s}\alpha_2$ , and  $\hat{u}_4(s) = \frac{1}{s}\alpha_3$  with arbitrary constants  $\alpha_i \in \mathbb{R}$ ,  $i = 0, 1, 2, 3$ . The steady-state error vanishes in this case.

### 5.2.3 Implementation

The discussed feedback control laws are parameterized as functions of the processed plate length  $X$ . However, the angular and longitudinal velocities as well as the curvature of the plate are measured with a fixed sampling time  $T_{s,fb}$ . This is why the controllers are implemented in a discrete-time form. Assuming piecewise constant inputs and using the Euler-forward integration scheme for a sampling period  $kT_{s,fb} \leq t < (k+1)T_{s,fb}$ , the PI-feedback control law of the inner loop at  $t = kT_{s,fb}$  follows in the form

$$u_{1,fb}(kT_{s,fb}) = \frac{V_I}{A_1} T_I (y_{1,ref}(kT_{s,fb}) - y_1(kT_{s,fb})) + \frac{V_I}{A_1} x_{I,k}, \quad (5.26)$$

with the update of the discrete-time integrator state

$$x_{I,k+1} = x_{I,k} + \bar{v}^{out}(kT_{s,fb}) T_{s,fb} (y_{1,ref}(kT_{s,fb}) - y_1(kT_{s,fb})).$$

The spatial increment  $X_{k+1} - X_k = \bar{v}^{out}(kT_{s,fb}) T_{s,fb}$  follows directly from (4.14). By analogy, the PI control law for the outer loop reads as

$$y_{1,fb}(kT_{s,fb}) = V_O T_O \tilde{e}_O(kT_{s,fb}) + V_O x_{O,k}, \quad (5.27)$$

with the update of the discrete-time integrator state

$$x_{O,k+1} = x_{O,k} + \bar{v}^{out}(kT_{s,fb}) T_{s,fb} \tilde{e}_O(kT_{s,fb}).$$

The initial states of the integrators are set to  $x_{I,0} = x_{O,0} = 0$ .

The feedback part  $u_{1,fb}$  of the inner control loop is limited to  $u_{1,min} \leq u_{1,fb} \leq u_{1,max}$  to avoid an excessive (additional) asymmetry of the output thickness of the plate. In combination with the integrators used in the feedback controllers, such a constraint of the control input can lead to a windup behavior of the controller, which is associated with a deterioration of the control performance. This is why a simple anti-windup mechanism is added to the control laws (5.26) and (5.27). The integrator state  $x_{I,k}$  is only updated if one of the conditions

$$\begin{aligned} u_{1,min} &< u_{1,fb}(kT_{s,fb}) < u_{1,max} \\ u_{1,fb}(kT_{s,fb}) &\leq u_{1,min} \wedge y_{1,ref}(kT_{s,fb}) > y_1(kT_{s,fb}) \\ u_{1,fb}(kT_{s,fb}) &\geq u_{1,max} \wedge y_{1,ref}(kT_{s,fb}) < y_1(kT_{s,fb}) \end{aligned}$$

is fulfilled. Analogously, the integrator state  $x_{O,k}$  is only updated for

$$\begin{aligned} u_{1,min} &< u_{1,fb}(kT_{s,fb}) < u_{1,max} \\ u_{1,fb}(kT_{s,fb}) &\leq u_{1,min} \wedge \tilde{e}_O(kT_{s,fb}) > 0 \\ u_{1,fb}(kT_{s,fb}) &\geq u_{1,max} \wedge \tilde{e}_O(kT_{s,fb}) < 0. \end{aligned}$$

Otherwise, the integrator states are held constant.

### 5.3 Multi-pass adjustment of the rolling gap

All methods of camber control presented so far are only utilizing the asymmetry of the plate thickness during the actual or the subsequent rolling pass. These single-pass-based approaches may indeed lead to the desired plate contour at the end of the rolling process. However, they can entail a non-homogeneous thickness profile of the final product. This drawback may be avoided by using a multi-pass approach utilizing the asymmetry of the thickness in several rolling passes. The result of this approach is a rolling schedule containing the desired curvature and the desired thickness asymmetry for the considered passes. Another application of the multi-pass approach is the production of annular sectors (a specifically cambered plate) with a homogeneous thickness profile, which are then bent to form a truncated cone. To this end, the multi-pass approach is used to determine the necessary rolling schedule yielding the desired contour and thickness profile after the last pass.

#### 5.3.1 Formulation of the optimization problem

As indicated in Fig. 5.10, the thickness asymmetry and the centerline before the first considered pass (pass 1) are assumed to be known. In the following  $N_{rp} - 1$  passes, the asymmetry of the plate thickness is adjusted to obtain the desired final plate contour defined by  $\delta_{pred,N_{rp}}^{out}$  and a homogeneous plate thickness after the last rolling pass, i. e.,  $\Delta \mathbf{h}_{N_{rp}}^{out} = \mathbf{0}$ .

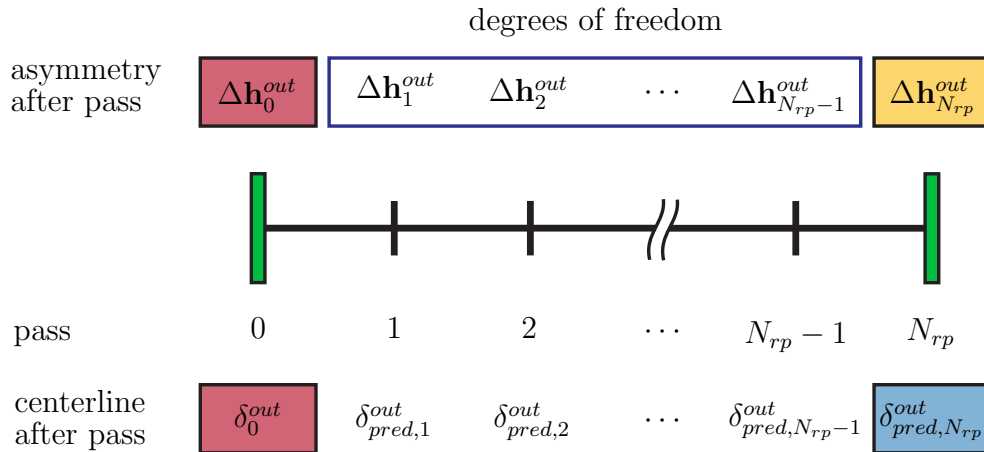


Figure 5.10: Schematic of the multi-pass approach to obtain the desired plate contour and a homogeneous thickness of the final product.

The output asymmetries  $\Delta h_{i,q}^{out}$  in every pass  $q = 1, \dots, N_{rp} - 1$  defined on an equally spaced grid  $x_{i,q}$ ,  $i = 1, \dots, N_P$  are summarized in the matrix  $\Delta \mathbf{H}^{out}$  in

the form

$$\Delta \mathbf{H}^{out} = \begin{bmatrix} \Delta \mathbf{h}_1^{out} & \Delta \mathbf{h}_2^{out} & \dots & \Delta \mathbf{h}_{N_{rp}-1}^{out} \end{bmatrix}.$$

$\Delta \mathbf{H}^{out}$  is determined by solving the optimization problem

$$\Delta \mathbf{H}^{out} \in \mathbb{R}^{N_P \times N_{rp}-1} \min J(\Delta \mathbf{H}^{out}) \quad (5.28)$$

with the objective function

$$\begin{aligned} J(\Delta \mathbf{H}^{out}) &= \frac{1}{M_{CL}} \sum_{j=1}^{M_{CL}} \left( (\delta_{des}(\bar{x}_{j,N_{rp}}))'' - (\delta_{pred,N_{rp}}^{out}(\bar{x}_{j,N_{rp}}))'' \right)^2 \\ &+ \frac{\tilde{\beta}_1}{N_P(N_{rp}-1)} \sum_{q=1}^{N_{rp}-1} (\Delta \mathbf{h}_q^{out})^T \Delta \mathbf{h}_q^{out} \\ &+ \frac{\tilde{\beta}_2}{(N_P-1)(N_{rp}-1)} \sum_{i=1}^{N_P-1} \sum_{q=1}^{N_{rp}-1} \left( \frac{\Delta h_{i+1,q}^{out} - \Delta h_{i,q}^{out}}{x_{i+1,q} - x_{i,q}} \right)^2 \\ &+ \frac{\tilde{\beta}_3}{N_P(N_{rp}-1)} \sum_{i=1}^{N_P} \sum_{q=1}^{N_{rp}-1} P(\Delta h_{i,q}^{out}) \\ &+ \frac{\tilde{\beta}_4}{M_{CL}(N_{rp}-1)} \sum_{j=1}^{M_{CL}} \sum_{q=1}^{N_{rp}-1} \left( (\delta_{pred,q}^{out}(\bar{x}_{j,q}))'' \right)^2. \end{aligned}$$

Here, the desired centerline is denoted by  $\delta_{des}(x)$  and  $M_{CL}$  is the number of values used for evaluating the final curvature deviation  $(\delta_{des}(x))'' - (\delta_{pred,N_{rp}}^{out}(x))''$  on an equally spaced grid  $\bar{x}_{j,N_{rp}}$ ,  $j = 1, \dots, M_{CL}$ . The weighting factors  $\tilde{\beta}_i$ ,  $i = 1, \dots, 3$ , have a similar influence on the optimization result as their counterparts  $\beta_i$  in the single pass optimization (5.7). The term  $\tilde{\beta}_4/M_{CL}(N_{rp}-1) \sum_{j=1}^{M_{CL}} \sum_{q=1}^{N_{rp}-1} \left( (\delta_{pred,q}^{out}(\bar{x}_{j,q}))'' \right)^2$  with the weighting factor  $\tilde{\beta}_4$  is added to the objective function to avoid too large curvatures of the centerline in the interim passes. The optimization problem (5.28) is solved similarly to the optimization problem (5.7) of the single pass approach. The same termination criteria as for the single pass-to-pass optimization in Section 5.1.3 are used in the numerical solution of (5.28).

### 5.3.2 Rolling of annular sectors

The multi-pass approach can be used for the production of annular sectors. Typically they are then bent to truncated cones (cf. Fig. 5.11a), which are used, e. g., for the pylons of wind turbines. In the standard production process, an annular sector is cut out from a rectangular plate (cf. Fig. 5.11b). Clearly, this approach entails significant amounts of waste (scrap), which has to be recycled.

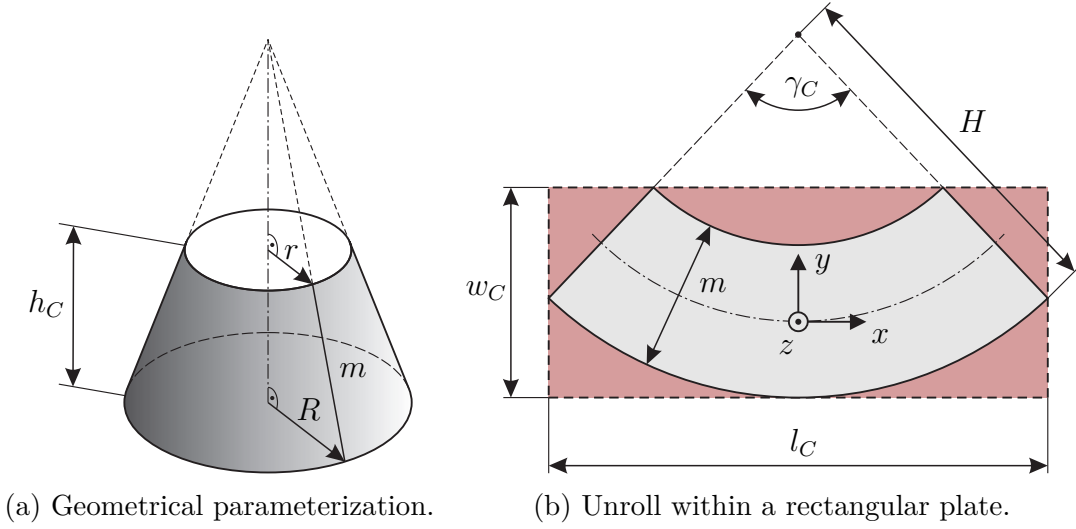


Figure 5.11: Basic and final geometry of a truncated cone.

Hence there is potential to reduce scrap by rolling annular sectors (plates with intentional camber).

In the following section, the multi-pass approach is used to create a rolling schedule which produces annular sectors with zero thickness asymmetry in several rolling passes. As shown in Fig. 5.11a, the truncated cone may be parameterized by the height  $h_C$  and the radii of the bottom and the top surface  $R$  and  $r$ , respectively. Another common parameter set to describe a cone is given by the outer radius  $R$ , the height  $h_C$  and the taper of the cone  $k_C = 2\frac{R-r}{h_C}$ .

As shown in Fig. 5.11b, the corresponding annular sector has the width  $m = \sqrt{h_C^2 + (R-r)^2}$ , the outer radius  $H = \frac{Rm}{R-r}$ , and the angle  $\gamma_C = 2\pi\frac{R-r}{m}$ . If this annular sector is cut out from a rectangular plate, it must at least have the width

$$w_C = H - (H - m) \cos\left(\frac{\gamma_C}{2}\right)$$

and the length

$$l_C = 2H \sin\left(\frac{\gamma_C}{2}\right).$$

Clearly, the amount of waste produced in the standard production process depends on the actual dimensions of the annular sector. As an indicator for the potential to reduce the recycling material and therefore the production costs, the degree of material utilization  $\eta_C$  is introduced. This is the ratio between the area of the annular sector and the area of a rectangle with dimensions  $w_C$  and  $l_C$ , i. e.,

$$\eta_C = \left(H^2 - (H - m)^2\right) \frac{\gamma_C}{2l_C w_C}.$$

Fig. 5.12 shows  $\eta_C$  for two different radii  $R$  and for different values of the cone height  $h_C$  and of the cone taper  $k_C$ . The height  $h_C$  ranges from 2 m to the maximum plate width  $w_{max} = 4.7$  m that can be rolled at the considered rolling mill. However, Fig. 5.12 only shows parameter combinations where  $m \leq w_{max}$  is satisfied because wider plates cannot even be rolled with the multi-pass approach at the considered rolling mill. The figure indicates that the achievable material

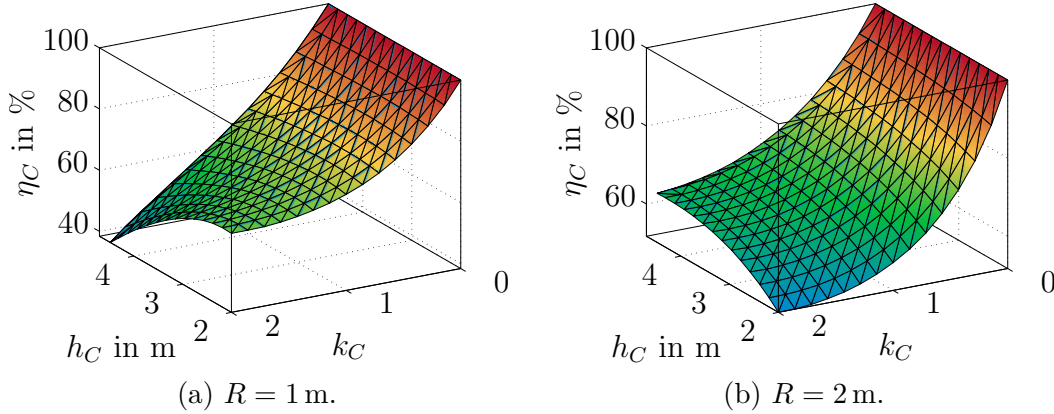


Figure 5.12: Degree of utilization  $\eta_C$  for different heights  $h_C$  and tapers  $k_C$  of a cone.

savings can be quite large if an annular sector is rolled. In this case, the multi-pass approach is used to create a rolling schedule with the desired centerline

$$\delta_{des}(x) = H - \frac{m}{2} - \sqrt{\left(H - \frac{m}{2}\right)^2 - x^2}$$

after the last pass. However, the direct rolling of annular sectors is subject to limitations. First of all, the controller of the rolling gap height has to cope with the off-center position of the plate. This entails an adaption of the subordinate rolling gap controller because in general an asymmetric deflection of the mill stand caused by the asymmetric loading of the rolling gap cylinders is not taken into account. Furthermore, the downstream plate moves sideways during the rolling pass due to the intended camber and hence it must be ensured that the plate stays on the roller table.

## 5.4 Summary

In this chapter, two approaches to reduce contour errors utilizing the contour measurement from Chapter 2 were discussed. The first one uses the mathematical model of the contour evolution to calculate the asymmetry of the output thickness required in the subsequent pass to eliminate a camber. Furthermore, an asymmetric compliance of the mill stand can be compensated based on the desired

rolling force. Moreover, using the measurement of the contour before and after the rolling pass, the resulting output asymmetry can be estimated. The difference between the estimated and the desired asymmetry is used to determine and to compensate disturbances affecting the asymmetry of the rolling gap. In the second approach, a feedback controller reduces contour errors during the current pass. Here, a delay-free measurement of the angular velocity of the plate is utilized in a 2-DOF Smith-predictor control structure. Moreover, a control strategy covering several rolling passes was discussed. This multi-pass approach may be used to determine a rolling schedule to simultaneously obtain the desired plate contour and a homogeneous thickness profile after the last pass. In the following chapter, the proposed camber reduction approaches are validated using simulations and measurement results from the considered rolling mill.



---

### Numerical results and measurements

---

In this chapter, the impact of disturbances and parameter uncertainties on the proposed approaches for the reduction of contour errors is studied by means of simulations. Furthermore, simulation results of the multi-pass adjustment for rolling of an annular sector are shown. Finally, measurements from the considered mill stand demonstrate the practical feasibility of the proposed methods.

#### 6.1 Simulation results

This section presents simulation results obtained by the proposed feedforward and feedback control strategies. The effect of changing important weighting and tuning factors is studied by means of different simulations. Furthermore, the impact of disturbances of the thickness profile and imperfections of the rolling gap actuators is investigated. Another simulation addresses the rolling of annular sectors as an application of the multi-pass approach.

##### 6.1.1 Single pass-to-pass adjustment

First, simulation results of the single-pass method to reduce the camber are shown. The evolution of the contour is predicted using the mathematical model from Chapter 3. The simulated contour is used in the optimization-based approach from Section 5.1 to determine the required output thickness profile of the next pass. Besides contour errors resulting from upstream processes (e. g. continuous casting, slab reheating process, roughing mill), generally unknown, inhomogeneous input thickness profiles are common imperfections before the first pass. Hence, an unknown asymmetric input thickness profile and a (measurable) initial contour

error at the beginning of the rolling process are used to validate the feedforward approach. In the first two simulation scenarios, ideal rolling gap actuators are assumed. Under real rolling conditions, position control of these actuators may be imperfect. Hence, the effect of deviations between the required and the actual output asymmetry is investigated in the third simulation scenario. Because the simulation model does not capture the mill stand compliance, the effect of asymmetric mill stand deflection is not considered in the simulations.

Crucial parameters affecting the result of the optimizations are the weighting factors  $\beta_i$ ,  $i = 1, \dots, 3$  and  $\hat{\beta}_i$ ,  $i = 1, \dots, 3$ . In addition to the role of  $\beta_1$  (and also of  $\hat{\beta}_1$ ) as weighting factor in the objective function, a large value of  $\beta_1$  contributes to a good-natured optimization problem due to the regularizing effect of the term  $\beta_1/N_P \sum_{i=1}^{N_P} (\Delta h_i^{out})^2$ , see, e. g., [47]. Variations of the output asymmetry in longitudinal direction are strongly penalized by setting  $\beta_2 = \hat{\beta}_2 = 10^3 \text{ m}^{-2}$ . This yields a sufficiently homogeneous asymmetry. The output asymmetry of the plate is limited to  $\Delta h_i^{out} \in [\Delta h_{min,i}^{out}, \Delta h_{max,i}^{out}]$ ,  $i = 1, \dots, N_P$ . The constant  $\beta_3$  is chosen so that violations of the constraints  $\Delta h_{min,i}^{out}$  and  $\Delta h_{max,i}^{out}$  are within an acceptable range. The constraints  $\Delta h_{min,i}^{out}$  and  $\Delta h_{max,i}^{out}$  are set according to

$$\begin{aligned}\Delta h_{min,i}^{out} &= \max(\Delta h_{min,rel}^{out} + \Delta h_i^{in}, \Delta h_{min,abs}^{out}) \\ \Delta h_{max,i}^{out} &= \min(\Delta h_{max,rel}^{out} + \Delta h_i^{in}, \Delta h_{max,abs}^{out}).\end{aligned}$$

The parameters  $\Delta h_{min,rel}^{out}$  and  $\Delta h_{max,rel}^{out}$  represent constraints relative to the asymmetry  $\Delta h^{in}$  of the input thickness of the current pass and are used to limit the change of the asymmetry from pass to pass. In contrast,  $\Delta h_{min,abs}^{out}$  and  $\Delta h_{max,abs}^{out}$  restrict the absolute value of the output asymmetry. Typically, the weighting factors of the asymmetry estimator are chosen equal to the weighting factors of the feedforward approach. However for the simulations, the estimated output asymmetry should not be subject to constraints, which is why  $\hat{\beta}_3$  is set to zero, i. e.,  $\hat{\beta}_3 = 0$ . The parameters used in the simulations are shown in Tab. 6.1.

Parameter	Value	Unit	Parameter	Value	Unit
$P_x$	20		$\hat{\beta}$	0.2	
$P_y$	4		$\Delta h_{min,rel}^{out}$	-100	$\mu\text{m}$
$N_P$	15		$\Delta h_{max,rel}^{out}$	100	$\mu\text{m}$
$N_B$	4		$\Delta h_{min,abs}^{out}$	-400	$\mu\text{m}$
$M_{CL}$	100		$\Delta h_{max,abs}^{out}$	400	$\mu\text{m}$
$\beta_1 = \hat{\beta}_1$	$10^{-1}$	$\text{m}^{-4}$	$h_{est,max}^{out}$	30	$\text{mm}$
$\beta_2 = \hat{\beta}_2$	$10^3$	$\text{m}^{-2}$	$\bar{\gamma}_x = \hat{\gamma}_x$	$10^{-7}$	$\text{m}$
$\beta_3$	$10^4$	$\text{m}^{-4}$	$\bar{\gamma}_J = \hat{\gamma}_J$	$10^{-8}$	$\text{m}^{-2}$
$\hat{\beta}_3$	0		$\bar{\gamma}_{dJ} = \hat{\gamma}_{dJ}$	$10^{-4}$	$\text{m}^{-2}$

Table 6.1: Parameters used for the simulations of the feedforward strategy.

pass	1	2	3	4	5	6
$h_{des}^{out}$ in mm	48.1	36.3	26.2	18.8	15.1	13.1

Table 6.2: Rolling schedule of the considered plate.

The choice  $\hat{\beta} = 0.2$  for the filter constant of the low-pass filter in (5.11) has proven to be useful because this selection entails only a moderate filtering of the estimated deviation  $\Delta \tilde{\mathbf{h}}^{out}$ . As discussed in Section 5.1.4, the estimation of the output asymmetry is only performed for plates with a desired output thickness smaller than  $h_{est,max}^{out}$  where the selection  $h_{est,max}^{out} = 30$  mm has proven to be useful.

A plate with the initial dimensions  $l = 6.92$  m,  $w = 2.59$  m, and  $h = 60.2$  mm is considered in the simulations. At the end of the rolling process, a final plate length of 31.7 m and a final plate thickness of 13.1 mm should be achieved. The rolling schedule of the considered plate is shown in Tab. 6.2.

### 6.1.1.1 Initial input thickness asymmetry

In the first simulation, an unknown asymmetric plate thickness ( $\Delta h^{in} = -1$  mm)

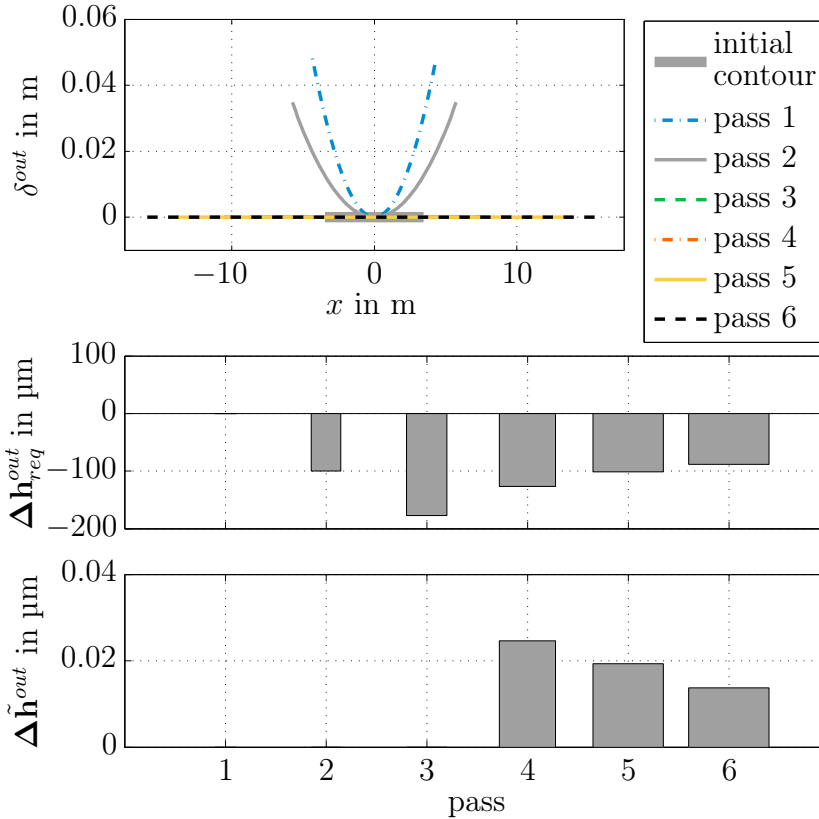


Figure 6.1: Simulation results for an unknown asymmetry of the initial thickness.

before the first rolling pass is assumed. The resulting centerline of the plate after each pass and the corresponding optimized input according to (5.12) are shown in Fig. 6.1. The width of the bars is proportional to the initial plate length in the respective pass and the height of the bars represents the value of the asymmetry at the equally spaced grid points. Due to the initial rectangular contour and the unknown input profile of the plate, no control action is performed in the first pass, i. e.  $\Delta \mathbf{h}_{req,1}^{out} = \mathbf{0}$ . This causes a cambered plate after the first pass because of the non-homogeneous deformation. Because of the constant initial asymmetry of the plate thickness, the asymmetries in Fig. 6.1 are also constant with respect to the  $x$ -coordinate. The asymmetry of the output thickness is only estimated for passes with a desired output thickness less than  $h_{est,max}^{out} = 30$  mm which is only satisfied for passes 3 to 6 (cf. Tab. 6.2). Hence, the estimated deviation  $\Delta \tilde{\mathbf{h}}^{out}$  is only available for passes 4 to 6. The assumed ideal position controller of the rolling gap actuators should lead to  $\Delta \tilde{\mathbf{h}}^{out} = \mathbf{0}$ . However, because the optimization problem to estimate the output asymmetry is only solved up to a certain numerical tolerance (cf. Section 5.1.4), a small but negligible estimated deviation  $\Delta \tilde{\mathbf{h}}^{out}$  results.

The camber is successively reduced to almost zero after the third pass and

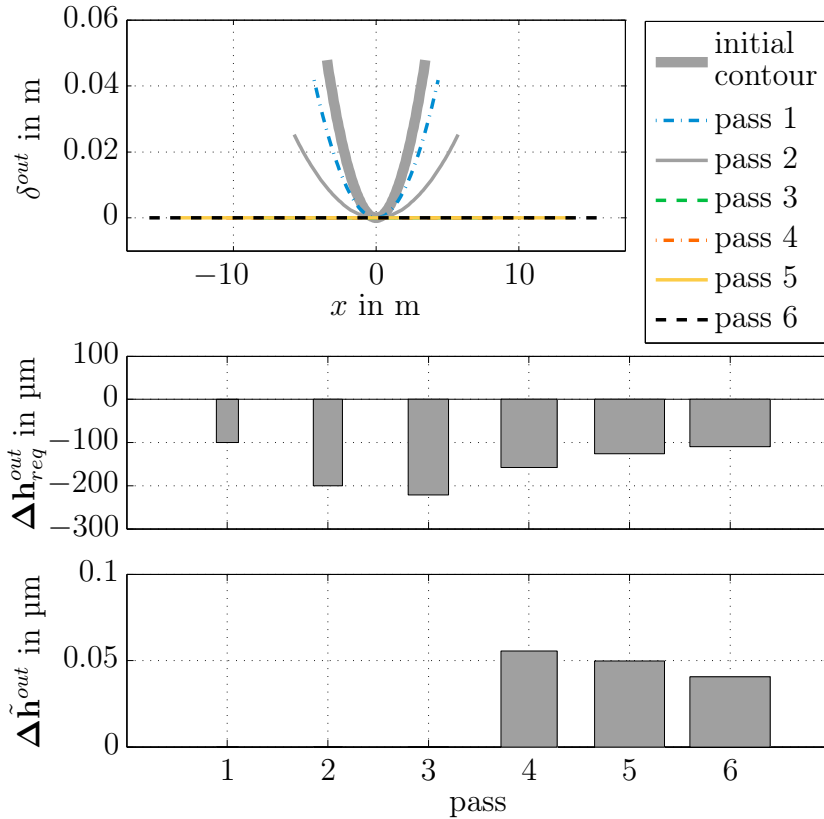


Figure 6.2: Simulation results for an initial contour error.

hence the passes 3 and 4 cannot be seen in the upper part of Fig. 6.1 because they are covered by the centerline of the passes 5 and 6. Without constraints on the output asymmetry and with  $\beta_1 = 0$ , i. e. no weighting of the asymmetry in the objective function  $J(\Delta \mathbf{h}^{out})$ , the contour error after pass 1 would be fully compensated in pass 2. An inhomogeneous thickness profile remains in the lateral direction after the last rolling pass, which is caused by the initial thickness asymmetry.

### 6.1.1.2 Initial contour error

In the second simulation study (cf. Fig. 6.2), a measurable and thus known contour error with a homogeneous thickness distribution at the beginning of the rolling process is assumed. Here, the constraint  $\Delta h_{min}^{out}$  on the asymmetry of the output thickness is active in the first two passes. Without constraints and with  $\beta_1 = 0$  the initial contour error could be fully compensated in pass 1. However, after a few passes the contour error is reduced to zero at the cost of an asymmetric thickness profile after the last rolling pass. Similar to the simulation scenario from Section 6.1.1.1,  $\Delta \tilde{\mathbf{h}}^{out}$  should be zero but the numerical method used to estimate the output asymmetry only yields  $\Delta \tilde{\mathbf{h}}^{out} \approx \mathbf{0}$ .

### 6.1.1.3 Non-ideal control of actuator positions and asymmetry disturbance

The following simulation covers both, an unknown asymmetric input thickness profile and a known camber before the first pass. Furthermore, the actual output asymmetry is considered in the form

$$\Delta \mathbf{h}_{act}^{out} = \kappa \Delta \mathbf{h}_{req}^{out} + [1 \quad \dots \quad 1]^T \Delta h_{dist}.$$

This mapping is used to simulate an erroneous behavior of the rolling gap actuators. For the following simulations, the scaling factor is chosen as  $\kappa = 0.5$  and the offset was set to  $\Delta h_{dist} = 100 \mu\text{m}$ . Even for this rather extreme simulation scenario, the camber of the plate can be successively reduced as shown in Fig. 6.3. Due to the low-pass filtering in (5.11) the estimated deviation  $\Delta \tilde{\mathbf{h}}^{out}$  increases during the rolling passes from  $0 \mu\text{m}$  to approximately  $170 \mu\text{m}$ .

Without using the estimated values  $\Delta \tilde{\mathbf{h}}^{out}$ , the results shown in Fig. 6.4 are obtained. Fig. 6.3 and 6.4 show that using the asymmetry estimation for compensation of the asymmetry results in a superior camber reduction. Fig. 6.3 indicates that the centerline of the plate after the last rolling pass shows a small but acceptable camber. The remaining camber is caused by the low-pass filtering of  $\Delta \tilde{\mathbf{h}}^{out}$  which brings along that the estimation  $\Delta \tilde{\mathbf{h}}^{out}$  approaches the real deviation  $\Delta \hat{\mathbf{h}}^{out} - \Delta \mathbf{h}^{out}$  with the dynamics given by (5.11).

For  $\kappa > 1$ , the control strategy achieves a similarly successful reduction of the camber. Generally,  $\kappa > 1$  entails an overcompensation of the camber and may

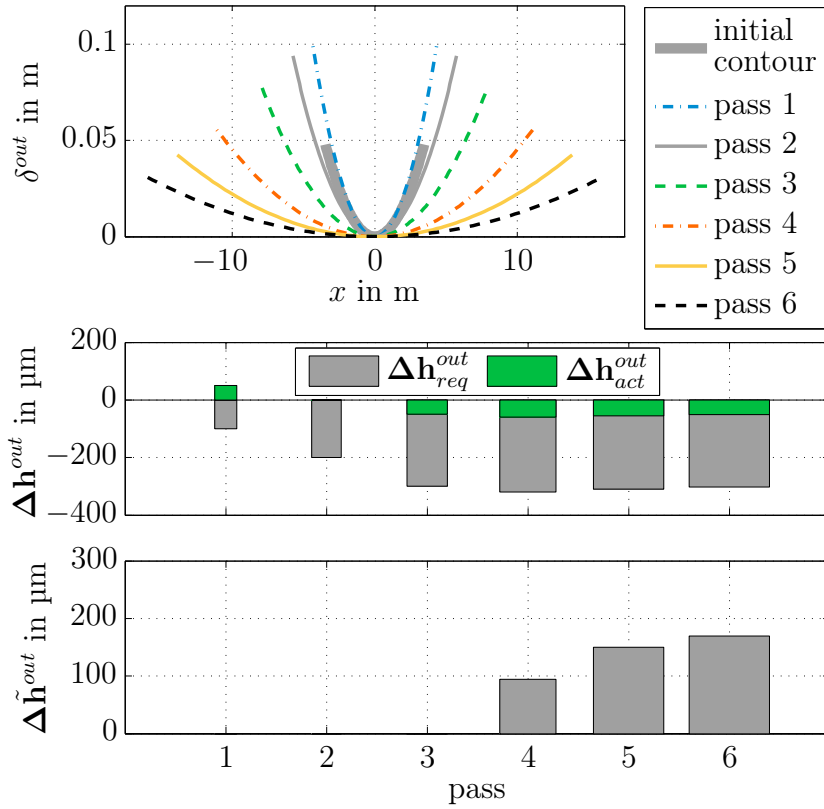


Figure 6.3: Simulation results for an initial input thickness wedge and an initial contour error. Furthermore, a non-ideal position controller of the rolling gap actuators is considered.

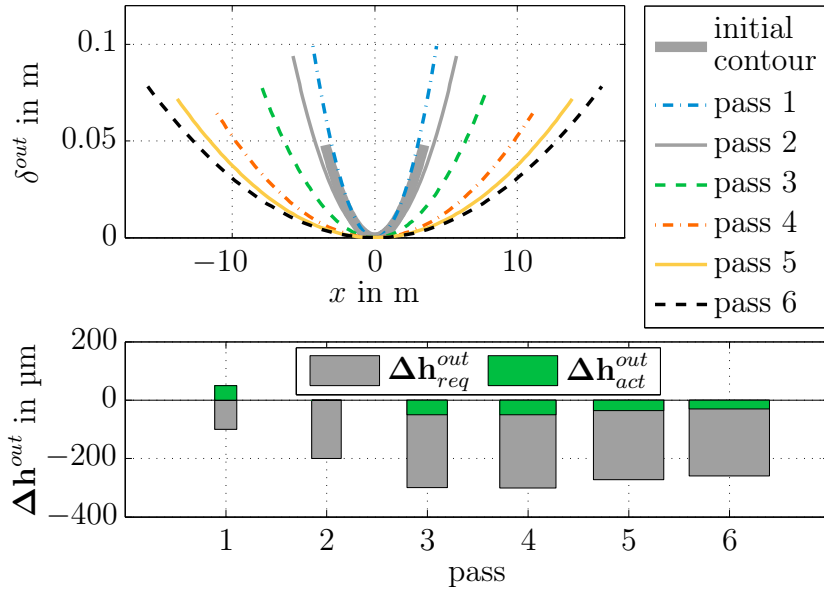


Figure 6.4: Results for the simulation scenario from Fig. 6.3 without using the estimated value  $\tilde{\Delta h}^{out}$ .

thus cause an oscillation of the centerline with respect to  $\delta^{out} = 0$ . In practical terms, the scaling imperfections of the rolling gap actuators are small, i. e.,  $\kappa \approx 1$ , and deteriorate the control result only slightly.

### 6.1.2 Feedback control

In the following, simulation results of the feedback control approach from Section 5.2 are presented. The first simulation covers the last pass of the plate from Section 6.1.1.3 to analyze the potential for improving the final contour of the plate by feedback control. The mathematical model of the movement of the plate (5.13) is used to simulate the contour evolution in the last pass. The input and the output thickness profiles as well as the centerline of the plate before the rolling pass are fed to the mathematical model (5.15a) and (5.15b) and the outputs (5.15c) and (5.15d) are used in the feedback controller.

The plate is rolled with a constant rolling speed  $\bar{v}^{out} = 3 \text{ m/s}$  in forward direction. Furthermore, it is assumed that the upstream angular displacement vanishes, i. e.,  $\Omega^{in} = 0$  (cf. Fig. 4.3) because the upstream side guides are closed. Also the same non-ideal controller of the rolling gap actuators as used in the simulation scenario from Section 6.1.1.3 is considered by choosing  $\tilde{A}_1 = -A_1(1 - \kappa)$  and  $d_1 = A_1 \Delta h_{dist}$ . The disturbance  $d_2$  and the constants  $\tilde{A}_2$  and  $\tilde{A}_3$  are set to zero. The sampling time of the discrete-time controller is set to  $T_{s,fb} = 100 \text{ ms}$  because at the considered rolling mill the desired asymmetry of the output thickness can only be changed with this sampling time. The controller parameters shown in Tab. 6.3 were empirically determined on the mill stand during a commissioning phase with different types of plates. According to the stability analysis from Section 5.2.2.2, the parameters used for the outer controller ensure internal stability for  $|\tilde{\xi}_{cam}| < 2.6 \text{ m}$ . In the simulations  $\tilde{\xi}_{cam} = 0 \text{ m}$  is used.

Parameter	Value	Unit
$V_I$	0.5	$\text{m}^{-1}$
$T_I$	0	m
$V_O$	0.4	$\text{m}^{-1}$
$T_O$	0.1	m
$T_{s,fb}$	100	ms
$u_{1,min}$	-100	$\mu\text{m}$
$u_{1,max}$	100	$\mu\text{m}$
$\xi_{cam}$	5	m
$X_{min}$	9	m

Table 6.3: Parameters used for the simulations of the feedback controller.

Because a central control objective is a straight plate, the desired curvature is set to  $y_{2,ref} = 0$ . The FOVs of the cameras are located  $\xi_{cam} = 5 \text{ m}$  away

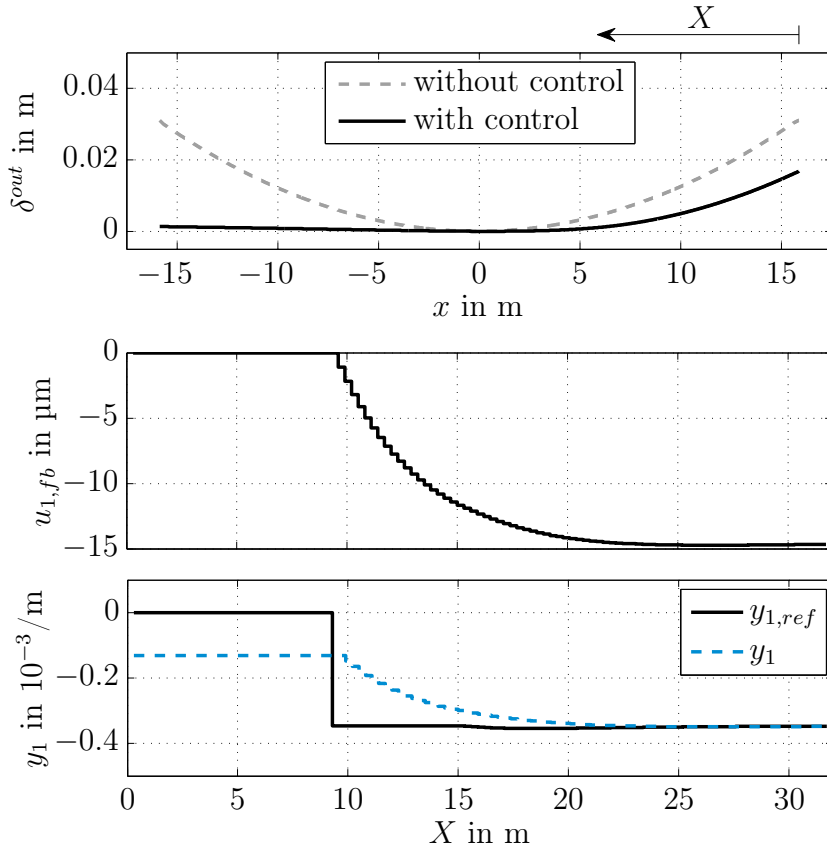


Figure 6.5: Simulation results of the feedback control approach applied to the last rolling pass of Fig. 6.3 with  $d_2 = 0$ .

from the rolling gap. The plate must range a few meters into the FOV for a reliable measurement of the contour and the movement of the plate. Therefore, a rolled plate length larger than the constant  $X_{min}$  is necessary to measure the downstream angular displacement. Hence, the feedback controller is activated when the minimum rolled plate length  $X_{min}$  is reached, i. e.,  $X > X_{min}$  is satisfied for the first time.

Fig. 6.5 shows the simulation results with and without applying the feedback controller. The desired output asymmetry determined by the feedforward controller is used for the feedforward part  $u_{1,ff}$  of the inner loop. For  $X < X_{min}$ , the camber of the plate cannot be reduced because a measurement of the downstream plate is not available. However, for the remaining part of the plate, i. e.  $X \geq X_{min}$ , the curvature can be reduced to almost zero. As shown in Fig. 6.5, the necessary control effort in the form of the output asymmetry is in the range of 15  $\mu\text{m}$ . The lower part of Fig. 6.5 shows that the inner control loop ensures  $y_{1,ref} = y_1$  within a few meters after the activation of the feedback controller. The outer controller should not be activated until  $y_{1,ref} = y_1$  is sufficiently ensured because otherwise the prerequisite of an ideal inner control loop is not fulfilled. For the parameters



used in the inner controller, activating the outer controller for  $X \geq X_{min} + 6$  m has proven to be useful. The control effort  $y_{1,ref}$  of the outer control loop stays almost constant after the activation of the controller.

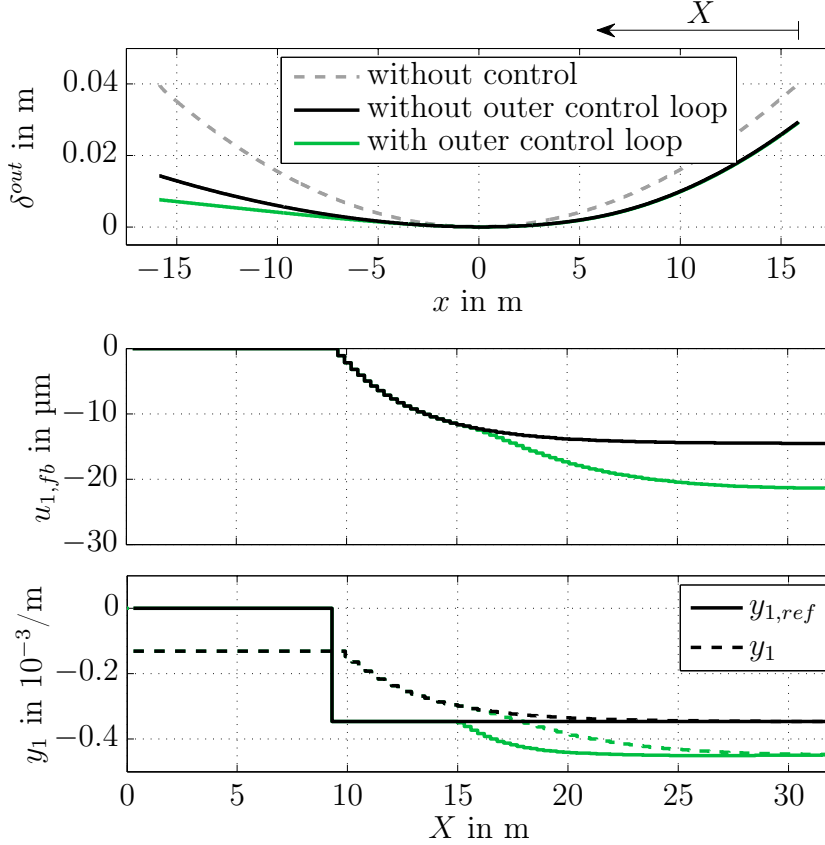


Figure 6.6: Simulation results of the feedback control approach applied to the last rolling pass of Fig. 6.3 with  $d_2 = 0.1 \cdot 10^{-3}/\text{m}$  with and without using the outer control loop.

The second simulation scenario is similar to the first one but uses the constant disturbance  $d_2 = 0.1 \cdot 10^{-3}/\text{m}$ . Fig. 6.6 shows the simulation results with ( $T_O \neq 0$ ,  $V_O \neq 0$ ) and without ( $T_O = 0$ ,  $V_O = 0$ ) the outer feedback controller  $C_O$ . After some distance for the feedback controller to become active ( $X \approx 20$  m), the outer loop compensates the effect of the disturbance  $d_2$ . By contrast, without using the outer control loop the effect of the disturbance  $d_2$  cannot be suppressed.

### 6.1.3 Multi-pass adjustment

As shown in Section 6.1.1, considering just a single pass for the reduction of contour errors may lead to the desired contour after the last rolling pass but in general the final product then shows an asymmetric thickness profile. By using the alternative multi-pass approach from Section 5.3 to create a tailored rolling

schedule, both the desired contour and a homogeneous thickness of the final product can be obtained.

### 6.1.3.1 Compensation of contour errors

The first simulation uses the same scenario as in Section 6.1.1.1, i. e., the plate has an initial thickness wedge ( $\Delta h^{in} = -1$  mm) before the first pass. Contrary to the simulation from Section 6.1.1.1, the initial input thickness is assumed to be known in the calculations. This is because the aim is to determine an optimized

Parameter	Value	Unit
$N_{rp}$	6	
$\tilde{\beta}_1$	$10^{-1}$	$\text{m}^{-4}$
$\tilde{\beta}_2$	$10^3$	$\text{m}^{-2}$
$\tilde{\beta}_3$	$10^4$	$\text{m}^{-4}$
$\tilde{\beta}_4$	$10^{-5}$	

Table 6.4: Parameters used for the simulations of the multi-pass approach.

rolling schedule to get a straight plate with vanishing asymmetry after the last pass. The parameters from Tab. 6.4 are used in addition to the parameters listed in Tab. 6.1.

Fig. 6.7 shows the contour as well as the output asymmetry of the plate in the considered passes. The contour is assumed to be rectangular before the first rolling pass. A small camber is intentionally rolled in the first rolling pass which results in different lengths of the longitudinal boundaries of the plate measured along the coordinate  $x$ . An assumption made in the multi-pass approach is that the plate velocity during the rolling pass is perpendicular to the axis of the mill stand and that the plate does not rotate. Then even a lateral constant plastic deformation along the coordinate  $x$  results in a different elongation of the longitudinal boundaries because of the different lengths before the rolling pass. This effect is utilized in the presented approach to cause an inhomogeneous material flow which skews the contour of the plate in the interim rolling passes such that a homogeneous output thickness profile in the last pass yields a straight centerline. By increasing the weighting factor  $\tilde{\beta}_4$ , the maximum lateral deviation in the interim passes could be decreased. Contrary to the simulation results from the single pass-to-pass approach, the contour of the plate is shown instead of its centerline. This is because the contour (especially the angle between the longitudinal and lateral boundaries) shows the effect of the inhomogeneous material flow.

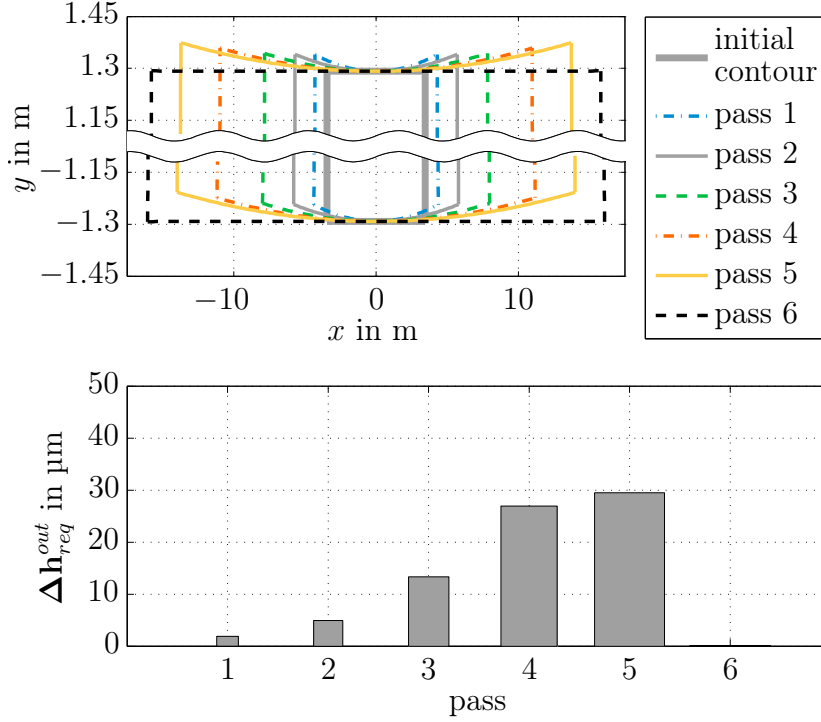


Figure 6.7: Simulation results for a known initial input thickness wedge  $\Delta h^{in} = -1$  mm using the multi-pass approach.

### 6.1.3.2 Rolling of annular sectors

The second simulation addressing the multi-pass approach deals with planning of a rolling schedule for the production of annular sectors. The rolling schedule contains target values of the feedforward and feedback strategy to ensure the desired contour in the considered interim passes and especially after the last pass. Once again, the simulation scenario from Section 6.1.1 is used. However, a symmetric thickness distribution and a rectangular shape of the plate are presumed before the first rolling pass. The plate should have a camber (circular arc) defined by  $\delta_{max} = 150$  mm at the end of the rolling process. Compared to the standard production process where annular sectors are cut out from rectangles, the achievable material savings are approximately 5% in the presented scenario. As shown in Fig. 6.8, the centerline of the plate is first bent in the opposite direction of the desired final camber. In the last pass, the thickness asymmetry vanishes and the curvature of the centerline changes its sign. The final tail and head end of the plate are approximately parallel to the  $y$ -axis.

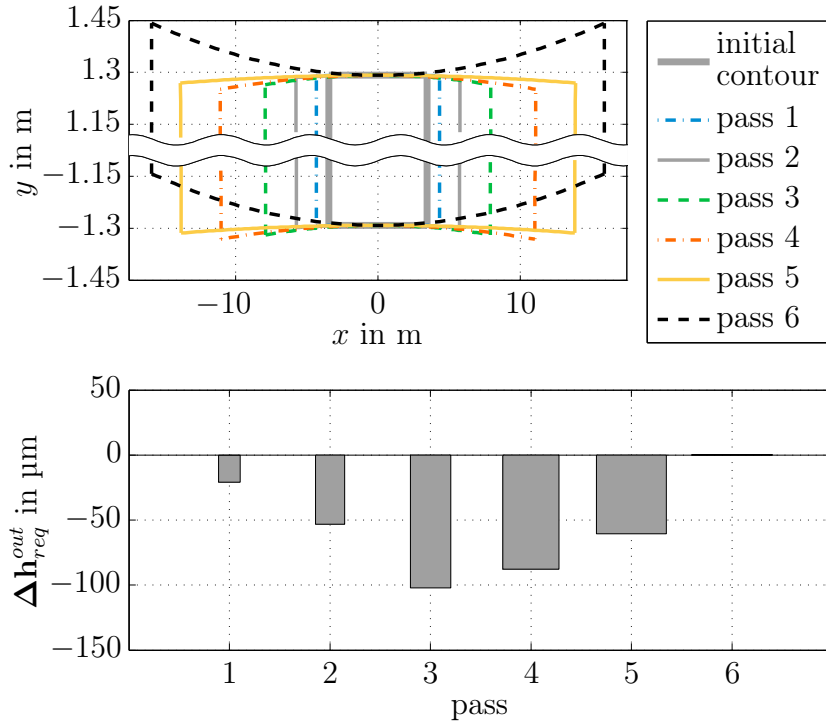


Figure 6.8: Simulation results of the multi-pass approach for rolling an annular sector.

## 6.2 Measurements

In the following, measurement results from plates rolled at AG der Dillinger Hüttenwerke are presented. The discussed control strategies and the algorithmic part of the contour measurement system from Chapter 2 were implemented in C++ and are executed on a standard PC. The data exchange between this PC and the mill stand computer is performed by means of TCP/IP messages. First, measurements from a plate rolled with the single pass-to-pass adjustment are shown. Additionally, a statistic covering several hundred plates demonstrates the feasibility of the contour error reduction approach. In the second part, measurement results of the feedback control approach are presented for an exemplary plate. Again the statistic evaluation of 2500 representative plates shows that the combination of the feedforward with the feedback control approach can significantly improve the contour of the rolled plates.

### 6.2.1 Single pass-to-pass adjustment

Fig. 6.9 illustrates the feedforward control approach in combination with the contour measurement from Chapter 2. The figure shows the mill stand and the two infrared cameras installed at the ceiling of the rolling mill. One camera is

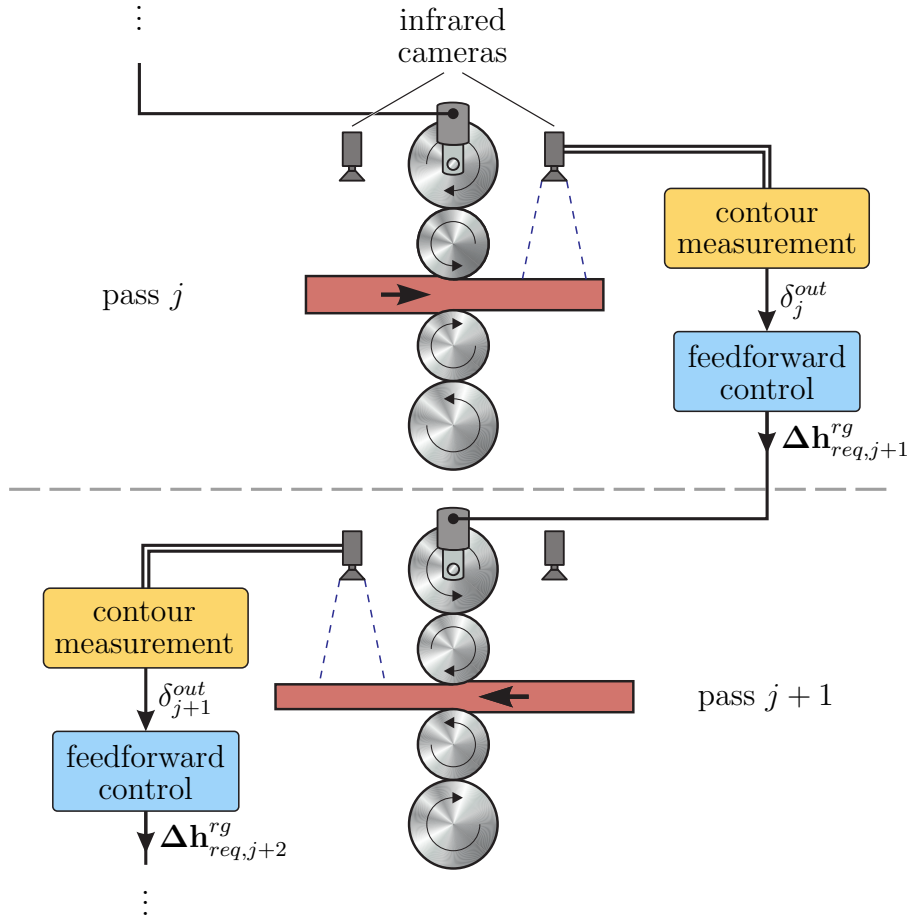


Figure 6.9: Contour measurement in combination with the feedforward control approach.

mounted upstream of the rolling mill to measure the outgoing contour in backward passes. The second camera is located downstream of the rolling mill to capture the outgoing plate contour in forward passes. As shown in Fig. 6.9, the measured contour after the forward pass is used to calculate the required asymmetry of the rolling gap height (characterized by the vector  $\Delta \mathbf{h}_{req}^{rg}$ ) in the consecutive backward pass. Consequently, the measured contour after the backward pass determines the target value of the rolling gap height in the following forward pass, and so on.

In the following, measurement results from a plate rolled during the stan-

pass	1	2	3	4	5	6
$h_{des}^{out}$ in mm	44.7	32.7	23.0	17.2	14.0	12.2

Table 6.5: Production schedule of the plate rolled with the feedforward control approach.

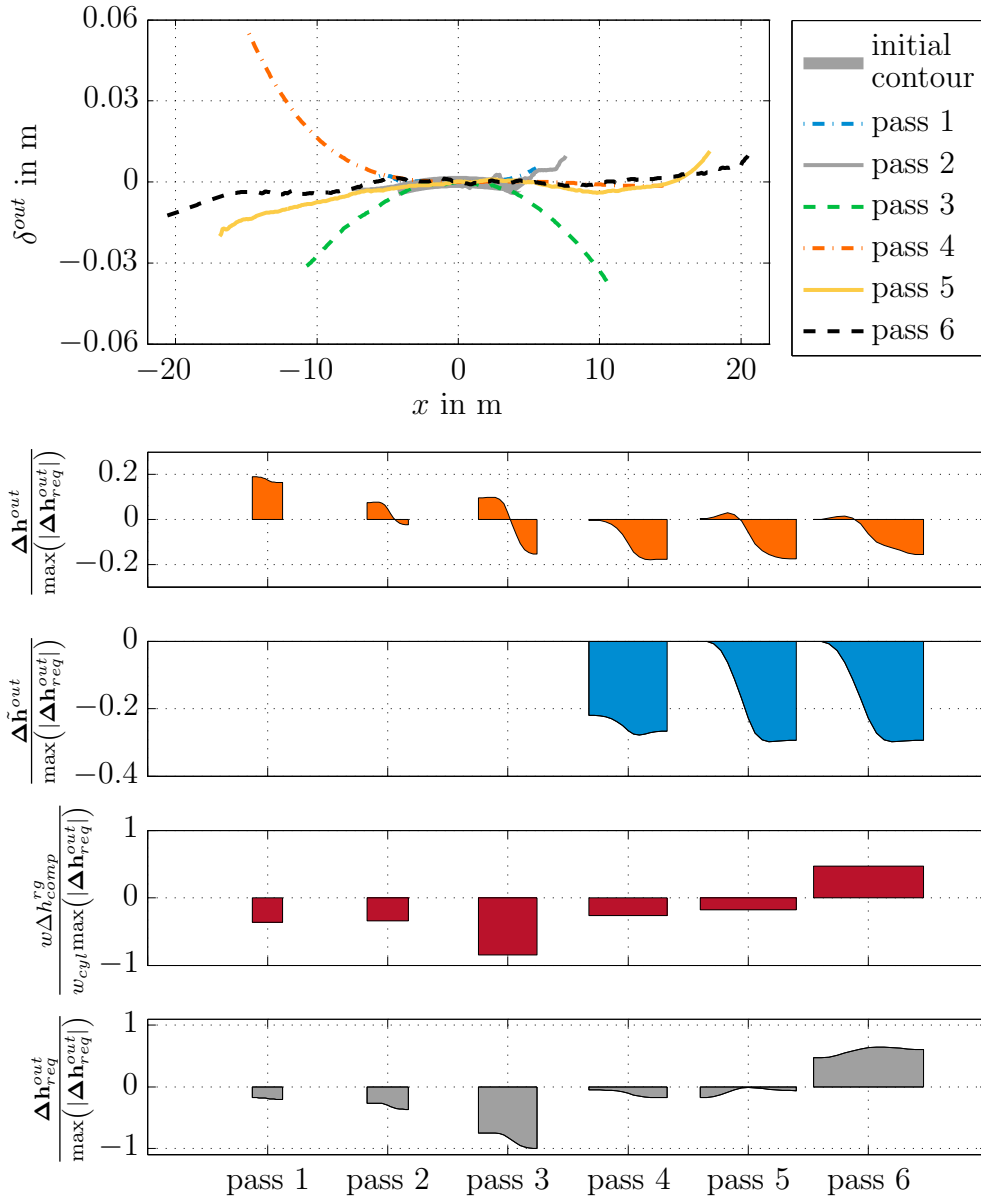


Figure 6.10: Measurement results of the feedforward control approach applied to a 42 m long and 2.7 m wide plate with a final plate thickness of 12.2 mm.

standard production are shown. The same parameters as for the simulations from Section 6.1.1 were used for the feedforward control approach, see Tab. 6.1. The considered plate has a desired final length of 42 m, a desired final width of 2.7 m, and a desired final thickness of 12.2 mm. Tab. 6.5 shows the desired output thickness values  $h_{des}^{out}$  in the interim passes.

Fig. 6.10 shows the evolution of the centerline of the considered plate. The deviations of the centerline can be reduced to very small values after the last pass. The lower part of Fig. 6.10 shows the required asymmetry  $\Delta h_{req}^{out}$  as well as the

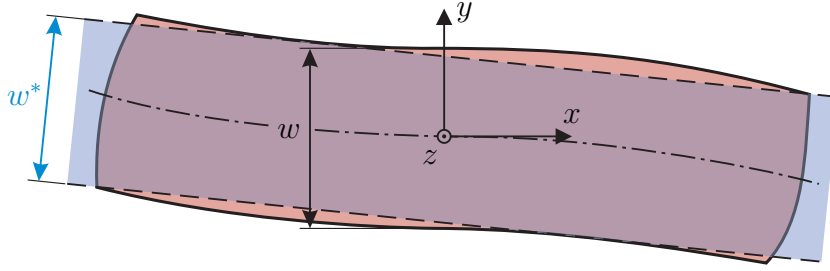


Figure 6.11: Plate with contour error and rectangular usable area inside the longitudinal boundaries of the plate.

asymmetries  $\Delta \mathbf{h}^{out}$ ,  $\Delta \tilde{\mathbf{h}}^{out}$  and  $\Delta h_{comp}^{out}$  normalized to  $\max(|\Delta \mathbf{h}_{req}^{out}|)$ . Only for the passes 4, 5 and 6, an estimation of the input asymmetry and therefore of the disturbance  $\Delta \tilde{\mathbf{h}}^{out}$  is available. Contrary to the simulations from Section 6.1.1, the asymmetries are no longer uniform in longitudinal direction. Furthermore, a large part of the required asymmetry  $\Delta \mathbf{h}_{req}^{out}$  of the mill stand is due to the compensation of the asymmetric deflection of the mill stand. Note that also non-uniform contour errors along the axis  $x$  (e. g. after pass 4) can be compensated by an appropriate profile of the thickness asymmetry along the plate length.

The plates are trimmed to rectangular shapes at the end of the production process. Clearly, the usable area of the plates should be maximized. This requirement is equivalent to maximizing the width of the blue region (usable area) inside the plate boundaries shown in Fig. 6.11 when neglecting the shape of the tail and head end. The maximum width of the usable area is denoted by  $w^*$  (cf.

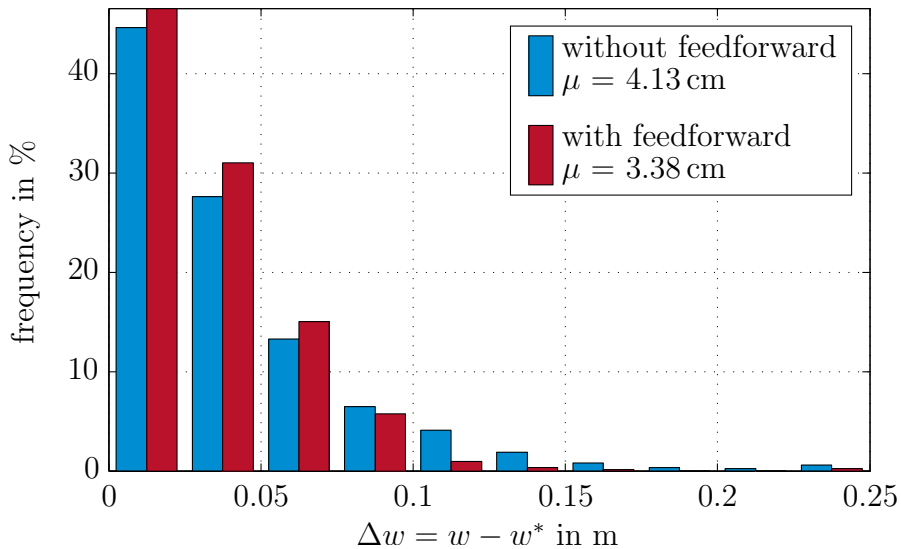


Figure 6.12: Frequency distribution of  $\Delta w$  obtained without and with the feedforward control approach (sample size 800 plates).

Fig. 6.11) and is determined from the longitudinal boundaries of the plate by means of static optimization. In the following, the difference  $\Delta w = w - w^*$  is used as an aggregate measure of the plate width lost due to contour errors.

Fig. 6.12 shows the frequency distribution of contour errors obtained with and without the proposed feedforward control approach. Here,  $\Delta w$  is shown for 800 plates with a minimal plate length of 10 m and a maximum final plate thickness of 30 mm. Shorter and thicker plates are not considered because for such plates camber does not play an important role. The measurements with feedforward control were recorded during the day work shift and the measurements without control actions were recorded during the remaining part of the working day. For the considered plates, the mean value  $\mu$  of  $\Delta w$  has been reduced by approximately 20% by applying the feedforward control approach. That is, the number of plates with small values of  $\Delta w$  has been increased by the feedforward control approach.

## 6.2.2 Feedback control

In this section, measurement results of the feedback control approach are presented. The same parameters as in the simulations of the feedback controller (see Tab. 6.3) are used in the real-time implementation. The center input and output thickness

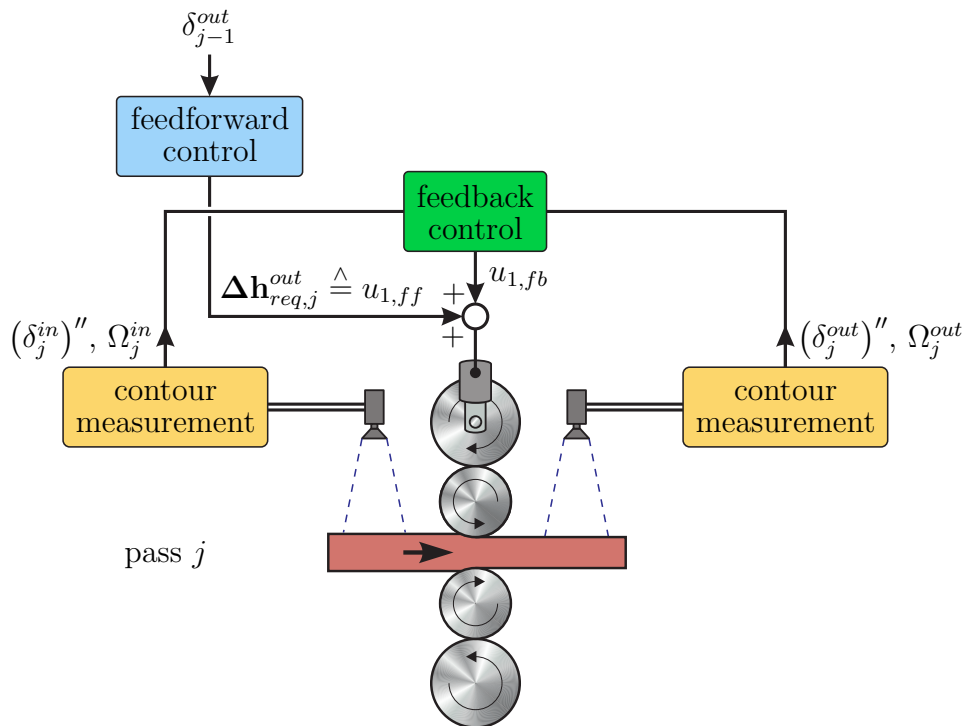


Figure 6.13: Downstream and upstream contour measurement in combination with the feedforward and feedback control approach.



$\bar{h}^{in}$  and  $\bar{h}^{out}$  are set to the desired input and output thickness of the plate, respectively. In addition to the downstream measurement of the contour, also the upstream plate movement and the upstream plate contour have to be measured during a feedback controlled pass (cf. Fig. 6.13).

The contour measurement has a lower sampling time ( $T_s = 33$  ms) compared to the sampling time  $T_{s,fb} = 100$  ms of the feedback controller. To avoid aliasing effects, the mean value of the quantities measured by the contour measurement within a sampling period  $T_{s,fb}$  are used in the feedback controller. At the end of the rolling pass, upstream measurements of the plate are not available due to the distance between the FOV of the camera and the mill stand. If upstream measurements are not available, the upstream quantities  $(\delta^{in})''$  and  $\Omega^{in}$  are set to zero in the feedback controller. Fig. 6.14 shows the results obtained for a plate with a final plate thickness of 12.4 mm and a final plate length of 29.8 m. During this rolling pass, the upstream side guides centered the plate in the lateral direction. The upper part of Fig. 6.14 shows the centerline of the plate before and after the

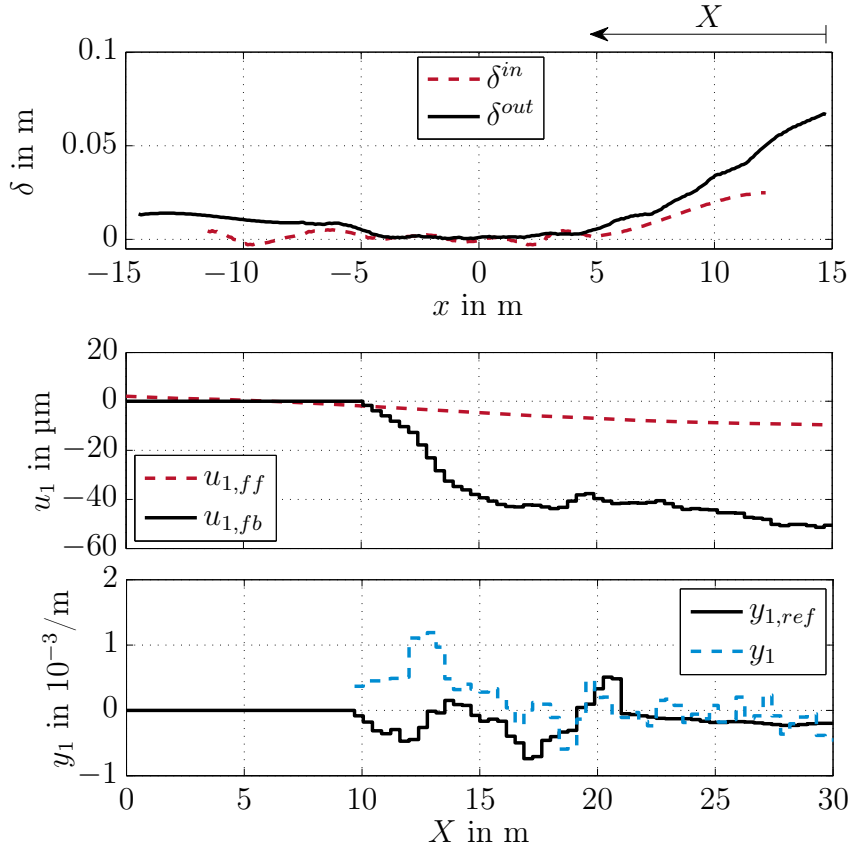


Figure 6.14: Measurement results of the feedback control approach applied to the last pass of a 29.8 m long plate.

rolling pass. The centerline before the rolling pass only shows a small camber. However, the plate shows a considerable camber near the head end ( $x > 5$  m)

after the rolling pass. Nevertheless, the curvature of the downstream centerline has been reduced to almost zero after  $X_{min}$  plus a few meters for the controller to become active. Furthermore, Fig. 6.14 shows the control efforts of the feedforward and the feedback controller  $u_{1,ff}$  and  $u_{1,fb}$ , respectively. The desired and measured downstream angular velocities are shown in the lower part of Fig. 6.14. There exists a large control error  $e_I = y_{1,ref} - y_1$  when the controller is activated at  $X = X_{min} = 9$  m. This error which is linked with the camber of the plate at this time step is reduced by the inner controller to an acceptable level within a few meters. For the considered plate, the measurement of the downstream angular velocity is very noisy. However, the proposed control approach can significantly reduce the camber of the plate even for measurements which are corrupted by large noise.

Fig. 6.15 shows the frequency distribution of the contour errors obtained without any control and with the presented feedforward and feedback control approaches. 2500 plates were rolled with camber control switched on and 2500 plates with comparable dimensions and material properties were rolled without any control. The plates used in the comparison have a minimal plate length of 15 m and a maximum final plate thickness of 30 mm. For shorter plates, almost no improvement of the contour can be achieved by feedback control because of the minimal plate length  $X_{min} = 9$  m associated with the distance between the FOV of the camera and the mill stand.

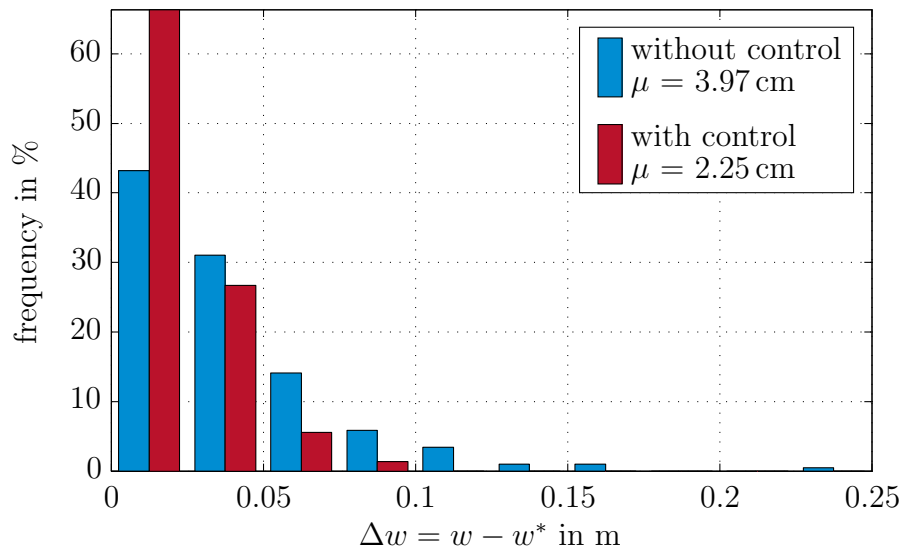


Figure 6.15: Frequency distribution of  $\Delta w$  obtained without any control and with feedforward and feedback control (sample size 2500 plates).

For the considered plates, the mean value of  $\Delta w$  has been reduced by approximately 45% by the combined feedforward and feedback controller. Using both control measures yields  $\Delta w < 5$  cm for 93% of the plates. The number of plates with  $\Delta w > 5$  cm has been reduced to a very low level.

## **6.3 Summary**

In this chapter, simulation results of the proposed control strategies to reduce contour errors were presented. In particular, the effect of disturbances of the input thickness profile and the impact of a non-ideal position controller of the rolling gap actuator on the feedforward and feedback control approaches were investigated. Furthermore, simulation results of the multi-pass approach simultaneously yielding the desired plate contour and a homogeneous thickness profile of the final product were shown. Finally, measurements from the considered industrial rolling mill with a real-time implementation of the developed feedforward and feedback control strategies prove the practical feasibility of the proposed methods.



### 7.1 Summary

This work deals with model-based estimation and control of the contour evolution in heavy-plate rolling. In the first part of the thesis, a new approach for the estimation of the plate contour was discussed. In this approach, the edges of the plate are first detected in bitmaps captured by two infrared cameras. The detected edges are then fed into an optimization-based estimator which fits polynomials to the detected edges. In addition to the contour, the angular movement and the longitudinal velocity of the plate are estimated. The estimator uses a mathematical model of the movement of the plate and systematically considers the restrictions on the lateral movement of the plate in the rolling gap. The longitudinal velocity of the plate is estimated based on the spatial shift of the non-uniform temperature distribution between subsequent bitmaps. The contour estimation was validated by means of measurements from a downstream contour measurement device.

A continuum-mechanics-based model of the contour evolution of the plate was presented. The quasi-static model predicts the contour after the rolling pass based on the contour before the rolling pass and the input and output thickness profiles of the plate. A two-dimensional problem formulation is used and a plane stress distribution is assumed. The resulting system of partial differential equations covering the unknown residual stresses is rewritten as scalar-valued partial differential equation (known as extended biharmonic equation) for a stress function. The biharmonic equation was solved using two-dimensional polynomials and a weighted residual method to fulfill the boundary conditions. By means of this model, the influence of lateral and longitudinal temperature gradients on the contour evolution was discussed. Measurements from a plate rolled during the

standard production process were used to validate the model.

The movement of a plate during a rolling pass is not considered in the quasi-static model of the contour evolution. Online feedback control during the rolling pass, however, requires a mathematical model of the evolution of the camber and the movement of the plate. Hence, a model covering the rotational movement and the camber formation during the rolling pass was developed. The model links the downstream and upstream angular velocities with the curvature before and after the rolling gap. Using the processed plate length as independent variable yields a time-free formulation, which is independent of the rolling speed. Measurements from the developed contour measurement system were used to validate the model.

The presented models of the contour evolution and the movement of the plate are used in different control approaches for the reduction of contour errors. Here, the asymmetry of the rolling gap height serves as control input. First, a feedforward strategy utilizing the static model of the contour evolution was proposed. The optimization-based approach determines the required asymmetry of the rolling gap to compensate a contour error during the subsequent rolling pass. Weighting factors in the objective function can be used to penalize the absolute value of the output asymmetry and its change. Furthermore, constraints on the asymmetry of the plate thickness are systematically incorporated into the optimization problem.

It was found that the compliance of the considered mill stand is slightly asymmetric. The resulting asymmetric deflection is compensated by an empirical approach. Based on the measured contour before and after a rolling pass and the input thickness profile, the deviation between the desired and the actual output thickness asymmetry is estimated so that it can be compensated in subsequent rolling passes. To further improve the contour of the plate, feedback control during the rolling pass was developed. Because the contour of the plate can only be measured with a transport delay, a delay-free measurement of the angular movement is utilized in a two degrees-of-freedom Smith-predictor control structure.

In general, the compensation of contour errors within single passes results in an inhomogeneous thickness profile of the final product. Hence, an approach covering several rolling passes to achieve both the desired contour and a homogeneous thickness was developed. The result of this multi-pass strategy is a rolling schedule which contains reference values for the feedforward and the feedback control approach.

Finally, simulation results and measurements of the proposed control strategies to reduce contour errors were presented. The simulations show the effect of changing the parameterization of the controllers and the influence of disturbances on the control performance. Measurements from an industrial rolling mill including statistical evaluations that cover a representative amount of plates prove the practical feasibility of the proposed methods.

## 7.2 Conclusions

A precise measurement of the plate contour is a key requirement for the reduction of contour errors. The results presented in Section 2.6 demonstrate that the presented contour measurement approach achieves a good accuracy with deviations in the range of a few centimeters in the lateral direction. Also the length of the plates is accurately measured by this approach. Therefore, the results of the contour measurement system can be used as inputs for the reduction of contour errors from pass to pass. The estimated velocity of the plate can also be used for process monitoring, e. g., to validate and, if necessary, to adapt the forward slip model used in the automation system of the mill stand.

The receding horizon estimation approach lowers the computational effort of the contour measurement. This facilitates an online measurement of the contour evolution and thus the use of feedback control approaches during the rolling pass itself. In contrast to the contour measurement concepts known from literature, also the angular velocity of the plate during the rolling pass is estimated, which simplifies the design of feedback controllers. Using infrared cameras instead of visible light cameras is beneficial for the considered application because the plate can be even captured through a cloud of steam and no illumination is needed. Moreover, the developed camera system has proven to be robust against the harsh conditions at the rolling mill for the last two years without any maintenance.

The derived mathematical models for the evolution of the contour and the movement of the plate are tailored to the use in control applications. As the continuum-mechanics-based model is computationally inexpensive but still sufficiently accurate, it can be used in the optimization-based feedforward concept. Because the input and output thickness profiles of the plate are used as inputs of the model no (additional) model of the mill stand and the deformation in the rolling gap is needed. The model was also used to analyze the effect of inhomogeneous temperature distributions. These investigations show that the influence of temperature gradients in the lateral and longitudinal direction may be neglected in the considered application. A validation with a plate rolled during the standard production process confirmed that the model can accurately predict the contour evolution.

The model of the movement of the plate serves as a basis for the design of feedback control strategies. It is tailored to the use with the proposed contour and movement measurements of the plate. The upstream as well as the downstream angular and longitudinal velocities of the plate can be estimated based on the measurements provided by the infrared cameras. Therefore, neither a model for the forward and backward slip nor a parameterization of such a model is needed. This is beneficial because the parameterization of a slip model covering different rolled materials is a delicate task. Measurements for an exemplary plate of the proposed contour measurement approach have shown a small acceptable model mismatch.

Simulation results presented in Section 6.1 further show that the proposed optimization-based feedforward approach can reduce initial contour errors and can successfully handle unknown inhomogeneous initial thickness profiles. Furthermore, disturbances of the output asymmetry or a non-ideal position controller of the rolling gap actuators deteriorate the control performance only slightly. This is due to the estimation of the (real) output asymmetry and the estimation of the disturbance affecting the output asymmetry. Moreover, simulation results demonstrate that the feedback control approach can further improve the final contour of long plates. Here, using the delay-free measurement of the angular velocity in addition to the delayed measurement of the curvature is advantageous in terms of feedback control. Utilizing the multi-pass approach, both the desired contour and a homogeneous thickness profile of the final product can be achieved. Furthermore, the presented approach for the direct rolling of annular sectors allows considerable material savings and cost reductions.

Measurements shown in Section 6.2 demonstrate the effectiveness of the proposed approaches for the reduction of contour errors. Statistical evaluations show a considerable reduction of contour errors already when only using the feedforward approach. A further improvement of the contour is achieved by feedback control in combination with the feedforward approach. In particular, the number of larger contour errors can be significantly decreased. This improvement can only be achieved because the feedback controller utilizes the measurements of the downstream and upstream camera.

Summarizing, the proposed control strategies have proven to be effective to systematically reduce contour errors in heavy-plate rolling. This also simplifies the work of the mill stand operator, who can focus more on monitoring the overall rolling process. Considerable savings of costs can be achieved with the proposed methods because:

- The allowance on the width of the plate can be reduced due to less contour errors.
- The downtime of the mill stand is reduced because large cambers are avoided, which otherwise may lead to damaged plant components nearby the mill stand.
- The product portfolio can be expanded by long thin products which cannot be properly rolled with pure manual adjustment of the mill stand by the operator.

### 7.3 Outlook

Currently, the proposed control strategies for the reduction of contour errors are used in an industrial pilot installation where their performance is permanently



supervised by a human operator. It is planned to further test the system in twenty-four hours operation without any supervision in the subsequent months. The algorithms of the contour measurement and the feedforward and feedback control algorithms are executed on a separate PC which communicates with the mill stand computer. Future work concerns the transfer of the algorithms to the mill stand computer. This makes a communication with the mill stand computer unnecessary and may help to improve the robustness of the control system against network failures.

Until now, only the single pass-to-pass approach and the feedback controller were implemented at the considered rolling mill. Because of the promising results of the single-pass feedforward and feedback approaches, it is planned to perform a test campaign using the multi-pass approach. This will include the reduction of contour errors across several passes by simultaneously achieving a homogeneous thickness profile of the final product. Also the tailored rolling of annular sectors will be tested in near future. To this end, the controller of the rolling gap height has to be adapted to cope with the off-centering of the plate during the rolling pass.

Using infrared cameras has proven to be useful for the measurement of the plate contour during the hot-rolling process. However, the use of infrared cameras in the hot rolling process may be extended. Further applications in rolling mills include material tracking of heavy plates. The knowledge of the plate position and the continuous measurement of the plate temperature by the infrared camera can be used to further monitor and automatize the handling of the products. Ideally, the plate is tracked from the exit of the reheating furnace to the last production step, e. g., inspection. Clearly, many plates are processed at the same time in modern rolling mills and have to be robustly distinguished. Further research questions may be related to the tracking of plates with several cameras covering the interesting parts of the production line. This includes the handling of several plates at the same time and additionally the processing of images captured by different cameras. The first steps towards material tracking are shown in [25] where the movements of the plates in front of the mill stand are tracked in real time.



# APPENDIX A

---

## Static optimization

---

This appendix presents numerical methods to solve unconstrained static optimization problems and gives an overview of the methods used in this work. A more detailed description of the methods may be found in [47]. The unconstrained static optimization problem is formulated as

$$\min_{\mathbf{w} \in \mathbb{R}^N} J(\mathbf{w}), \quad (\text{A.1})$$

where  $\mathbf{w} = [w_1 \ w_2 \ \dots \ w_N]^T$  is the vector of optimization variables and  $J(\mathbf{w})$  is the scalar valued twice continuously differentiable objective function. Sufficient conditions for a local minimum of  $J(\mathbf{w}^*)$  at the optimal point  $\mathbf{w}^*$  have the form (cf. [47])

$$\nabla J(\mathbf{w}^*) = \mathbf{0} \quad (\text{A.2a})$$

$$\mathbf{s}^T \nabla^2 J(\mathbf{w}^*) \mathbf{s} > 0 \quad (\text{A.2b})$$

for all vectors  $\mathbf{s} \in \mathbb{R}^N$  and the Nabla operator  $\nabla$ . In most cases, (A.2) cannot be solved analytically. Therefore, it is common to use iterative numerical methods. Starting with an initial guess for  $\mathbf{w}$ , the objective function is decreased in every iteration. The iteration stops if a termination criterion is satisfied or the maximum number of iterations is exceeded.

The literature offers a huge collection of suitable algorithms for solving the optimization problem (A.1), for instance, the steepest descent method [47], the conjugate gradient method [52], the quasi-Newton method [53], the Newton's method [54], and the Gauss-Newton method [47]. They differ in their theoretical convergence rate and the computational effort necessary in every iteration. Clearly, for the real-time capable estimation and control algorithms presented in this work,

short optimization times have to be achieved. The time required to solve a specific optimization problem depends on the achieved convergence rate of the algorithm and the computational effort associated with each iteration. To achieve short optimization times, different tailored algorithms are used in this work.

The presented methods are called line search strategies, where the value of the objective function is decreased along the search direction  $\mathbf{d}_l$  in every iteration  $l$ . The step length  $\alpha_l$  along  $\mathbf{d}_l$  is determined by solving a one-dimensional optimization problem. The iterative procedure to solve the optimization problem (A.1) proceeds as follows:

Step 0: Choose the initial guess  $\mathbf{w}_0$  and set  $l = 0$ .

Step 1: Compute the search direction  $\mathbf{d}_l$ .

Step 2: Perform a line search, i. e. solve

$$\min_{\alpha_l \geq 0} J(\mathbf{w}_l + \alpha_l \mathbf{d}_l) \text{ and apply the update} \\ \mathbf{w}_{l+1} = \mathbf{w}_l + \alpha_l \mathbf{d}_l.$$

Step 3: Check if any termination criterion (maximum number of iterations, convergence) is fulfilled. If yes, stop here.

Step 4: Increment  $l$  and start again at Step 1.

In the following, algorithms with different approaches to choose the search direction  $\mathbf{d}_l$  and to solve the line search problem are discussed.

## A.1 Newton method

The search direction according to Newton's method is derived from the second-order Taylor series approximation of  $J(\mathbf{w}_l + \mathbf{d}_l)$  at the point  $\mathbf{w}_l$ , which is given by

$$J(\mathbf{w}_l + \mathbf{d}_l) \approx J(\mathbf{w}_l) + \mathbf{d}_l^T \mathbf{g}_l + \frac{1}{2} \mathbf{d}_l^T \mathbf{H}_l \mathbf{d}_l, \quad (\text{A.3})$$

with the gradient  $\mathbf{g}_l = \nabla J(\mathbf{w}_l)$  and the Hessian  $\mathbf{H}_l = \nabla^2 J(\mathbf{w}_l)$ . The search direction of Newton's method follows in the form

$$\mathbf{d}_l = -\mathbf{H}_l^{-1} \mathbf{g}_l.$$

The vector  $\mathbf{d}_l$  minimizes the right-hand side of (A.3). Newton's method features a superlinear convergence rate (cf. [47]). However, the calculation of the inverse Hessian in every iteration entails a high computational effort.

## A.2 Quasi-Newton method

Quasi-Newton methods provide an attractive alternative to Newton's method because they do not require the calculation of the Hessian. However, they can still achieve a superlinear convergence rate. In fact, an approximation  $\tilde{\mathbf{H}}_l^{-1}$  of the inverse of the Hessian is used, which is iteratively updated in every iteration. One method to update  $\tilde{\mathbf{H}}_l^{-1}$  is the BFGS (Broyden-Fletcher-Goldfarb-Shanno) rule, which follows as

$$\tilde{\mathbf{H}}_{l+1}^{-1} = \left( \mathbf{I} - \frac{\mathbf{d}_l \mathbf{q}_l^T}{\mathbf{q}_l^T \mathbf{d}_l} \right) \tilde{\mathbf{H}}_l^{-1} \left( \mathbf{I} - \frac{\mathbf{q}_l \mathbf{d}_l^T}{\mathbf{q}_l^T \mathbf{d}_l} \right) + \frac{\mathbf{d}_l \mathbf{d}_l^T}{\mathbf{q}_l^T \mathbf{d}_l} \alpha_l,$$

with  $\mathbf{q}_l = \mathbf{g}_{l+1} - \mathbf{g}_l$  and the identity matrix  $\mathbf{I} \in \mathbb{R}^{N \times N}$ . The search direction  $\mathbf{d}_l$  reads as

$$\mathbf{d}_l = -\tilde{\mathbf{H}}_l^{-1} \mathbf{g}_l.$$

A crucial point for the achieved convergence rate of the quasi-Newton method is the choice of the initial guess  $\tilde{\mathbf{H}}_0^{-1}$  (cf. [47]). In so called least-squares problems, the objective function may be written in the special form

$$J(\mathbf{w}) = \mathbf{e}^T(\mathbf{w})\mathbf{e}(\mathbf{w}),$$

where the vector  $\mathbf{e} = [e_1 \ e_2 \ \dots \ e_M]^T$  contains scalar functions of  $\mathbf{w}$ . Let the Jacobian  $\mathbf{J}$  of  $\mathbf{e}$  with respect to  $\mathbf{w}$  be denoted as

$$\mathbf{J}(\mathbf{w}) = (\nabla \mathbf{e})^T.$$

Hence, the Hessian of  $J(\mathbf{w})$  can be written as

$$\nabla^2 J(\mathbf{w}) = 2\mathbf{J}^T(\mathbf{w})\mathbf{J}(\mathbf{w}) + 2\mathbf{\Gamma},$$

with  $\mathbf{\Gamma} = [\Gamma_{q,n}]$  and

$$\Gamma_{q,n} = \sum_{j=1}^M e_j \frac{\partial^2 e_j}{\partial w_q \partial w_n} \quad \forall q, n \in \{1, 2, \dots, N\}.$$

This motivates the initial guess

$$\tilde{\mathbf{H}}_0^{-1} = \left( 2\mathbf{J}^T(\mathbf{w}_0)\mathbf{J}(\mathbf{w}_0) \right)^{-1}, \quad (\text{A.4})$$

which requires  $M \geq N$ .  $\tilde{\mathbf{H}}_0^{-1}$  is a positive definite approximation of the inverse of the Hessian.  $\mathbf{\Gamma}$  (second order derivatives) is typically neglected.

The expression  $\left( 2\mathbf{J}^T(\mathbf{w}_l)\mathbf{J}(\mathbf{w}_l) \right)^{-1}$  could also be used as an approximation of the inverse Hessian in every iteration of the optimization problem. This choice is made in the Gauss-Newton method (cf. [47]) presented in the following.

### A.3 Gauss-Newton method

As described in Section A.2, the Gauss-Newton method exploits the quadratic form of the objective function of least-squares problems to avoid the costly computation of the Hessian. The search direction follows as

$$\mathbf{d}_l = - \left( 2\mathbf{J}^T(\mathbf{w}_l)\mathbf{J}(\mathbf{w}_l) \right)^{-1} \mathbf{g}_l, \quad (\text{A.5})$$

with the gradient  $\mathbf{g}_l = 2\mathbf{J}^T(\mathbf{w}_l)\mathbf{e}_l$ . The Gauss-Newton method features a very good convergence rate for the optimization problems considered in this work. However, the computational effort of the matrix multiplications and of the solution  $\mathbf{d}_l$  of the linear equation  $-\left(2\mathbf{J}^T(\mathbf{w}_l)\mathbf{J}(\mathbf{w}_l)\right)\mathbf{d}_l = \mathbf{g}_l$  (cf. (A.5)) may lead to larger optimization times compared to the quasi-Newton method.

### A.4 Line search

In every iteration  $l$ , the step size  $\alpha_l$  to move along the search direction  $\mathbf{d}_l$  has to be determined. The natural step length is  $\alpha_l = 1$  for all three discussed methods. This is because choosing  $\alpha_l = 1$  minimizes the objective function if the quadratic approximation from (A.3) is exact. In general, the approximation is not exact and therefore a line search based on a quadratic interpolation of the objective function

$$J(\mathbf{w}_l + \alpha_l\mathbf{d}_l) \approx a_0 + a_1\alpha_l + a_2\alpha_l^2 \quad (\text{A.6})$$

with coefficients  $a_i$ ,  $i = 0, 1, 2$ , is performed. Two different methods to determine the coefficients of the quadratic interpolation are used in this work.

#### A.4.1 Line search I

In the first line search approach, the objective function is evaluated at three different step sizes  $\alpha_l \in \{0, 0.5, 1\}$ . The coefficients in (A.6) follow as

$$a_0 = J_0, \quad a_1 = -3J_0 - J_1 + 4J_{0.5}, \quad a_2 = 2J_0 + 2J_1 - 4J_{0.5},$$

where

$$J_0 = J(\mathbf{w}_l), \quad J_{0.5} = J(\mathbf{w}_l + 0.5\mathbf{d}_l)$$

and

$$J_1 = J(\mathbf{w}_l + \mathbf{d}_l).$$

The optimal step length  $\alpha_l^*$  that minimizes the polynomial (A.6) reads as

$$\alpha_l^* = \frac{1}{4} \frac{3J_0 + J_1 - 4J_{0.5}}{J_0 + J_1 - 2J_{0.5}}.$$

### A.4.2 Line search II

The second method uses the derivative of the objective function at  $\alpha_l = 0$  in the quadratic approximation. The polynomial coefficients  $a_0$ ,  $a_1$  and  $a_2$  can be computed in the form

$$a_0 = J_0, \quad a_1 = J'_0, \quad a_2 = J_1 - J_0 - J'_0,$$

where

$$J'_0 = \left. \frac{dJ(\mathbf{w}_l + \alpha_l \mathbf{d}_l)}{d\alpha_l} \right|_{\alpha_l=0} = \mathbf{d}_l^T \mathbf{g}_l.$$

The optimal step length  $\alpha_l^*$  that minimizes the right-hand side of (A.6) is therefore

$$\alpha_l^* = \frac{1}{2} \frac{J'_0}{J_0 + J'_0 - J_1}.$$

The second line search approach requires only two evaluations of the objective function in every iteration, which reduces the computational effort compared to the first line search method. However, the first line search may lead to a more accurate approximation of the left-hand side of (A.6) and thus to a greater improvement of the objective function value in each iteration. This behavior was especially observed for line search problems with an inaccurate approximation by means of the right-hand side of (A.6).





---

### Gradients used in the estimation of the plate contour

---

In the sequel, the analytical gradients of the objective function (2.12) with respect to the optimization variables  $\boldsymbol{\omega}$ ,  $\mathbf{v}_S$ ,  $\mathbf{p}_L$ , and  $v_L$  are summarized. The gradient of  $J(\mathbf{w}) = J(\boldsymbol{\omega}, \mathbf{v}_S, \mathbf{p}_L, v_L)$  with respect to the angular velocities  $\omega_r$ ,  $r = 0, \dots, N-1$  has the form

$$\frac{d}{d\omega_r} J(\mathbf{w}) = 2 \sum_{k=0}^N \sum_{j=1}^{M_L} e_{L,j,k} \frac{d}{d\omega_r} e_{L,j,k} + 2 \sum_{k=0}^N \sum_{j=1}^{M_H} e_{H,j,k} \frac{d}{d\omega_r} e_{H,j,k}$$

with

$$\frac{d}{d\omega_r} e_{L,j,k} = \frac{\partial p_L(\xi_{L,j,k})}{\partial \xi_{L,j,k}} \frac{d\xi_{L,j,k}}{d\omega_r} - \frac{d\eta_{L,j,k}}{d\omega_r} \quad (\text{B.1})$$

and

$$\frac{d}{d\omega_r} e_{H,j,k} = \frac{\partial p_H(\eta_{H,j,k})}{\partial \eta_{H,j,k}} \frac{d\eta_{H,j,k}}{d\omega_r} - \frac{d\xi_{H,j,k}}{d\omega_r} \quad (\text{B.2})$$

according to (2.9) and (2.8), respectively.

The additional derivatives used in (B.1) can be calculated as

$$\frac{\partial p_L(\xi_{L,j,k})}{\partial \xi_{L,j,k}} = c_{L,1} + 2c_{L,2}\xi_{L,j,k} + \dots + N_L c_{L,N_L} \xi_{L,j,k}^{N_L-1} \quad (\text{B.3a})$$

$$\begin{aligned} \frac{d\xi_{L,j,k}}{d\omega_r} &= -(\xi_{ml,j} - \Delta\xi_k) \sin(\varphi_k) \frac{d\varphi_k}{d\omega_r} \\ &\quad + (\eta_{ml,j,k} - \Delta\eta_k) \cos(\varphi_k) \frac{d\varphi_k}{d\omega_r} \\ &\quad - \cos(\varphi_k) \frac{d\Delta\xi_k}{d\omega_r} - \sin(\varphi_k) \frac{d\Delta\eta_k}{d\omega_r} \end{aligned} \quad (\text{B.3b})$$

$$\begin{aligned} \frac{d\eta_{L,j,k}}{d\omega_r} &= -(\eta_{ml,j,k} - \Delta\eta_k) \sin(\varphi_k) \frac{d\varphi_k}{d\omega_r} \\ &\quad - (\xi_{ml,j} - \Delta\xi_k) \cos(\varphi_k) \frac{d\varphi_k}{d\omega_r} \\ &\quad - \cos(\varphi_k) \frac{d\Delta\eta_k}{d\omega_r} + \sin(\varphi_k) \frac{d\Delta\xi_k}{d\omega_r} \end{aligned} \quad (\text{B.3c})$$

(cf. (2.13) and (2.14)). The derivatives utilized in (B.2) may be obtained by exchanging  $p_L$  with  $p_H$ ,  $N_L$  with  $N_H$ ,  $c_{L,i}$  with  $c_{H,i}$  and  $\xi_{L,j,k}$  with  $\eta_{H,j,k}$  in (B.3a). Moreover,  $\xi_{L,j,k}$  has to be replaced by  $\xi_{H,j,k}$ ,  $\eta_{L,j,k}$  by  $\eta_{H,j,k}$ ,  $\xi_{ml,j}$  by  $\xi_{mh,j,k}$  and  $\eta_{ml,j,k}$  by  $\eta_{mh,j}$  in (B.3b) and (B.3c), respectively.

Based on (2.11), the derivatives  $\frac{d\mathbf{x}_k}{d\omega_r}$  can be recursively computed in the form

$$\frac{d\mathbf{x}_k}{d\omega_r} = \begin{cases} \mathbf{0} & \text{if } r \geq k \\ \frac{\partial \mathbf{f}(\mathbf{x}_r, \omega_r, v_{S,r}, v_L)}{\partial \omega_r} + \frac{\partial \mathbf{f}(\mathbf{x}_r, \omega_r, v_{S,r}, v_L)}{\partial \mathbf{x}_r} \frac{d\mathbf{x}_r}{d\omega_r} & \text{if } r = k - 1 \\ \frac{\partial \mathbf{f}(\mathbf{x}_{k-1}, \omega_{k-1}, v_{S,k-1}, v_L)}{\partial \mathbf{x}_{k-1}} \frac{d\mathbf{x}_{k-1}}{d\omega_r} & \text{if } r < k - 1 \end{cases}$$

with

$$\frac{\partial \mathbf{f}(\mathbf{x}_r, \omega_r, v_{S,r}, v_L)}{\partial \omega_r} = T_s \begin{bmatrix} -\Delta\xi_r \sin(\bar{\omega}_r) - \Delta\eta_r \cos(\bar{\omega}_r) + \frac{v_L}{\omega_r} \cos(\bar{\omega}_r) \\ -\frac{v_L}{\omega_r^2 T_s} \sin(\bar{\omega}_r) - \frac{v_{S,r}}{\omega_r} \sin(\bar{\omega}_r) - \frac{v_{S,r}}{\omega_r^2 T_s} (\cos(\bar{\omega}_r) - 1) \\ \Delta\xi_r \cos(\bar{\omega}_r) - \Delta\eta_r \sin(\bar{\omega}_r) + \frac{v_L}{\omega_r} \sin(\bar{\omega}_r) \\ -\frac{v_L}{\omega_r^2 T_s} (1 - \cos(\bar{\omega}_r)) + \frac{v_{S,r}}{\omega_r} \cos(\bar{\omega}_r) - \frac{v_{S,r}}{\omega_r^2 T_s} \sin(\bar{\omega}_r) \\ 1 \end{bmatrix}$$

and

$$\frac{\partial \mathbf{f}(\mathbf{x}_r, \omega_r, v_{S,r}, v_L)}{\partial \mathbf{x}_r} = \begin{bmatrix} \cos(\bar{\omega}_r) & -\sin(\bar{\omega}_r) & 0 \\ \sin(\bar{\omega}_r) & \cos(\bar{\omega}_r) & 0 \\ 0 & 0 & 1 \end{bmatrix}, \quad (\text{B.4})$$

where the abbreviation  $\bar{\omega}_r = \omega_r T_s$  was used.

The gradient of (2.12) with respect to  $v_{S,r}$  reads as

$$\frac{d}{dv_{S,r}} J(\mathbf{w}) = 2 \sum_{k=0}^N \sum_{j=1}^{M_L} e_{L,j,k} \frac{d}{dv_{S,r}} e_{L,j,k} + 2 \sum_{k=0}^N \sum_{j=1}^{M_H} e_{H,j,k} \frac{d}{dv_{S,r}} e_{H,j,k}$$

with

$$\frac{d}{dv_{S,r}} e_{L,j,k} = \frac{\partial p_L(\xi_{L,j,k})}{\partial \xi_{L,j,k}} \frac{d\xi_{L,j,k}}{dv_{S,r}} - \frac{d\eta_{L,j,k}}{dv_{S,r}}$$

and

$$\frac{d}{dv_{S,r}} e_{H,j,k} = \frac{\partial p_H(\eta_{H,j,k})}{\partial \eta_{H,j,k}} \frac{d\eta_{H,j,k}}{dv_{S,r}} - \frac{d\xi_{H,j,k}}{dv_{S,r}}.$$

The expressions

$$\frac{d\xi_{L,j,k}}{dv_{S,r}} = \frac{d\xi_{H,j,k}}{dv_{S,r}} = -\cos(\varphi_k) \frac{d\Delta\xi_k}{dv_{S,r}} - \sin(\varphi_k) \frac{d\Delta\eta_k}{dv_{S,r}}$$

and

$$\frac{d\eta_{L,j,k}}{dv_{S,r}} = \frac{d\eta_{H,j,k}}{dv_{S,r}} = -\cos(\varphi_k) \frac{d\Delta\eta_k}{dv_{S,r}} + \sin(\varphi_k) \frac{d\Delta\xi_k}{dv_{S,r}}$$

follow in the form

$$\frac{d\mathbf{x}_k}{dv_{S,r}} = \begin{cases} \mathbf{0} & \text{if } r \geq k \\ \frac{\partial \mathbf{f}(\mathbf{x}_r, \omega_r, v_{S,r}, v_L)}{\partial v_{S,r}} + \frac{\partial \mathbf{f}(\mathbf{x}_r, \omega_r, v_{S,r}, v_L)}{\partial \mathbf{x}_r} \frac{d\mathbf{x}_r}{dv_{S,r}} & \text{if } r = k - 1 \\ \frac{\partial \mathbf{f}(\mathbf{x}_{k-1}, \omega_{k-1}, v_{S,k-1}, v_L)}{\partial \mathbf{x}_{k-1}} \frac{d\mathbf{x}_{k-1}}{dv_{S,r}} & \text{if } r < k - 1 \end{cases}$$

using (B.4) and

$$\frac{\partial \mathbf{f}(\mathbf{x}_r, \omega_r, v_{S,r}, v_L)}{\partial v_{S,r}} = \frac{1}{\omega_r} \begin{bmatrix} \cos(\omega_r T_s) - 1 \\ \sin(\omega_r T_s) \\ 0 \end{bmatrix}.$$

The gradient of the objective function  $J(\mathbf{w})$  with respect to the parameter vector  $\mathbf{p}_L$  is

$$\frac{d}{d\mathbf{p}_L} J(\mathbf{w}) = 2 \sum_{k=0}^N \sum_{j=1}^{M_L} e_{L,j,k} \begin{bmatrix} 1 & \xi_{L,j,k} & \xi_{L,j,k}^2 & \dots & \xi_{L,j,k}^{N_L} \end{bmatrix}.$$

The gradient of the objective function  $J(\mathbf{w})$  with respect to  $v_L$  reads as

$$\frac{d}{dv_L} J(\mathbf{w}) = 2 \sum_{k=0}^N \sum_{j=1}^{M_L} e_{L,j,k} \frac{d}{dv_L} e_{L,j,k} + 2 \sum_{k=0}^N \sum_{j=1}^{M_H} e_{H,j,k} \frac{d}{dv_L} e_{H,j,k}$$

with

$$\frac{d}{dv_L} e_{L,j,k} = \frac{\partial p_L(\xi_{L,j,k})}{\partial \xi_{L,j,k}} \frac{d\xi_{L,j,k}}{dv_L} - \frac{d\eta_{L,j,k}}{dv_L}$$

and

$$\frac{d}{dv_L} e_{H,j,k} = \frac{\partial p_H(\eta_{H,j,k})}{\partial \eta_{H,j,k}} \frac{d\eta_{H,j,k}}{dv_L} - \frac{d\xi_{H,j,k}}{dv_L}.$$

Here, it is necessary to calculate

$$\frac{d\xi_{L,j,k}}{dv_L} = \frac{d\xi_{H,j,k}}{dv_L} = -\cos(\varphi_k) \frac{d\Delta\xi_k}{dv_L} - \sin(\varphi_k) \frac{d\Delta\eta_k}{dv_L}$$

and

$$\frac{d\eta_{L,j,k}}{dv_L} = \frac{d\eta_{H,j,k}}{dv_L} = -\cos(\varphi_k) \frac{d\Delta\eta_k}{dv_L} + \sin(\varphi_k) \frac{d\Delta\xi_k}{dv_L}$$

with the recursive definition

$$\frac{d\mathbf{x}_k}{dv_L} = \begin{cases} \mathbf{0} & \text{if } k = 0 \\ \frac{1}{\omega_{k-1}} \begin{bmatrix} \sin(\omega_{k-1} T_s) \\ 1 - \cos(\omega_{k-1} T_s) \\ 0 \end{bmatrix} + \frac{\partial \mathbf{f}(\mathbf{x}_{k-1}, \omega_{k-1}, v_{S,k-1}, v_L)}{\partial \mathbf{x}_{k-1}} \frac{d\mathbf{x}_{k-1}}{dv_L} & \text{if } k > 0 \end{cases}$$

using (B.4).

## APPENDIX C

---

### Proof of the robust stability of the feedback control loop

---

For proving BIBO stability of (5.22), it is sufficient to satisfy

$$\Re\{1 + L(s)\} > 0 \quad \forall s \in \bar{N}_\infty. \quad (\text{C.1})$$

Insertion of  $L(s)$  from (5.23) into (C.1) and evaluation along the  $j\omega$ -axis yields

$$\frac{1}{V_O} + \frac{1}{\omega} \left[ \sin(\omega\xi_{cam}) - \sin(\omega\bar{\xi}_{cam}) \right] + T_O \left[ 1 - \cos(\omega\xi_{cam}) + \cos(\omega\bar{\xi}_{cam}) \right] > 0.$$

Applying the summation formulas for trigonometric functions results in

$$\begin{aligned} \frac{1}{V_O} + T_O &> 2T_O \sin\left(\frac{\omega(2\xi_{cam} + \tilde{\xi}_{cam})}{2}\right) \sin\left(\frac{\omega\tilde{\xi}_{cam}}{2}\right) \\ &+ \frac{2}{\omega} \cos\left(\frac{\omega(2\xi_{cam} + \tilde{\xi}_{cam})}{2}\right) \sin\left(\frac{\omega\tilde{\xi}_{cam}}{2}\right). \end{aligned} \quad (\text{C.2})$$

Using Pythagoras' theorem, an upper bound of the right-hand side of (C.2) is found in the form

$$2 \left| \sin\left(\frac{\omega\tilde{\xi}_{cam}}{2}\right) \right| \sqrt{T_O^2 + \frac{1}{\omega^2}}.$$

Hence,

$$\frac{1}{V_O} + T_O > 2 \left| \sin\left(\frac{\omega\tilde{\xi}_{cam}}{2}\right) \right| \sqrt{T_O^2 + \frac{1}{\omega^2}}$$

ensures internal stability of (5.22).

The task is to determine the global maximum of

$$rhs(\omega) = 2 \left| \sin \left( \omega \frac{\tilde{\xi}_{cam}}{2} \right) \right| \sqrt{T_O^2 + \frac{1}{\omega^2}} \quad (\text{C.3})$$

with respect to  $\omega$ . Note that (C.3) is symmetric in  $\omega$ . The maximum of  $rhs(\omega)$  is found by analyzing the roots  $\omega^*$  of  $\frac{drhs(\omega)}{d\omega} \Big|_{\omega=\omega^*}$ . The roots  $\omega^*$  follow from solving the equation

$$0 = \left( \frac{\tilde{\xi}_{cam}\omega^*}{2} \right)^3 \left( \frac{2T_O}{\tilde{\xi}_{cam}} \right)^2 + \frac{\tilde{\xi}_{cam}\omega^*}{2} - \tan \left( \frac{\tilde{\xi}_{cam}\omega^*}{2} \right). \quad (\text{C.4})$$

Utilizing the Taylor series expansion of  $\tan(x)$  about 0, i. e.,  $\tan(x) = x + \frac{1}{3}x^3 + \frac{2}{15}x^5 + \frac{17}{315}x^7 + \dots$ , (C.4) may be written in the specialized form

$$0 = \left( \frac{\tilde{\xi}_{cam}\omega^*}{2} \right)^3 \left[ \underbrace{\left( \frac{2T_O}{\tilde{\xi}_{cam}} \right)^2}_{k_1} - \underbrace{\frac{1}{3} - \frac{2}{15} \left( \frac{\tilde{\xi}_{cam}\omega^*}{2} \right)^2 - \frac{17}{315} \left( \frac{\tilde{\xi}_{cam}\omega^*}{2} \right)^4 - \dots}_{k_2(\omega^*)} \right]. \quad (\text{C.5})$$

Clearly,  $\omega^* = 0$  is a solution of (C.5). Because of  $k_2(\omega^*) \leq 0$ , an additional solution of (C.4) exists for  $k_1 > 0$ , i. e., if  $T_O > \frac{|\tilde{\xi}_{cam}|}{2\sqrt{3}}$ .

The solution  $\omega^* = 0$  only represents a maximum of  $rhs(\omega)$  if  $T_O < \frac{|\tilde{\xi}_{cam}|}{2\sqrt{3}}$  because then

$$\frac{d^2rhs(\omega)}{d\omega^2} \Big|_{\omega=0} = \frac{1}{12} |\tilde{\xi}_{cam}| (12T_O^2 - \tilde{\xi}_{cam}^2)$$

is negative. For  $T_O > \frac{|\tilde{\xi}_{cam}|}{2\sqrt{3}}$ , the global maximum occurs at  $\omega = \pm\omega^*$  where  $\omega^*$  is the smallest strictly positive solution of (C.4).

---

## Bibliography

---

- [1] Y. Tanaka, K. Omori, T. Miyake, K. Nishizaki, M. Inoue, and S. Tezuka, “Camber control techniques in plate rolling”, Kawasaki Steel, Tech. Rep. 16, Jun. 1987.
- [2] R.C. González, R. Valdés, and J.A. Cancelas, “Vision based measurement system to quantify straightness defect in steel sheets”, in *Proceedings of 9<sup>th</sup> International Conference on Computer Analysis of Images and Patterns*, Warsaw, Poland, Sep. 2001, pp. 427–434.
- [3] R.J. Montague, J. Watton, and K.J. Brown, “A machine vision measurement of slab camber in hot strip rolling”, *Journal of Materials Processing Technology*, vol. 168, pp. 172–180, 2005.
- [4] B.N. Carruthers-Watt, Y. Xue, and A.J. Morris, “A vision based system for strip tracking measurement in the finishing train of a hot strip mill”, in *Proceedings of 2010 IEEE ICMA*, Xi’an, China, Aug. 2010, pp. 1115–1120.
- [5] I. Mallocci, J. Daafouz, C. Iung, R. Bonidal, and P. Szczepanski, “Robust steering control of hot strip milling”, *IEEE Transactions on Control Systems Technology*, vol. 18, no. 4, pp. 908–917, 2010.
- [6] J.W. Yoo, N.W. Kong, J. Song, and P.G. Park, “Camber detection algorithm using the image stitching technique in hot-rolling process”, in *Proceedings of International Conference on Robotics*, Phuket, Thailand, Nov. 2010, pp. 74–77.
- [7] J. Lee, N. Kong, J. Yoo, and P. Park, “A fast image stitching algorithm in the endless hot rolling process”, in *Proceedings of 11<sup>th</sup> International Conference on Control, Automation and Systems*, Gyeonggi-do, Korea, Oct. 2011, pp. 1264–1268.

- [8] N.W. Kong, J.W. Yoo, J.S. Lee, S.W. Yun, J. Bae, and P.G. Park, “Vision-based camber measurement system in the endless hot rolling process”, *Optical Engineering*, vol. 50, no. 10, pp. 107202/1–107202/10, 2011.
- [9] A. Ollikkala, T. Kananen, A. Mäkynen, M. Holappa, E. Torppa, and T. Harvala, “A single camera system for camber measurement in hot strip rolling”, in *Proceedings of Rolling 2013 - 9<sup>th</sup> International Rolling Conference and the 6<sup>th</sup> European Rolling Conference*, Venice, Italy, Jun. 2013.
- [10] T. Kiefer and A. Kugi, “An analytical approach for modelling asymmetrical hot rolling of heavy plates”, *Mathematical and Computer Modelling of Dynamical Systems*, vol. 14, no. 3, pp. 249–267, 2008.
- [11] T. Ishikawa, Y. Tozawa, and J. Nishizawa, “Fundamental study on snaking in strip rolling”, *Transactions of the Iron and Steel Institute of Japan*, vol. 28, no. 6, pp. 485–490, 1988.
- [12] T. Shiraishi, H. Ibata, A. Mizuta, S. Nomura, E. Yoneda, and K. Hirata, “Relation between camber and wedge in flat rolling under restrictions of lateral movement”, *Iron and Steel Institute of Japan International*, vol. 31, no. 6, pp. 583–587, 1991.
- [13] A. Nilsson, “FE simulations of camber in hot strip rolling”, *Journal of Materials Processing Technology*, no. 80–81, pp. 325–329, 1998.
- [14] D.L. Biggs, S.J. Hardy, and K.J. Brown, “Finite element modelling of camber development during hot rolling of strip steel”, *Ironmaking and Steelmaking*, vol. 25, no. 1, pp. 81–89, 1998.
- [15] M. Trull, D. McDonald, A. Richardson, and D.C.J. Farrugia, “Advanced finite element modelling of plate rolling operations”, *Journal of Materials Processing Technology*, vol. 177, pp. 513–516, 2006.
- [16] A. Dixon and D. Yuen, “Mathematical analysis of the effects of width-wise asymmetric rolling conditions on head-end wedge, camber and off-centre”, in *Proceedings of Rolling 2013 - 9<sup>th</sup> International Rolling Conference and the 6<sup>th</sup> European Rolling Conference*, Venice, Italy, Jun. 2013.
- [17] J.H. Ruan, L.W. Zhang, S.D. Gu, W.B. He, and S.H. Chen, “3D FE modelling of plate shape during heavy plate rolling”, vol. 41, no. 3, pp. 199–205, 2014.
- [18] T. Kiyota, H. Matsumoto, Y. Adachi, E. Kondo, Y. Tsuji, and S. Aso, “Tail crash control in hot strip mill by LQR”, in *Proceedings of American Control Conference*, Denver, Colorado, Jun. 2003, pp. 3049–3054.
- [19] M. Okada, K. Murayama, Y. Anabuki, and Y. Hayashi, “VSS control of strip steering for hot rolling mills”, in *Proceedings of 16<sup>th</sup> IFAC World Congress*, Prague, Czech Republic, 2005, pp. 1681–1686.



- [20] I. Choi, J. Rossiter, J. Chung, and P. Fleming, “An MPC strategy for hot rolling mills and applications to strip threading control problems”, in *Proceedings of 17<sup>th</sup> IFAC World Congress*, Seoul, Korea, Jul. 2008, pp. 1661–1662.
- [21] C.W.J. Hol, J. de Roo, L. Kampmeijer, T. Dirkson, G. Schipper, M. La Maire, and J. van der Lugt, “Model predictive controller for strip-tracking during tail-out of the finishing mill”, in *Proceedings of IFAC MMM 2013 International Symposium*, San Diego, USA, Aug. 2013, pp. 397–402.
- [22] D. Jeong, Y. Kang, Y.J. Jang, D. Lee, and S. Won, “Development of FEM simulator combined with camber reducing output feedback fuzzy controller for rough rolling process”, *Iron and Steel Institute of Japan International*, vol. 53, no. 3, pp. 511–519, 2013.
- [23] F. Schausberger, A. Steinboeck, and A. Kugi, “Optimization-based estimator for the contour and movement of heavy plates in hot rolling”, *Journal of Process Control*, vol. 29, pp. 23–32, 2015.
- [24] F. Schausberger, K. Speicher, A. Steinboeck, M. Jochum, and A. Kugi, “Two illustrative examples to show the potential of thermography for process monitoring and control in hot rolling”, in *Proceedings of 16<sup>th</sup> IFAC Symposium on Control, Optimization and Automation in Mining, Mineral & Metal Processing (MMM)*, Oulu, Finland, Aug. 2015, pp. 48–53.
- [25] F. Schausberger, A. Steinboeck, A. Kugi, M. Jochum, D. Wild, and T. Kiefer, “Vision-based material tracking in heavy-plate rolling”, in *Proceedings of 17<sup>th</sup> IFAC Symposium on Control, Optimization and Automation in Mining, Mineral & Metal Processing (MMM)*, Vienna, Austria, Aug. 2016.
- [26] F. Schausberger, A. Steinboeck, and A. Kugi, “Mathematical modeling of the contour evolution of heavy plates in hot rolling”, *Applied Mathematical Modelling*, vol. 39, pp. 4534–4547, 2015.
- [27] F. Schausberger, A. Steinboeck, A. Kugi, M. Jochum, D. Wild, and T. Kiefer, “Estimation of the thickness asymmetry using models for the contour evolution and vision-based measurements of plates in hot rolling”, in *Proceedings of METEC and 2<sup>nd</sup> European Steel Technology and Application Days (ES-TAD)*, Düsseldorf, Germany, Jun. 2015, pp. 1–8.
- [28] F. Schausberger, A. Steinboeck, and A. Kugi, “Optimization-based reduction of contour errors of heavy plates in hot rolling”, *Journal of Process Control*, vol. 47, pp. 150–160, 2016.
- [29] —, “Feedback control of the contour shape in heavy-plate hot rolling”, *Submitted to IEEE Transactions on Control Systems Technology*, 2016.
- [30] D. Dochain, “State and parameter estimation in chemical and biochemical processes: a tutorial”, *Journal of Process Control*, vol. 13, no. 8, pp. 801–818, 2003.

- [31] J.B. Rawlings and L. Ji, “Optimization-based state estimation: current status and some new results”, *Journal of Process Control*, vol. 22, pp. 1439–1444, 2012.
- [32] C.T. Kelley, *Iterative methods in optimization*, 2nd ed. Philadelphia: SIAM, Frontiers in Applied Mathematics, 1999.
- [33] S.J. Orfanidis, *Optimum signal processing: an introduction*. Prentice Hall, New York, 1996.
- [34] H.D. Baehr and K. Stephan, *Heat and mass transfer*, 2nd ed. New York: Springer, 2006.
- [35] J. Canny, “A computational approach to edge detection”, *IEEE Transactions on Pattern Analysis and Machine Intelligence*, vol. 8, pp. 679–698, 1986.
- [36] T. König, A. Steinböck, A. Kugi, R. Heeg, and T. Kiefer, “Deflection and bending model of a four-high mill stand for heavy plate rolling”, in *Proceedings of 4<sup>th</sup> International Conference on Modelling and Simulation of Metallurgical Processes in Steelmaking, STEELSIM, METEC InSteelCon 2011*, Düsseldorf, Germany, Jun. 2011.
- [37] M.H. Sadd, *Elasticity, theory, applications and numerics*. Academic Press, Burlington, 2009.
- [38] H. Schimmöller, *Analytische Behandlung von Eigenspannungszuständen auf der Grundlage der Elastizitätstheorie*. Technische Universität Hamburg-Harburg, Aug. 1992.
- [39] G.B. Airy, “On the strains in the interior of beams”, *Philosophical Transactions of the Royal Society of London*, no. 153, pp. 49–80, 1863.
- [40] A. Pucher, “Über die Berechnung der Einflußfelder ebener Platten”, *Berichte der Gesellschaft von Freunden der technischen Hochschule Berlin*, 1940, pp. 60–68.
- [41] J.N. Reddy, *An introduction to the finite element method*, 3rd ed. London: McGraw-Hill, 2006.
- [42] V.I. Krylov, *Approximate calculation of integrals*. MacMillan, London, 1962.
- [43] F. Richter, “Physikalische Eigenschaften von Stählen und ihre Temperaturabhängigkeit”, Mannesmann AG, Tech. Rep. 10, 1983, p. 42.
- [44] J.G. Lenard, *Primer on flat rolling*, 2nd ed. Oxford: Elsevier, 2014.
- [45] K.H. Weber, “Hydrodynamic theory of rolling”, *Journal of the Iron and Steel Institute*, vol. 203, pp. 27–35, 1965.
- [46] A. Kugi, W. Haas, K. Schlacher, K. Aistleitner, H.M. Frank, and W. Rigler, “Active compensation of roll eccentricity in rolling mills”, *IEEE Transactions on Industry Applications*, vol. 36, no. 2, pp. 625–632, 2000.

- [47] J. Nocedal and S.J. Wright, *Numerical optimization*, 2nd ed. New York: Springer Series in Operations Research, 2006.
- [48] N. Abe and K. Yamanaka, “Smith predictor control and internal model control - A tutorial”, in *Proceedings of SICE Annual Conference*, Fukui, Japan, Aug. 2003, pp. 1383–1387.
- [49] J.E. Normey-Rico and E.F Camacho, *Control of dead-time processes*. London: Springer, 2007.
- [50] M. Vidyasagar, *Nonlinear systems analysis*, 2nd ed., ser. Classics in Applied Mathematics 42. Philadelphia: SIAM, 1992.
- [51] R.F. Curtain and H. Zwart, *An introduction to infinite-dimensional linear systems theory*. New York: Springer, 1995, vol. 21 of *Texts in Applied Mathematics*.
- [52] E. Polak, *Computational methods in optimization: a unified approach*. New York: Academic Press, 1971.
- [53] C.T. Kelley and E.W. Sachs, “Quasi-newton methods and unconstrained optimal control problems”, *SIAM Journal on Control and Optimization*, vol. 25, pp. 1503–1516, 1987.
- [54] D.P. Bertsekas, *Nonlinear programming*, 2nd ed. Belmont, Massachusetts: Athena Scientific, 1999.